MAGNETIC ANNIHILATION, NULL COLLAPSE AND CORONAL HEATING

Christopher Mellor

A Thesis Submitted for the Degree of PhD
at the
University of St Andrews

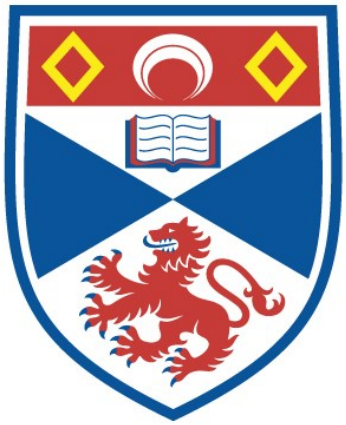

2004

Magnetic Annihilation, Null Collapse and Coronal Heating

Christopher Mellor

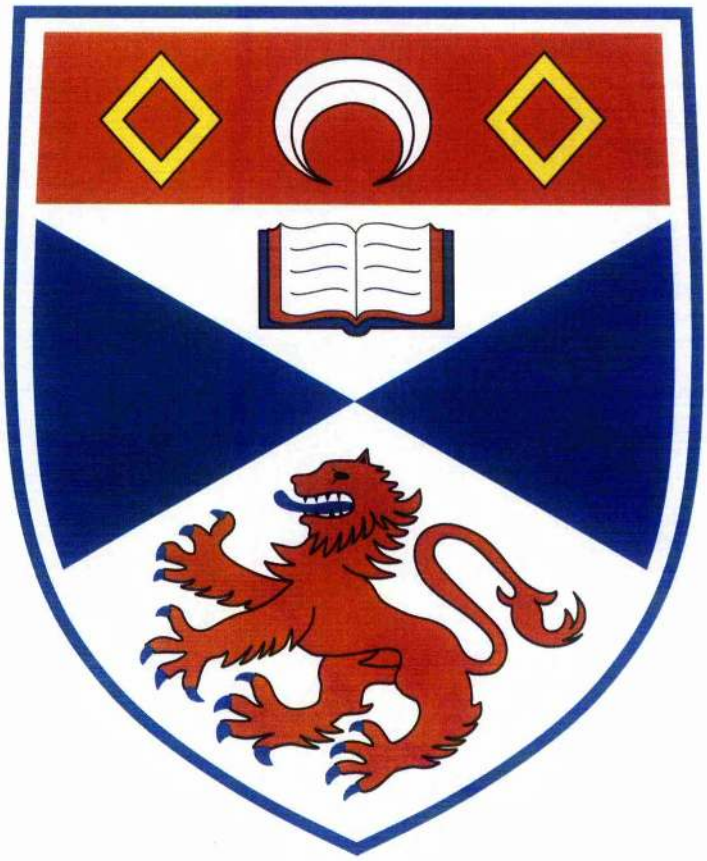

Thesis submitted for the degree of Doctor of Philosophy
of the University of St Andrews

14th January 2004

Abstract

The problem of how the Sun's corona is heated is of central importance to solar physics research. In this thesis we model three main areas. The first, *annihilation*, is a feature of non-ideal MHD and focusses on how magnetic field of opposite polarity meets at a null point and annihilates, after having been advected with plasma toward a stagnation point in the plasma flow. Generally, the null point of the field and the stagnation point of the flow are coincident at the origin, but in chapter 2 a simple extension is considered where an asymmetry in the boundary conditions of the field moves the null point away from the origin. Chapter 3 presents a model of reconnective annihilation in three dimensions. It represents flux being advected through the fan plane of a 3D null, and diffusing through a thin diffusion region before being annihilated at the spine line, and uses the method of matched asymptotic expansions to find the solution for small values of the resistivity.

The second area of the thesis covers *null collapse*. This is when the magnetic field in close proximity to a null point is disturbed, causing the field to fold up on itself and collapse. This is a feature of ideal MHD, and causes a strong current to build up, allowing non-ideal effects to become important. When using linearised equations for the collapse problem, we are in fact looking at a linear instability. If this instability initiates a collapse, this is only a valid model until non-linear effects become important. By talking about collapse in chapters 4 and 5 (as it is talked about in the literature), we mean that the linear instability initiates collapse, which in principle, non-linear effects could later stop. Chapter 4 introduces a two-dimensional model for collapse, using the ideal, compressible, linearised MHD equations. It is a general solution in which all spatially linear nulls and their supporting plasma flows and pressure gradients can be checked for susceptibility to collapse under open boundary conditions. Chapter 5 uses the model introduced in chapter 4 to investigate the collapse of three-dimensional, potential nulls (again, spatially linear) for all possible supporting plasma flows and pressure gradients. Using this model, all nulls under consideration are found to collapse and produce large currents, except for a group of 2D O-type nulls supported by

highly super-Alfvénic plasma flows.

The third area of this thesis involves numerically simulating a model of heating by *coronal tectonics* (Priest *et al*, 2002). A simple magnetic field is created and the boundary is driven, also in a simple manner. Current sheets which scale with grid resolution are seen to build up on the quasi-separatrix layers, and there is some evidence of magnetic reconnection.

Declaration

1. I, Christopher Mellor, hereby certify that this thesis, which is approximately 35,000 words in length, has been written by me, that it is a record of work carried out by me and that it has not been submitted in any previous application for a higher degree.

   date 14.1.04 ..... signature of candidate .....

2. I was admitted as a research student in October 2000 and as a candidate for the degree of PhD in October 2001; the higher study for which this is a record was carried out in the University of St Andrews between 2000 and 2003.

   date 14.1.04 ..... signature of candidate .....

3. I hereby certify that the candidate has fulfilled the conditions of the Resolution and Regulations appropriate to the degree of PhD in the University of St Andrews and that the candidate is qualified to submit the thesis in application for that degree.

   date 14.1.04 ..... signature of supervisor .....

4. In submitting this thesis to the University of St Andrews I understand that I am giving permission for it to be made available for use in accordance with the regulations of the University Library for the time being in force, subject to any copyright vested in the work not being affected thereby. I also understand that the title and abstract will be published and that a copy of the work may be made and supplied to any bona fide library or research worker.

   date 14.1.04 ..... signature of candidate .....

Acknowledgements

Much praise and many thanks must be piled, nay heaped, upon

My parents, without whom I wouldn't be here slaving away over a hot computer

My sister, Fiona

Cath

Eric Priest who took me on and gave me some of the years of his life

Klaus Galsgaard and Slava Titov for working and showing patience with me and giving me the ability to do the work

Dr Boothroyd and Dr Segar at Oriel College, who managed to steer me through all adversity towards my undergraduate degree

All my friends and the rest of my family who have helped me to keep my perspective

All the friendly people in the Solar Group, especially my office mates (David Boddie, Clare Foullon, Laura Carcedo and Robert Kevis)

I would like to acknowledge gratefully the financial support of PPARC. The numerical simulations were carried out using the JREI/SHEFC funded Compaq cluster and the PPARC/SRIF funded maths cluster in St Andrews.

And many thanks to Larson, who provided the amusing cartoons that punctuate this otherwise tedious document.

Contents

List of Figures

Chapter 1

Introduction

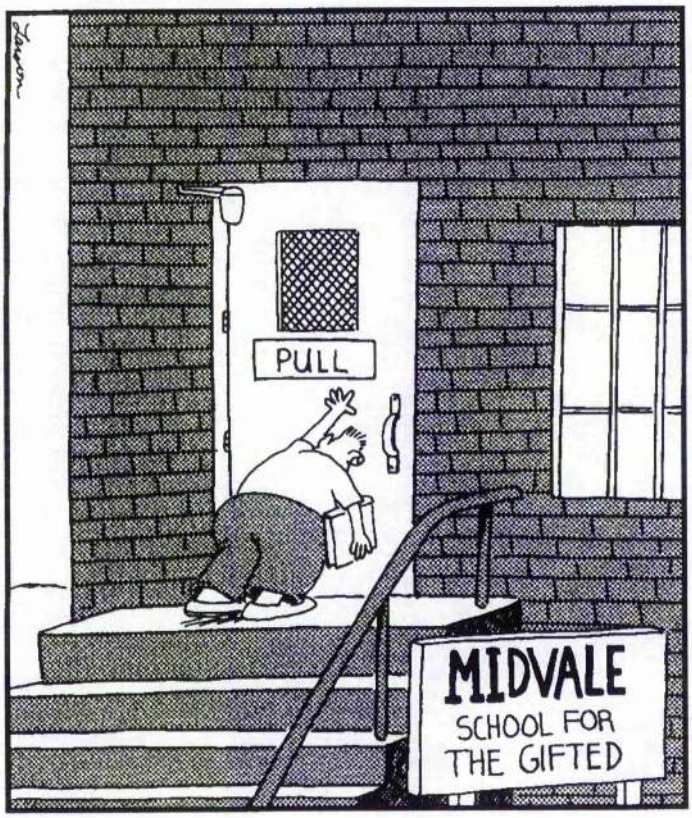

1.1 Overview of the Sun

Containing over 99% of the total mass in the solar system, the Sun is our nearest star and the source of life on Earth. It is no wonder that, as such, it is an obvious focus of scientific interest. The Sun is a huge, searing hot ball of ionised plasma, powered by nuclear fusion. Fig 1.1 shows a simple section through the Sun, showing the core, radiative zone, convective zone and some information about temperatures and densities in the core and at the photospheric surface.

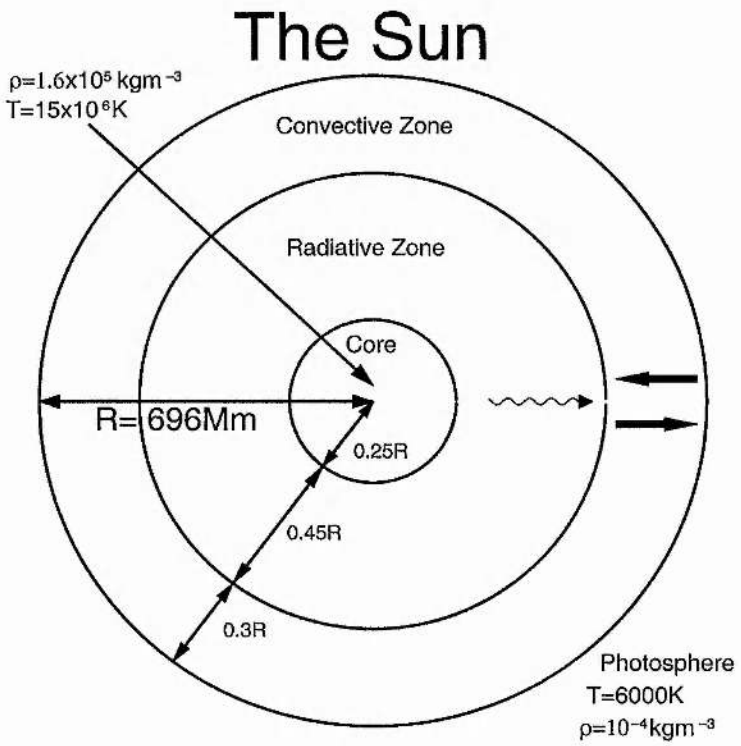

Figure 1.1: A schematic diagram of the Sun, showing the core, the radiative zone and the convective zone.

The atmosphere of the Sun is divided into three tiers. The photosphere, chromosphere and of most interest for the purposes of this thesis, the corona. The corona is the outermost part of the Sun and stretches from 4000km above the surface, right out past the Earth and other planets as the solar wind. It is extremely tenuous ($\rho = 10^{-12}\text{kgm}^{-3}$) and very hot ($T > 10^6\text{K}$). One of the biggest questions in the study of the corona is *why is it so much hotter than the photosphere and chromosphere?* It is widely believed that the magnetic field in the corona is responsible.

All of the major features and dynamic events of the corona (such as flares, prominences, sunspots and many others) are driven by the Sun's magnetic field. The origin of this magnetic field lies in the convection of ionised plasma beneath the surface of the Sun. The moving electric

charges in this solar dynamo give rise to a magnetic field which is transported to the surface of the Sun by magnetic buoyancy in the convective zone. Once the field has emerged into the corona, the forces it exerts are much stronger than those due to the coronal plasma. This means that it is the magnetic field rather than the plasma that acts as the driving force for coronal phenomena.

Among the most important magnetic processes is magnetic reconnection. This happens when a region of strong current allows magnetic field lines to break and join to other field lines. This change of connectivity releases energy which was previously stored in the magnetic field and is thought to be one of the reasons why the corona is so hot. Some of the regions which may be important to the occurrence of reconnection are included in the topological skeleton of the magnetic field. The skeleton of a magnetic field is made up of the null points of the field, the spines and fans (explained later) associated with these nulls, and the separators (field lines joining two nulls) and separatrices (the intersections of fans which mark the boundaries of regions of different magnetic connectivity). Figure 1.2 shows an example of a magnetic skeleton due to three unbalanced photospheric magnetic sources.

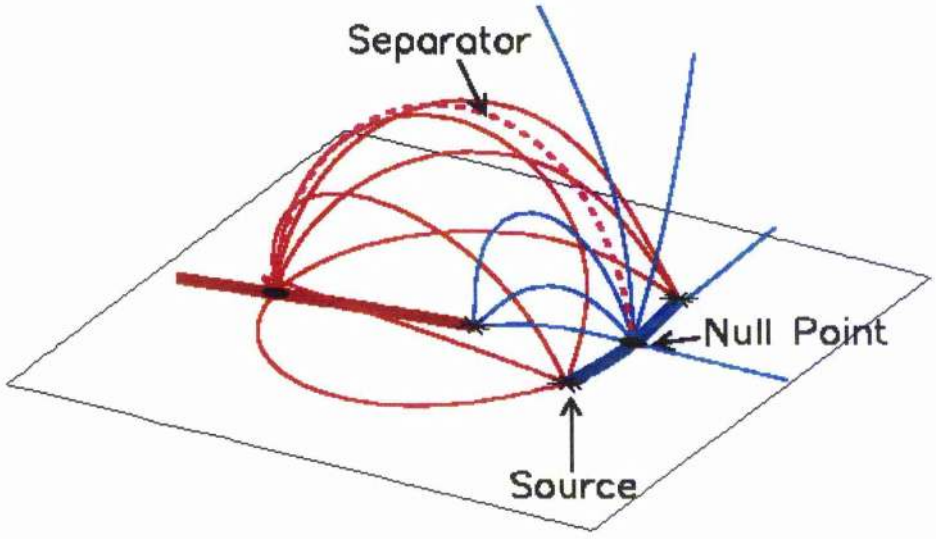

Figure 1.2: Three-dimensional fieldline plot showing the magnetic skeleton due to three unbalanced sources (black stars). The red dome is the separatrix surface forming the fan of the null point (black spot) on the left and the thicker red line is its spine. The blue dome and thicker line are the equivalent structures for the other null point. The dotted purple line is the separator which joins the two null points. This is also the curve where the two separatrix domes intersect.

In this thesis, we are most interested in the null points of the magnetic field. The early chapters are concerned with magnetic annihilation at a null point with a current sheet concentrated along the spine of the null, and the later chapters explore the collapse of the magnetic field close to a null and the formation of current sheets, an important prelude to the onset of reconnection. The final piece of work is a basic, preliminary numerical simulation of a model for coronal tectonics,

where current sheets are seen to build up at quasi-separatrix layers.

1.2 Introduction to the Thesis

The universe consists mainly of ionised gas, or plasma, which often forms highly dynamic and complex systems. When a plasma interacts with a magnetic field, such as in the corona of a star, it may be structured, heated and also accelerated by the field. The two are coupled to each other in a subtle non-linear manner. In this environment the magnetohydrodynamic (MHD) equations are often appropriate for modelling a wide range of processes.

A very important process that occurs in a magnetised plasma is magnetic reconnection at a null point. This causes a change in magnetic topology to take place due to field lines changing their connectivity. The process often releases a great deal of energy that was previously stored in the field. It is thought to be at least partially responsible for the heating of the solar corona and for many other phenomena in laboratory, space, solar and astrophysical plasmas. Reconnection can occur when a strong current causes the field lines to diffuse through the plasma and become connected to different field lines. In three dimensions, reconnection can occur either at null points (e.g., Priest and Titov, 1996; Galsgaard and Nordlund, 1997b) or in the absence of null points (e.g. Schindler *et al*, 1988; Priest and Forbes, 1989; Priest and Demoulin, 1995; Hornig and Rast ätter, 1998). A detailed account of all these aspects can be found in a recent monograph (Priest and Forbes, 2000).

Null points are locations where the magnetic field vanishes. When one of these points collapses, a strong current sheet is formed around the null. The current sheet may be the catalyst for an increase in resistivity in the plasma which can trigger fast reconnection. This introduction concentrates on existing exact solutions for the collapse of null points and the resulting annihilation of magnetic field.

1.2.1 The Validity of MHD

There are several approximations under which MHD is valid. These are discussed further in Priest (1982), Goedbloed (1983) and Biskamp (1993). They can be summarised briefly as follows.

1. The MHD equations are single fluid equations.
2. The length-scale under consideration is much larger than the Debye length, $\lambda_D = \left(\epsilon_0 k_B T / e^2 n_e\right)^{1/2}$,

where ϵ_0 is the permeability of free space, k_B is the Boltzman constant, T is the temperature of the plasma, e is the ion charge and n_e is the ion number density.

3. The length-scale under consideration is also much larger than $r = (2mk_BT)^{1/2}/eB$, the ion-gyro radius, where m is the ion mass and B is the field strength across the electric field.
4. All velocities under consideration are much less than the speed of light, such that the displacement current, $(d\mathbf{E}/dt)/c^2$, in Ampére's law can be neglected.
5. The factor of 2 in the ideal gas law is for a hydrogen plasma. This is a good approximation in the solar corona.

1.2.2 The MHD Equations

The MHD equations for $\mathbf{v}$, $\mathbf{B}$, p, ρ that we shall employ are equations 1.1-1.9, namely, the induction equation

$$\frac{\partial \mathbf{B}}{\partial t} = \nabla \times (\mathbf{v} \times \mathbf{B}) + \eta \nabla^2 \mathbf{B}, \tag{1.1}$$

Ohm's Law

$$\mathbf{j} = \sigma(\mathbf{E} + \mathbf{v} \times \mathbf{B}), \tag{1.2}$$

the equation of motion

$$\rho \frac{D\mathbf{v}}{Dt} = -\nabla p + \mathbf{j} \times \mathbf{B} + \rho \mathbf{g} + \mathbf{F}, \tag{1.3}$$

the equation of mass continuity

$$\frac{\partial \rho}{\partial t} + \nabla \cdot (\rho \mathbf{v}) = 0, \tag{1.4}$$

the ideal gas law

$$P = 2\rho RT, \tag{1.5}$$

and an energy equation such as

$$\frac{\rho^\gamma}{\gamma - 1} \frac{D}{Dt} \left(\frac{p}{\rho^\gamma} \right) = \frac{j^2}{\sigma}, \tag{1.6}$$

with the initial constraint

$$\nabla \cdot \mathbf{B} = 0, \tag{1.7}$$

where $\mathbf{B}$ is the magnetic field, $\mathbf{v}$ is the plasma velocity, ρ is the plasma density, $\mathbf{j}$ is the current density, p is the thermal plasma pressure, $\mathbf{g}$ is the acceleration due to gravity, $\mathbf{F}$ is the force due to other effects, such as viscosity and γ is the ratio of specific heats. The permeability is μ_0 and the diffusivity of the plasma is $\eta = 1/(\mu_0\sigma)$ where σ is the conductivity (all assumed to be constant). The primary variables, $\mathbf{v}$, $\mathbf{B}$ and ρ can be determined from Equations 1.1-1.5. The secondary variables $\mathbf{E}$ (the electric field) and $\mathbf{j}$ then result from Ampère's and Faraday's laws, namely,

$$\mathbf{j} = \frac{1}{\mu_0}\nabla \times \mathbf{B}, \tag{1.8}$$

$$\nabla \times \mathbf{E} = -\frac{\partial \mathbf{B}}{\partial t}. \tag{1.9}$$

1.2.3 The Structure of Two-Dimensional Null Points

Null (or neutral) points occur where the local magnetic field vanishes. In the linear approximation, the magnetic field $\mathbf{B}$ near a null point can be represented as

$$\mathbf{B} = \mathbf{M} \cdot \mathbf{r}, \tag{1.10}$$

where $\mathbf{M}$ is a matrix with elements $M_{ij} = \partial B_i/\partial x_j$ and $\mathbf{r}$ is the position vector.

In two dimensions (x, y), the most general form for $\mathbf{M}$ is

$$\mathbf{M} = \begin{bmatrix} p & \frac{1}{2}(q-j) \\ \frac{1}{2}(q+j) & -p \end{bmatrix},$$

where p and q are associated with the potential part of the field and j/μ_0 is the current in the z-direction. The associated flux function (A) satisfies

$$B_X = \frac{\partial A}{\partial Y}, \quad B_Y = -\frac{\partial A}{\partial X},$$

and has the form

$$A = \tfrac{1}{4}\left((q-j)Y^2 - (q+j)X^2\right) + pXY. \tag{1.11}$$

By rotating the axes we may eliminate the XY term and reduce this to

$$A = \tfrac{1}{4}\left((j_c - j)y^2 - (j_c + j)x^2\right), \tag{1.12}$$

where

$$j_c = (4p^2 + q^2)^{1/2}, \tag{1.13}$$

is a critical current.

Four different cases arise, as follows

i. $j = 0$.
The flux function then becomes

$$A = j_c(y^2 - x^2)/4,$$

which implies that the field lines are rectangular hyperbolae. The separatrices through the null in this case intersect at right angles. It is referred to as a potential null, since there is no current associated with the field.

ii. $|j| < j_c$.
The flux function here gives hyperbolic field lines with separatrices that intersect at an angle of

$$\tan^{-1}\left(\frac{(j_c^2 - j^2)^{1/2}}{j}\right).$$

This is a non-potential X-point. As $j \to 0$, the field lines tend to rectangular hyperbolae as in the first case.

iii. $|j| = j_c$.
The flux function now depends only on x^2 if $j_c = j$ and only y^2 if $j_c = -j$. The configuration has antiparallel field lines with a null line along the y or x-axis, respectively, and represents a one-dimensional current sheet.

iv. $|j| > j_c$.
The flux function produces concentric ellipses as field lines so the configuration is called an O-point. The ratio of the semi-major and semi-minor axes of the ellipses is

$$\left(\left|\frac{j + j_c}{j - j_c}\right|\right)^{1/2}$$

As $j_c/j \to 0$, these become circular.

Figure 1.3 shows examples of the four different types of null point in two dimensions.

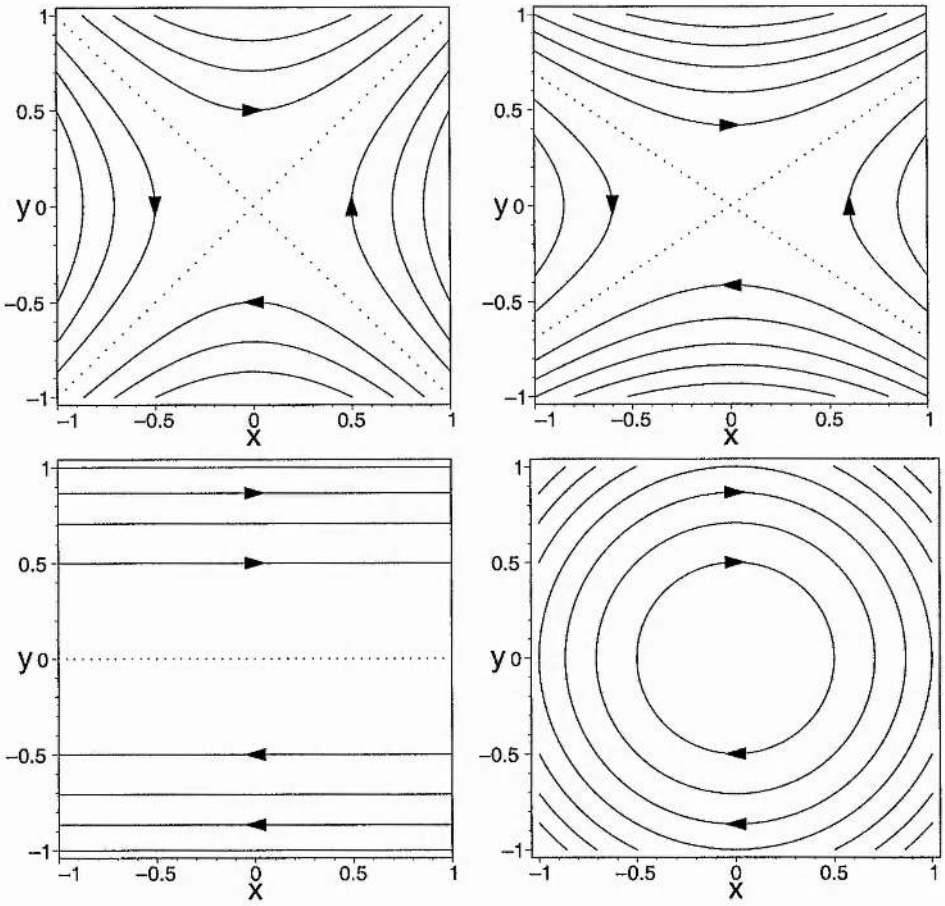

Figure 1.3: Magnetic field lines for the four types of two-dimensional null point. (*Top Left*) A potential X-point ($j = 0$). (*Top Right*) A non-potential X-point ($|j| < j_c$). (*Bottom Left*) A one-dimensional current sheet ($|j| = j_c$). (*Bottom Right*) An O-point ($|j| > j_c$.)

1.2.4 The Structure of Three-Dimensional Null Points

The simplest form that **M** (Equation 1.10) can take in three dimensions is

$$\mathbf{M} = \begin{bmatrix} 1 & \frac{1}{2}(Q - J_{\parallel}) & 0 \\ \frac{1}{2}(Q + J_{\parallel}) & R & 0 \\ 0 & J_{\perp} & -(R+1) \end{bmatrix}, \tag{1.14}$$

where $R \geq -1$, $Q^2 \leq J_{\parallel}^2 + 4R$ and the current is

$$\mathbf{j} = \frac{1}{\mu_0} \begin{pmatrix} J_{\perp} \\ 0 \\ J_{\parallel} \end{pmatrix}$$

The potential part of the field is determined by the parameters R and Q, $J_{\parallel}$ is the current parallel to the z-axis, which is known as the spine, and $J_{\perp}$ is the current perpendicular to the spine. The effects of varying the various parameters and an in-depth treatment of the structure of these nulls has been given by Parnell *et al* (1996). In general, the skeleton of a three-dimensional null consists of a spine curve and a fan plane. The spine is a field line through the null following the eigenvector of the matrix **M** that is associated with the eigenvalue which has a different sign from the other two eigenvalues. The fan is a surface through the null which is defined by the eigenvectors of **M** associated with the remaining eigenvalues (Priest and Titov, 1996). A potential null has spine and fan perpendicular to each other. Increasing $J_{\perp}$ increases the angle between spine and fan whereas varying $J_{\parallel}$ changes the structure of the field lines in the fan. Figure 1.4 shows a simple potential three-dimensional null point, highlighting the location of the spine and the fan.

1.3 Null Point Collapse in Two Dimensions

1.3.1 Equilibrium or Steady-State Structure of a Null

In an ideal steady state, the magnetic field, plasma velocity, plasma pressure and density must satisfy the time-independent MHD equations

$$\nabla \times (\mathbf{v} \times \mathbf{B}) = \mathbf{0}, \tag{1.15}$$

$$\rho(\mathbf{v} \cdot \nabla)\mathbf{v} = -\nabla p + \mathbf{j} \times \mathbf{B}, \tag{1.16}$$

$$\nabla \cdot (\rho \mathbf{v}) = 0, \tag{1.17}$$

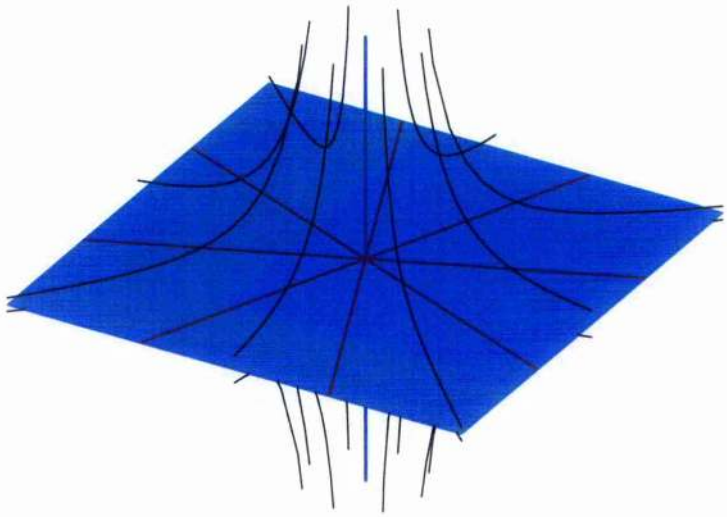

Figure 1.4: A potential three-dimensional null point. The spine is the blue vetical line and the fan plane is the light blue plane. Fieldlines lying in the fan plane are red and a selection of other fieldlines are black.

$$\begin{aligned} &\frac{p}{\rho^\gamma} = \text{constant (in the compressible case)}, \\ &\rho = \text{constant (in the incompressible case)}. \end{aligned} \tag{1.18}$$

In two dimensions, consider first the simplest null point, a potential X-point, where the separatrices are at right angles and there is no current. The equations are satisfied identically when $\mathbf{v} = \mathbf{0}$ and $\nabla p = \mathbf{0}$, so that there is no plasma flow and the pressure is uniform throughout the space which we are considering close to the null.

If we next consider a circular O-point, whose field components are $B_0(-y, x)/l$, the steady-state equations are satisfied with a balance between just the magnetic and centrifugal forces when the plasma flow is directed along the magnetic field and has magnitude $\sqrt{2}v_A(-y, x)/l$, where v_A is the Alfvén speed, $B_0/(\mu_0\rho)^{1/2}$. This represents a super-Alfvénic flow parallel to the field and so is unlikely to occur easily in practice. However, if a slower flow $\mathbf{v} = v_0(-y, x)/l$ is present, then a pressure gradient of

$$\nabla p = \frac{\rho\mu_0 v_0^2 - 2B_0^2}{\mu_0 l^2}(x, y). \tag{1.19}$$

can balance the centrifugal and magnetic forces. For an X-point with current, or an elliptical O-point, neither a plasma flow nor a pressure gradient on its own can support the magnetic field, so there needs to be a mixture of both. If the magnetic field and plasma velocities are $B_0(\alpha y, x)/l$

and $v_0(\alpha y, x)/l$, respectively, then the supporting pressure gradient is

$$\nabla p = \frac{1}{\mu_0 l^2} \begin{pmatrix} (-\alpha\rho\mu_0 v_0^2 + B_0^2(\alpha - 1))x \\ -(\alpha\rho\mu_0 v_0^2 + \alpha B_0^2(\alpha - 1))y \end{pmatrix}.$$

With these spatially linear forms for the magnetic field and velocity, the form that is adopted for the plasma pressure is different for a compressible and an incompressible plasma regime. In the compressible case, the pressure $(p_0 + p_1)$ and density $(\rho_0 + \rho_1)$ are assumed to be functions of time alone and independent of space, such that the compressible part of 1.18 is satisfied. After non-dimensionalising and linearising, the equations of motion and mass continuity then become

$$\rho_0 \frac{\partial \mathbf{v_1}}{\partial t} + \rho_0(\mathbf{v_0} \cdot \nabla)\mathbf{v_1} + \rho_1(\mathbf{v_0} \cdot \nabla)\mathbf{v_0} + \rho_0(\mathbf{v_1} \cdot \nabla)\mathbf{v_0} = (\nabla \times \mathbf{B_1}) \times \mathbf{B_0} + (\nabla \times \mathbf{B_0}) \times \mathbf{B_1}, \quad (1.20)$$

$$\frac{\partial \rho_1}{\partial t} + \rho_0 \nabla \cdot \mathbf{v_1} = 0, \quad (1.21)$$

where a subscript 0 denotes the initial, steady state and a subscript 1 indicates the small perturbation. In order to satisfy (1.20), the densities (ρ_0, ρ_1) and pressures (p_0, p_1) are spatially uniform, so there is no spatial pressure gradient.

In the incompressible case, ρ_0 is constant and ρ_1 vanishes. After non-dimensionalising and linearising, the equations of motion and continuity instead become

$$\frac{\partial \mathbf{v_1}}{\partial t} + (\mathbf{v_0} \cdot \nabla)\mathbf{v_1} + (\mathbf{v_1} \cdot \nabla)\mathbf{v_0} = -\nabla p_1 + (\nabla \times \mathbf{B_0}) \times \mathbf{B_1} + (\nabla \times \mathbf{B_1}) \times \mathbf{B_0}, \quad (1.22)$$

$$\nabla \cdot \mathbf{v_1} = 0. \quad (1.23)$$

The constant density (ρ_0) has been scaled out, but this time 1.22 can be satisfied by assuming the perturbed pressure (p_1) is a quadratic function of x and y since there is no (adiabatic) energy equation restricting its form.

1.3.2 Physical Cause of Collapse

In his paper of 1953, Dungey considered what would happen at a potential X-point null if there were no plasma flow or pressure gradient in the basic state. He discovered that the X-point can collapse if the footpoints of the field are allowed to move and energy can propagate into the region of the null point. This can be demonstrated using the following simple example.

Consider the initial magnetic field with components

$$B_{0x} = \frac{B_0}{l} y, \quad B_{0y} = \frac{B_0}{l} x, \tag{1.24}$$

where B_0 and l scale the magnetic field and distance, respectively. The field has rectangular hyperbolae for field lines, described by

$$y^2 - x^2 = \text{constant}, \tag{1.25}$$

as shown in Figure 1.5. The current ($\mathbf{j_0} = (\nabla \times \mathbf{B_0})/\mu_0$) of this field vanishes, so that the force ($\mathbf{j_0} \times \mathbf{B_0}$) exerted by the field on the plasma is also zero, and the field is in equilibrium with itself.

Now consider a perturbation to the field of

$$B_{1y} = \epsilon \frac{B_0}{l} x, \tag{1.26}$$

so that the perturbed field ($\mathbf{B} = \mathbf{B_0} + \mathbf{B_1}$) is now

$$B_x = \frac{B_0}{l} y, \quad B_y = (1+\epsilon)\frac{B_0}{l} x. \tag{1.27}$$

and the field lines are

$$y^2 - (1+\epsilon)x^2 = \text{constant}, \tag{1.28}$$

with the separatrices now no longer perpendicular to each other, but described by

$$y = \pm(1+\epsilon)^{1/2} x, \tag{1.29}$$

much like the closing of a pair of scissors. The field is no longer current-free and possesses a current,

$$\mathbf{j}_1 = \frac{\epsilon B_0}{\mu_0 l} \hat{\mathbf{z}}, \tag{1.30}$$

which means that the linear force exerted by the field is now

$$\mathbf{j}_1 \times \mathbf{B} = \frac{\epsilon B_0^2}{\mu_0 l^2} \left(-x\hat{\mathbf{x}} + y\hat{\mathbf{y}}\right). \tag{1.31}$$

The directions of this force are such as to carry on closing the X-point until it collapses completely, also shown in Figure 1.5. As the field lines close up in this way and ϵ increases, so the ohmic heating ($j^2/\sigma = \epsilon^2 B_0^2/(\sigma \mu_0^2 l^2)$) also increases.

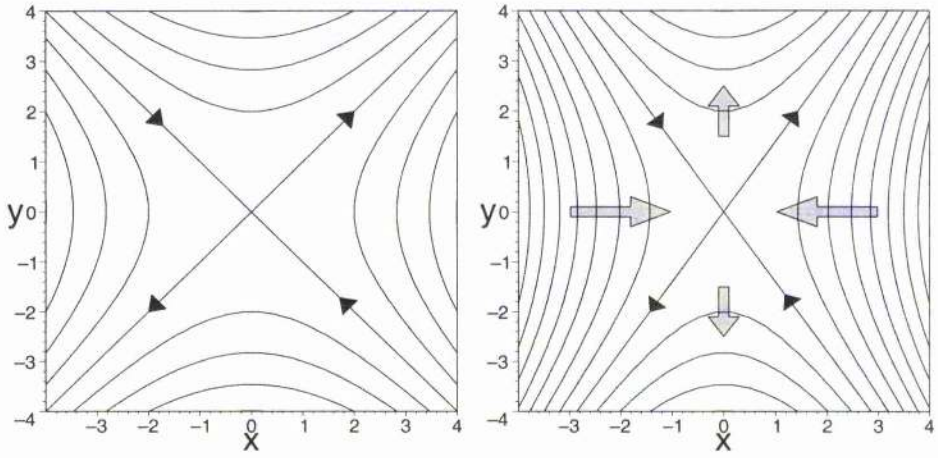

Figure 1.5: The magnetic field lines near an X-type null point, with distance measured in dimensionless units x/l and y/l. The field line spacing depends on the strength of the field. (*Left*) In equilibrium with no current. (*Right*) Away from equilibrium ($\epsilon = 0.96$) with the resultant force on the x- and y-axes indicated by the thick arrows. It can be seen that this force will carry on the collapse of the X-point.

1.3.3 Linear Collapse

Linear analyses of the collapse problem have been carried out using perturbation techniques by many people during the 1990s (e.g., Bulanov *et al*, 1990; Craig and McClymont, 1991; Hassam, 1992; Fontenla, 1993 and Titov and Priest, 1993). These treatments demonstrate that collapse occurs for a wide variety of initial and boundary conditions. It must be stressed that when one talks about linear collapse (as they do in the literature on the subject), what is really being talked about is a linear instability. In principle, when the linear perturbation grows large enough for non-linear terms to become important, these may possibly halt the collapse. The linear results are obtained by linearising the MHD equations and using an initial flux function describing a potential X-point ($A_0 = B_0 l(\bar{x}^2 - \bar{y}^2)$) where $\bar{x} = x/l$ and $\bar{y} = y/l$. Setting the pressure to zero leads to a third-order, linear differential equation for the linear perturbation (A_1), namely,

$$\frac{\partial^2 A_1}{\partial \bar{t}^2} = (\bar{x}^2 + \bar{y}^2)\nabla^2 A_1 + \bar{\eta}\nabla^2 \left(\frac{\partial A_1}{\partial \bar{t}} \right), \tag{1.32}$$

The dimensionless time is $\bar{t} = t v_{A0}/l$ and the dimensionless diffusivity is $\bar{\eta} = \eta/(v_{A0} l)$, where v_{A0} is the Alfvén speed, $B_0/(\rho\mu_0)^{1/2}$. There are several ways to solve this equation, and here we follow Craig and McClymont (1991).

Removing all bars from the dimensionless units and setting $A_1 = \exp(\lambda t) f(r) \exp(im\phi)$ in

polar coordinates, the equation for $f(r)$ becomes,

$$r(rf')' = \left(\frac{\lambda^2}{1+\eta\lambda/r^2} + m^2\right) f, \tag{1.33}$$

where $f' \equiv df/dr$. The perturbation (A_1) is set equal to a constant on the boundary, $r = 1$, which freezes the field lines to the boundary.

Very close to the origin, equation (1.32) reduces to the diffusion equation

$$\frac{\partial A_1}{\partial t} = \eta \nabla^2 A_1, \tag{1.34}$$

giving a solution

$$A_{1m} = J_m[(-\lambda/\eta)^{1/2} r] \exp(im\phi + \lambda t),$$

in terms of the Bessel function (J_m).

Away from the origin, in the advection region, Equation (1.32) reduces to the wave equation,

$$\frac{\partial^2 A_1}{\partial t^2} = r^2 \nabla^2 A_1. \tag{1.35}$$

The speed of the wave, and thus the information travelling in from the boundary, varies as the distance (r) from the origin. The only mode, however, which allows topological reconnection at the origin is the $m = 0$ mode, due to the Bessel function form of the current near the origin.

Figure 1.6 shows the evolution of the field lines in the fundamental mode ($m = 0$ with no nodes in the radial direction). The field lines can be seen to be oscillating to and from the null. At the end of the three cycles shown, the system is very close to its equilibrium null point configuration with magnetic diffusion having been responsible for the dissipation of the energy in the system.

1.3.4 Non-Linear Collapse

Whilst Dungey (1953) considered the linear evolution of an initially potential X-type null point, Imshennik and Syrovatsky (1967) extended this by studying the non-linear evolution of an X-point with a compressible flow. They solved the equations

$$\frac{\partial}{\partial x}\frac{dA}{dt} = 0, \quad \frac{\partial}{\partial y}\frac{dA}{dt} = 0,$$

$$\rho\frac{dv_x}{dt} = -\frac{\partial p}{\partial x} - \frac{1}{\mu_0}\frac{\partial A}{\partial x}\nabla^2 A,$$

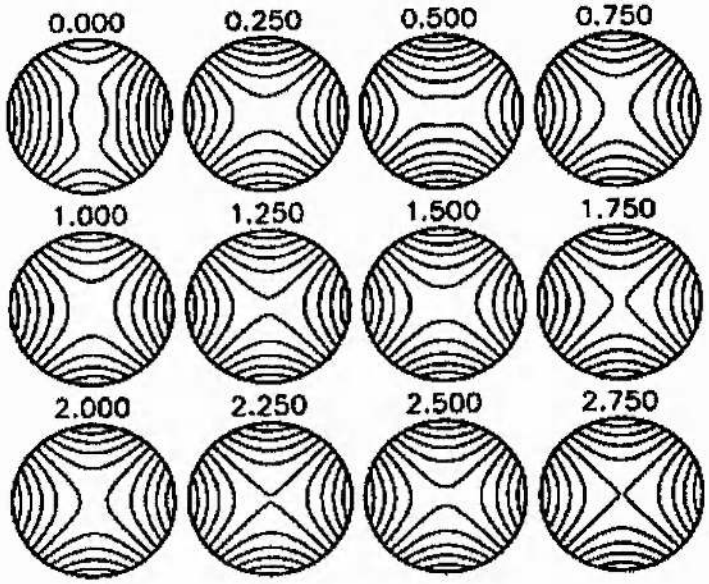

Figure 1.6: Evolution of field lines in the fundamental mode for linear X-point collapse including magnetic diffusion and anchoring the footpoints to the circular boundary. The number above each plot is the number of cycles of oscillation that have passed. After three cycles the system is close to its equilibrium neutral point configuration. (Craig and McClymont, 1991)

$$\rho\frac{dv_y}{dt} = -\frac{\partial p}{\partial y} - \frac{1}{\mu_0}\frac{\partial A}{\partial y}\nabla^2 A,$$

$$\frac{d\rho}{dt} + \rho\nabla.\mathbf{v} = 0. \tag{1.36}$$

A is the magnetic flux function and d/dt is the advective time-derivative. The pressure (p) is assumed to be a function of the density only, with a polytropic equation of state so that $p = p(t)$, $\rho = \rho(t)$ and $\nabla p = \mathbf{0}$. Their initial conditions were

$$\rho(x, y, 0) = \rho_0, \quad A(x, y, 0) = \frac{A_0}{l^2}(x^2 - y^2),$$

$$v_x(x, y, 0) = \frac{Ux}{l}, \quad v_y(x, y, 0) = \frac{Vy}{l}, \tag{1.37}$$

where ρ_0, A_0, U, V are constant. Non-dimensionalising and introducing the new variables

$$\tau = \frac{t}{t_0}, \quad \bar{v}_x = \frac{v_x}{v_0}, \quad \bar{v}_y = \frac{v_y}{v_0},$$

$$\bar{\rho} = \frac{\rho}{\rho_0}, \quad \bar{A} = \frac{A}{A_0}, \quad \bar{y} = \frac{y}{l}, \qquad \bar{x} = \frac{x}{l}, \tag{1.38}$$

where $v_0 = A_0/(l(\mu_0\rho_0)^{1/2})$ and $t_0 = l/v_0$, the Equations (1.36) may be written,

$$\frac{\partial}{\partial\bar{x}}\frac{d\bar{A}}{d\tau} = 0, \quad \frac{\partial}{\partial\bar{y}}\frac{d\bar{A}}{d\tau} = 0,$$

$$\bar{\rho}\frac{d\bar{v}_x}{d\tau} = -\frac{\partial\bar{A}}{\partial\bar{x}}\nabla^2\bar{A}, \quad \bar{\rho}\frac{d\bar{v}_y}{d\tau} = -\frac{\partial\bar{A}}{\partial\bar{y}}\nabla^2\bar{A},$$

$$\frac{d\bar{\rho}}{d\tau} + \bar{\rho}\nabla\cdot\bar{\mathbf{v}} = 0. \tag{1.39}$$

The initial conditions become

$$\bar{\rho}(\bar{x},\bar{y},0) = 1, \quad \bar{A}(\bar{x},\bar{y},0) = \bar{x}^2 - \bar{y}^2, \quad \bar{v}_x(\bar{x},\bar{y},0) = \gamma_0\bar{x}, \quad \bar{v}_y(\bar{x},\bar{y},0) = \delta_0\bar{y},$$

where

$$\gamma_0 = \frac{U}{v_0}, \quad \delta_0 = \frac{V}{v_0}.$$

The system has a solution of the form

$$\bar{A}(\bar{x},\bar{y},\tau) = \alpha(\tau)\bar{x}^2 - \beta(\tau)\bar{y}^2, \quad \bar{\rho}(\bar{x},\bar{y},\tau) = \bar{\rho}(\tau), \quad \bar{v}_x(\bar{x},\bar{y},\tau) = \gamma(\tau)\bar{x},$$
$$\bar{v}_y(\bar{x},\bar{y},\tau) = \delta(\tau)\bar{y},$$

with the unknown functions of τ determined by the following non-linear equations,

$$\dot{\alpha} + 2\alpha\gamma = 0, \quad \dot{\beta} + 2\beta\delta = 0, \quad \bar{\rho}(\dot{\gamma} + \gamma^2) = \alpha(\beta - \alpha), \quad \dot{\bar{\rho}} + \bar{\rho}(\gamma + \delta) = 0,$$
$$\bar{\rho}(\dot{\delta} + \delta^2) = \beta(\alpha - \beta),$$

where $\dot{f} \equiv df/d\tau$ and the initial conditions are $\alpha(0) = 1$, $\beta(0) = 1$, $\gamma(0) = \gamma_0$, $\delta(0) = \delta_0$ and $\bar{\rho}(0) = 1$

Figure 1.7 shows how α and γ vary with τ, for the initial conditions $\gamma_0 = 0$ and different values of δ_0. It can be seen that the solution for these functions blows up after a finite time, which implies that the X-point collapses.

The solutions were shown to become singular at a time τ_0 with an asymptotic behaviour as $\tau \to \tau_0$ given by

$$\alpha \propto \alpha_1, \quad \beta \propto (\tau_0 - \tau)^{-4/3}, \quad \gamma \propto \gamma_1,$$

$$\delta \propto (\tau_0 - \tau)^{-1}, \quad \bar{\rho} \propto (\tau_0 - \tau)^{-2/3}. \tag{1.40}$$

α_1, γ_1 and τ_0 depend on the initial conditions and are found by solving the system of equations numerically.

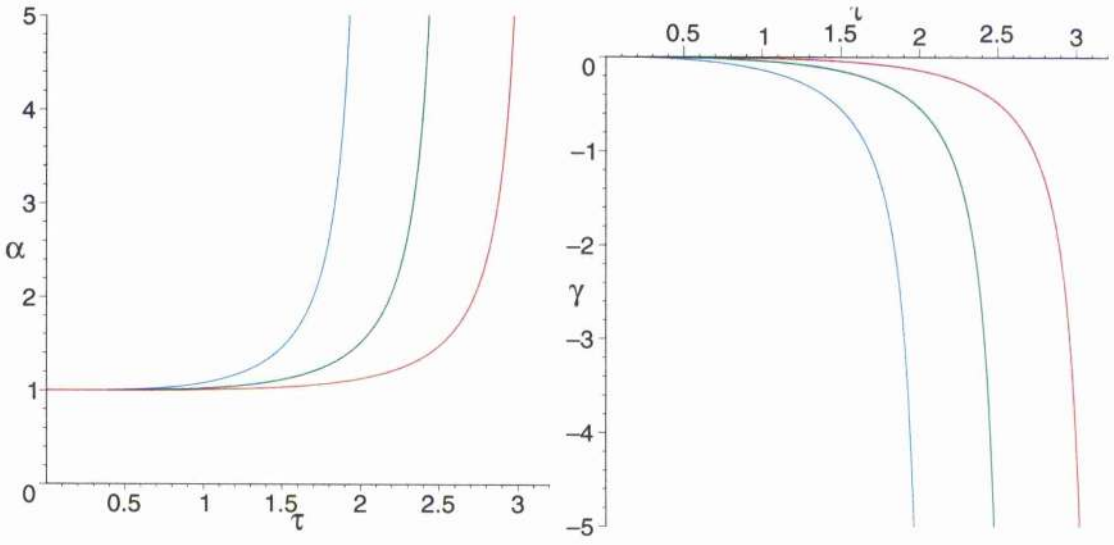

Figure 1.7: (*Left*) The dimensionless flux function (α) as a function of dimensionless time τ and different values of δ_0 ($\delta_0 = 0.01$, the red line; $\delta_0 = 0.03162$, the green line; $\delta_0 = 0.1$, the blue line) for the non-linear collapse of a potential X-point. (*Right*) The dimensionless velocity (γ) as a function of τ. The functions become singular in a finite time, thus collapsing the null.

Other investigations into the collapse of an X-point have been carried out by Chapman and Kendall (1963) and Forbes and Speiser (1979). Later, Neukirch (1995), Neukirch and Priest (2000) and Neukirch and Cheung (2001) found special solutions to the time-dependent MHD equations for an ideal isothermal plasma in which the plasma elements experience no acceleration, or alternatively an acceleration caused by a potential force.

The importance of the open boundary conditions was emphasised by Klapper (1998) who showed that in ideal, two-dimensional, incompressible MHD, a singularity cannot occur in a finite time unless driven by some non-local singularity in the pressure. This is consistent with the original physical argument of Dungey (1953), which needed open boundary conditions to allow energy to propagate into the system from outside.

1.4 Null Point Collapse in Three Dimensions

1.4.1 Introduction

In three dimensions, once again there are steady-state solutions of the MHD equations around a linear null point. As in the two-dimensional case, a potential null supports itself without a plasma flow or pressure gradient. Indeed, the only linear three-dimensional null point which can be in magnetic or force-free equilibrium in the static case is the potential null. This is because the curl

of the $\mathbf{j} \times \mathbf{B}$ force can only be zero when the null point is current-free (or potential).

Other three-dimensional nulls can be supported by a combination of the plasma flow and a pressure gradient. Such flows and pressure gradients were found by Titov and Hornig (2000) for the case of incompressible plasma flow. They used the linear three-dimensional magnetic field given in Equation 1.14 for their field ($\mathcal{B}$) and solved the matrix equations

$$\mathcal{V}^2 - \mathcal{V}^{T2} = \mathcal{B}^2 - \mathcal{B}^{T2}, \tag{1.41}$$

$$tr(\mathcal{V}) = 0, \quad tr(\mathcal{B}) = 0, \tag{1.42}$$

$$\mathcal{V}\mathcal{B} = \mathcal{B}\mathcal{V}, \tag{1.43}$$

$$\mathcal{P} = \mathcal{B}^2 - \mathcal{B}^T\mathcal{B} - \mathcal{V}^2, \tag{1.44}$$

to find the plasma velocity ($\mathcal{V}$) and the pressure gradient matrices. They again discovered that a flow parallel to the field at the Alfvén speed could support the field. However for a null point with spiral field lines in its fan ($|J_\parallel| > \left((R-1)^2 + Q^2\right)^{1/2}$), there are other, non-trivial flows that can sustain the field.

1.4.2 Linear Collapse

As was mentioned in the introduction, by making certain rotations and scalings, the simplest form in which to express the magnetic field close to a null point is $\mathbf{B} = \mathbf{M} \cdot \mathbf{r}$, where $\mathbf{r}$ is the position vector and $\mathbf{M}$ is the 3×3 matrix

$$\mathbf{M} = \begin{bmatrix} 1 & \frac{1}{2}(Q - J_\parallel) & 0 \\ \frac{1}{2}(Q + J_\parallel) & R & 0 \\ 0 & J_\perp & -(R+1) \end{bmatrix}$$

(Parnell *et al*, 1996) where R and Q represent the potential parts of the field, and $J_\parallel$ and $J_\perp$ are the current parallel and perpendicular to the z-axis respectively. When $R > -1$ the eigenvector along the z-axis is always pointing toward the null, and the other two eigenvectors are always pointing away from the null. The z-axis therefore represents the spine and the other two eigenvectors lie in the plane of the fan (Priest and Titov, 1996).

Parnell *et al* (1997) considered three-dimensional potential nulls

$$\mathbf{B_0} = \frac{B_0}{l}[x, Ry, -(R+1)z],$$

with no initial flow and no pressure gradient. When the null was perturbed linearly to introduce

current into the system, they solved the linearised, compressible MHD equations, including

$$\frac{\partial \mathbf{B_1}}{\partial t} = \nabla \times (\mathbf{v_1} \times \mathbf{B_0}),$$

$$\rho_0 \frac{\partial \mathbf{v_1}}{\partial t} = \frac{1}{\mu_0}(\nabla \times \mathbf{B_1}) \times \mathbf{B_0},$$

where $\mathbf{B} = \mathbf{B_0} + \epsilon \mathbf{B_1}$, and $\mathbf{v} = \epsilon \mathbf{v_1}$ with $\epsilon \ll 1$. The resulting density perturbation follows from the continuity equation. They found that the solutions grow exponentially whatever the form of current introduced by the perturbation. These growing solutions indicate that the null point will tend to collapse provided that the footpoints of the field lines are free to move on some boundary.

When a current is introduced perpendicular to the spine, the solutions are of the form

$$\mathbf{B_1} = \frac{\epsilon B_0 J_\perp e^{\omega t}}{l(2R+1)} \begin{pmatrix} 0 \\ -(R+1)z \\ Ry \end{pmatrix},$$

$$\mathbf{v_1} = \frac{\epsilon v_A J_\perp e^{\omega t}}{l(2R+1)} \begin{pmatrix} 0 \\ (R+1)z \\ Ry \end{pmatrix},$$

where $v_A = B_0/(\rho_0 \mu_0)^{1/2}$ and the growth rate $\omega = (2R+1)v_A/l$.

When a current is instead introduced parallel to the spine, the solutions are of the form

$$\mathbf{B_1} = \frac{\epsilon B_0 J_\parallel e^{\omega t}}{l(R-1)} \begin{pmatrix} -Ry \\ -x \\ 0 \end{pmatrix},$$

$$\mathbf{v_1} = \frac{\epsilon v_A J_\parallel e^{\omega t}}{l|R-1|} \begin{pmatrix} -Ry \\ x \\ 0 \end{pmatrix},$$

where $v_A = B_0/(\rho_0 \mu_0)^{1/2}$ and the growth rate $\omega = |R-1|v_A/l$.

Figure 1.8 shows a particular case of the collapse of the null in which the current parallel to the spine grows in time and the fan plane collapses to a one-dimensional line. Figure 1.9 shows the other particular case in which the current perpendicular to the spine grows in time, so that the spine and fan close up towards each other.

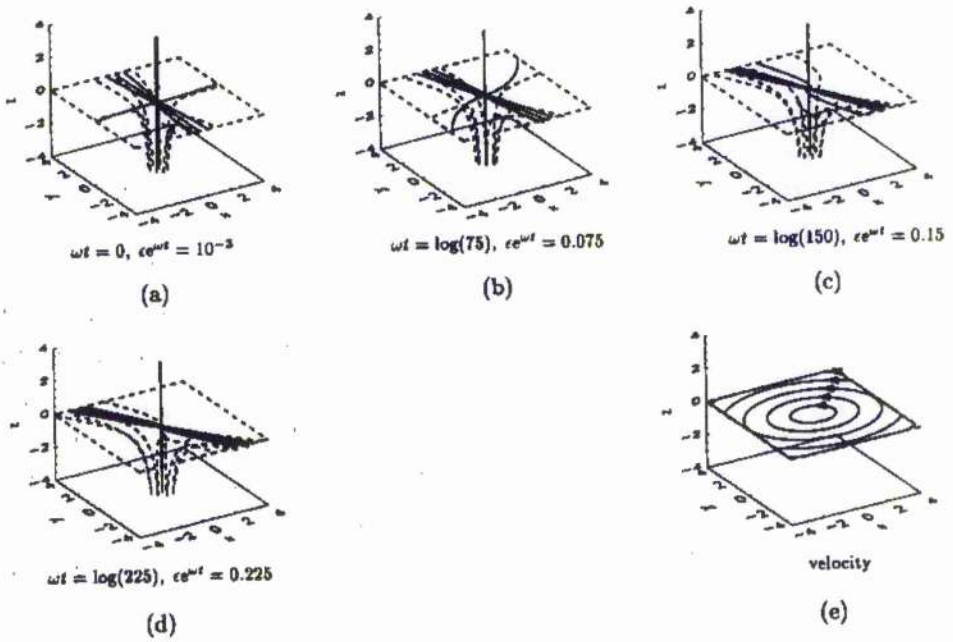

Figure 1.8: The linear collapse of a potential null due to the growth of a spine current along the z-axis. The field lines within the fan plane collapse over time (Parnell *et al*, 1997).

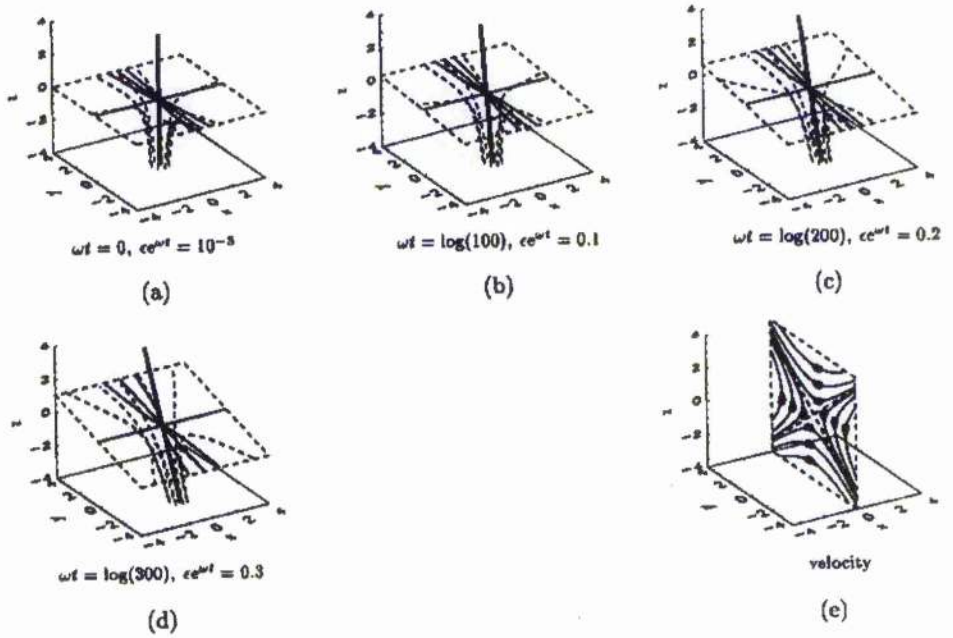

Figure 1.9: The linear collapse of a potential null due to the growth of a fan current along the x-axis. The angle between the spine and fan decreases over time. (Parnell *et al*, 1997).

1.4.3 Non-Linear Collapse

The non-linear collapse of a three-dimensional null with incompressible plasma flow was studied by Bulanov and Olshanetsky (1984). They looked at the non-linear evolution of the incompressible MHD equations. They expressed the plasma flow, magnetic field and pressure in the form $\mathbf{v} = \mathcal{W}(t)\mathbf{r}$ and derived an equation for the deformation matrix ($\mathcal{M}(t)$), where $\mathcal{W} = \dot{\mathcal{M}}\mathcal{M}^{-1}$ with an overdot denoting the time derivative.

$$\ddot{\mathcal{M}} = -\frac{(\mathcal{M}^T)^{-1}\mathcal{P}(0)}{D^{2/3}} + \frac{\mathcal{M}\mathcal{B}^2(0) - (\mathcal{M}\mathcal{B}(0)\mathcal{M}^{-1})^T\mathcal{M}\mathcal{B}(0)}{D}, \tag{1.45}$$

where D denotes $\det\mathcal{M}$. They investigated the special case where

$$\mathcal{B} = \begin{pmatrix} B_{11} & B_{12} & 0 \\ B_{21} & B_{22} & 0 \\ 0 & 0 & B_{33} \end{pmatrix}, \tag{1.46}$$

$$\mathcal{M} = \begin{pmatrix} M_{11} & M_{12} & 0 \\ M_{21} & M_{22} & 0 \\ 0 & 0 & M_{33} \end{pmatrix}, \tag{1.47}$$

and found that a finite time singularity (at $t = t_0$) was formed in the solution. As $t \to t_0$, the asymptotic behaviour of the variables is

$$\mathcal{B} \propto (t - t_0)^{-4/3}, \quad \mathcal{W} \propto (t - t_0)^{-1}, \quad D \propto (t - t_0)^{-2/3}. \tag{1.48}$$

Bulanov and Sakai (1997, 1998) gave a more complete account of the incompressible collapse of null points. In their paper of 1997, using the same system of equations as Bulanov and Olshanetsky (1984) they derived the non-linear equations

$$\dot{v}_{11} + v_{11}^2 + v_{12}v_{21} = (B_{12} - B_{21})B_{21}, \tag{1.49}$$

$$\dot{v}_{12} = (B_{12} - B_{21})B_{22}, \tag{1.50}$$

$$\dot{v}_{21} = -(B_{12} - B_{21})B_{11}, \tag{1.51}$$

$$\dot{v}_{33} + v_{33}^2 = 0, \tag{1.52}$$

$$\dot{B}_{11} + B_{12}v_{21} - v_{12}B_{21} = 0, \tag{1.53}$$

$$\dot{B}_{12} + B_{11}v_{12} - 2B_{12}v_{11} - v_{12}B_{22} = 0, \tag{1.54}$$

$$\dot{B}_{21} + B_{22}v_{21} + 2B_{21}v_{11} - v_{21}B_{11} = 0, \tag{1.55}$$

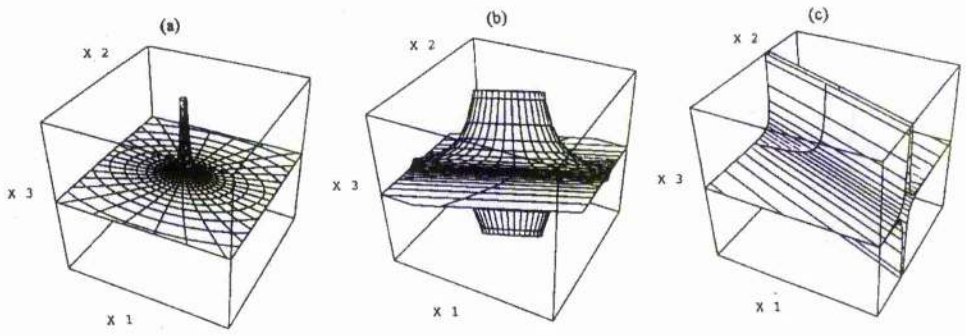

Figure 1.10: The non-linear collapse of a potential null point due to growth of the spine current, causing the spine to flatten out. (Bulanov and Sakai, 1997)

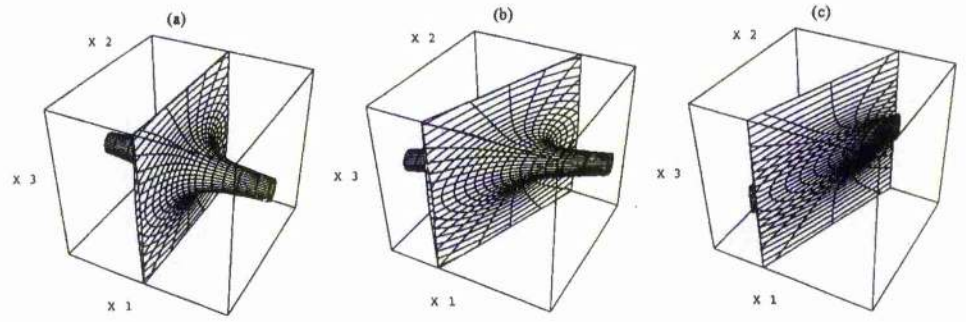

Figure 1.11: The non-linear collapse of a potential null point due to the growth of the fan current, causing the spine to collapse into the fan plane. (Bulanov and Sakai, 1997)

$$\dot{v}_{22} + V_{21}v_{12} - v_{21}B_{12} = 0. \tag{1.56}$$

They started with a potential null point and considered two different cases. In the first case, the perturbation of the flow was parallel to the fan plane of the null, causing spine current density to grow (see Figure 1.10). The spine flattened out and rotated, eventually forming a line of two-dimensional X-points. In the second case, the flow perturbation was parallel to the spine of the null, causing the fan current to grow. The spine collapsed into the fan plane, like a falling tree. The fan plane also changed its position slightly, ending up inclined at a slight angle to its original position as can be seen in Figure 1.11. In their paper of 1998, they extended their analysis to a weakly ionised plasma.

Klapper *et al* (1996) studied the incompressible collapse using the same matrix representation of the magnetic field, plasma flow and pressure, but deduced ordinary differential equations for the traces of these matrices. They showed that the eigenvalues of the magnetic field matrix are constant in time and also that a finite time singularity occurs with collapse of the null.

1.5 Magnetic Annihilation in Two Dimensions

1.5.1 Introduction

Annihilation of a magnetic field is a natural way of converting stored magnetic energy into heat through ohmic dissipation. One of the useful features of annihilation models is that they allow us to study clearly the physical process of energy conversion, one of the ingredients of the more complex phenomenon of magnetic reconnection (e.g., Priest and Forbes, 2000).

1.5.2 Simple Annihilation

Let us assume first that the magnetic Reynolds number for a plasma flow is much smaller than unity, which happens in a current sheet with very small width and non-vanishing diffusivity. We can then reduce the induction equation to the following form

$$\frac{\partial \mathbf{B}}{\partial t} = \eta \nabla^2 \mathbf{B}. \tag{1.57}$$

Consider a one-dimensional field which initially has a uniform, positive value (B_0) for $x > 0$ and a uniform negative value ($-B_0$) for $x < 0$. As time passes, the field will dissipate, starting from the origin (Figure 1.12). The appropriate solution to the induction equation under these conditions is

$$B(x,t) = \frac{2B_0}{\pi^{1/2}} \int_0^{x/(4\eta t)^{1/2}} \exp(-u^2) du. \tag{1.58}$$

The total magnetic flux remains zero due to the symmetry of the solution, since there are equal and opposite amounts on both sides of the central null so that they sum to zero. The total current,

$$J = \int_{-\infty}^{\infty} j \, dx = \frac{2B_0}{\mu_0}, \tag{1.59}$$

is constant and the current just spreads out in space as the current sheet broadens in time. The magnetic energy, however, decreases at a rate

$$\frac{\partial}{\partial t} \int_{-\infty}^{\infty} \frac{B^2}{2\mu_0} dx = - \int_{-\infty}^{\infty} \frac{j^2}{\sigma} dx, \tag{1.60}$$

and so there is pure conversion of magnetic energy into heat energy by ohmic dissipation.

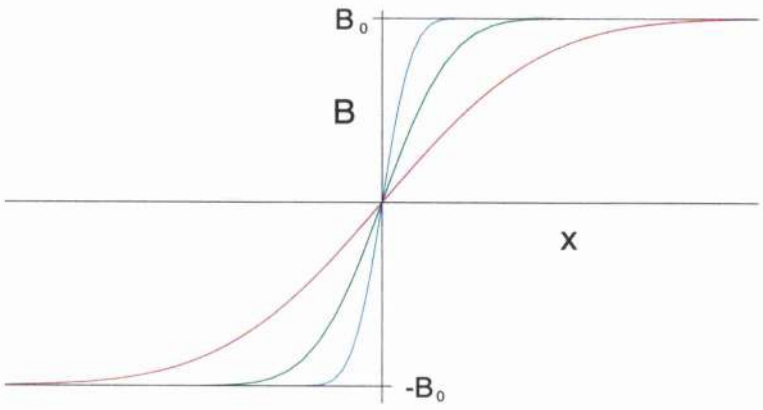

Figure 1.12: The ohmic decay of a simple current sheet with a one-dimensional magnetic field $B(x,t)\hat{\mathbf{y}}$. The initial field profile is the black line, the blue line represents the profile at $t = 1/4$, the green line at $t = 7/4$ and the red line at $t = 49/4$.

1.5.3 Stagnation-Point Flow Model

Sonnerup and Priest (1975), building on earlier work by Parker (1973), discovered an exact solution to the steady-state, incompressible MHD equations for a plasma flow of the form

$$v_x = -\frac{v_0 x}{a}, \quad v_y = \frac{v_0 y}{a},$$

acting on a one-dimensional magnetic field in the y- direction of the form

$$\mathbf{B} = B(x)\hat{\mathbf{y}}.$$

Integrating the induction equation gives us

$$\mathbf{E} + \mathbf{v} \times \mathbf{B} = \eta \nabla \times \mathbf{B}, \tag{1.61}$$

where $\mathbf{E} = E\hat{\mathbf{z}}$ is a constant in two dimensions (x, y) due to Faraday's law. Substituting the field and velocity into Equation (1.61) yields an ordinary differential equation for the unknown $B(x)$, namely,

$$E - \frac{v_0 x}{a} B = \eta \frac{dB}{dx}. \tag{1.62}$$

It may be integrated to give

$$B = \frac{2Ea}{v_0 l} \mathrm{daw}\left(\frac{x}{l}\right), \tag{1.63}$$

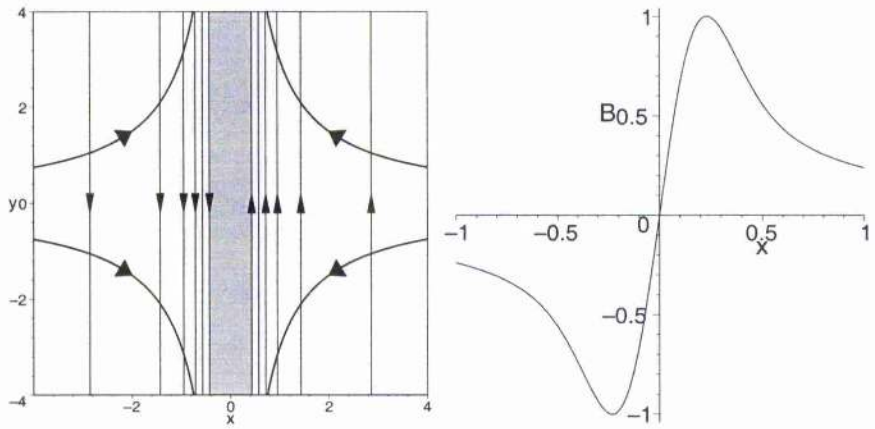

Figure 1.13: The stagnation-point flow model for magnetic annihilation. (*Left*) The velocity stream lines (thick) and the magnetic field lines (thin). The shaded region denotes the diffusion region. (*Right*) A plot of the field strength (B) as a function of distance x.

where $l^2 = 2a\eta/v_0$ and

$$\mathrm{daw}(\xi) = \exp(-\xi^2) \int_0^{\xi} \exp(u^2) du.$$

This represents a hyperbolic plasma flow into the null point along the x-axis and out from the null point along the y-axis. The flow advects the magnetic field lines in towards the stagnation point where they concentrate, causing a current concentration to be formed, before diffusing across the y-axis to annihilate with the field lines from the other side. Figure 1.13 shows the field lines and stream lines of the solution, and also how the field strength varies with distance from the null.

There is, however a limit on how fast the magnetic field can be annihilated. The equation of motion implies

$$\nabla \left(p + \frac{B^2}{2\mu_0} + \frac{\rho v^2}{2} \right) = 0, \tag{1.64}$$

and so determines the plasma pressure as

$$p = p_s - \frac{\rho v^2}{2} - \frac{B^2}{2\mu_0}, \tag{1.65}$$

where p_s is the pressure at the stagnation point. The pressure must always be greater than zero, and so this puts a constraint on the maximum rate of annihilation of the field (Priest, 1996; Litvinenko *et al*, 1996) or the plasma beta (the ratio of the plasma pressure to the magnetic pressure, Jardine *et al*, 1993). The requirement that the pressure be positive can be written as

$$M_e < \frac{1.7(1+\beta_e)}{R_{me}}, \tag{1.66}$$

where M_e is the external Alfvén Mach number, β_e is the external plasma beta and R_{me} is the magnetic Reynolds number. The external values are calculated far from the null at a position $(L_e, 0)$.

1.5.4 Time-Dependent Stagnation-Point Flow

If the stagnation-point flow is generalised to become

$$\mathbf{v} = \frac{v(t)}{a}(x, -y), \tag{1.67}$$

and the magnetic field becomes

$$\mathbf{B} = [B_x(y,t), 0], \tag{1.68}$$

then the induction equation reduces to

$$\frac{\partial B}{\partial t} = \frac{vB}{a} + \frac{vy}{a}\frac{\partial B}{\partial y} + \eta\frac{\partial^2 B}{\partial y^2}. \tag{1.69}$$

Scaling away η and a, and making the substitutions

$$Y = yg(t), \quad \frac{dg}{dt} = vg, \quad \frac{d\tau}{dt} = g^2,$$

Equation (1.69) becomes

$$\frac{\partial B}{\partial \tau} = f(\tau)B + \frac{\partial^2 B}{\partial Y^2}, \tag{1.70}$$

where $f = v/g^2$. This can be solved to give the time-development of an initial magnetic field, $B(Y,0) = B_0(Y)$ in the form

$$B(Y,\tau) = \frac{g}{2(\pi\tau)^{1/2}}\int_{-\infty}^{\infty} B_0(\xi)e^{-(\xi-Y)^2/(4\tau)}d\xi. \tag{1.71}$$

Many different initial configurations and velocity profiles were investigated by Anderson and Priest (1993) in order to discover the time-dependent effects of advection and diffusion on a magnetic field (e.g., Figure 1.14), how the diffusion layer is formed, how it behaves and how it interacts with the magnetic field (see also Clark, 1964; Heyn and Pudovkin, 1993).

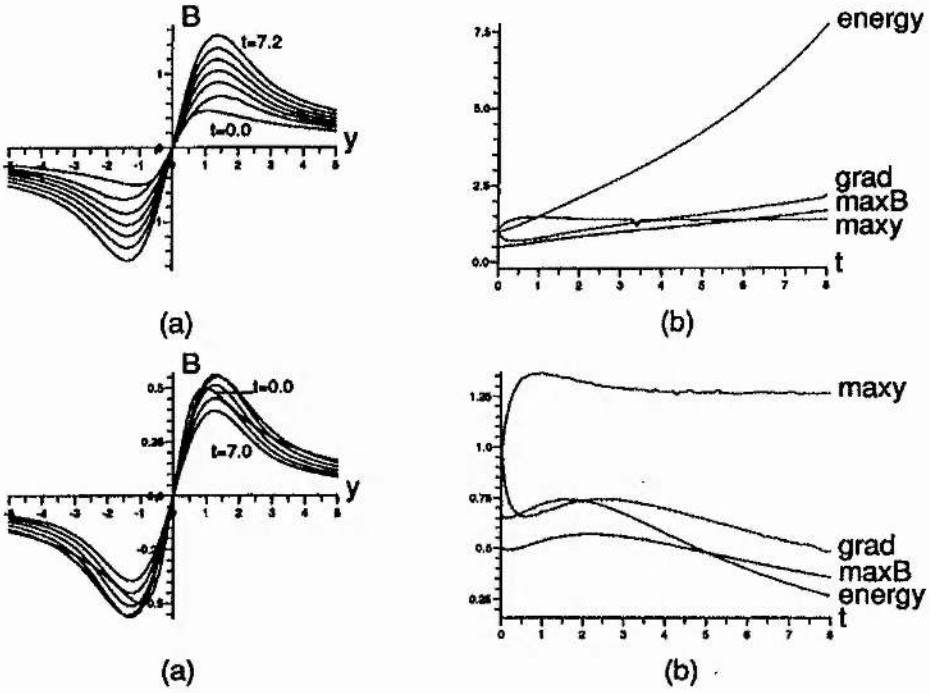

Figure 1.14: Time-dependent magnetic annihilation. (*Top*) The initial profile $B(y) = y/(1+y^{1.9})$. (a) The development of the field for times $t = 0, 1.2, 2.4...7.2$, and (b) the resulting magnetic properties. (*Bottom*) The initial profile $B(y) = y/(1+y^{2.1})$. (a) The development of the field for times $t = 0, 1.4, 2.8...7$, and (b) the resulting magnetic properties. (Anderson and Priest, 1993)

1.5.5 Reconnective Annihilation

The steady stagnation-point flow solution was generalised by Craig and Henton (1995), who considered a two-dimensional velocity

$$v_x = -x, \quad v_y = y - F(x),$$

which satisfies $\nabla \cdot \mathbf{v} = 0$ and a magnetic field of the form

$$\mathbf{B} = \lambda \mathbf{v} + G(x)\hat{\mathbf{y}}$$

which satisfies $\nabla \cdot \mathbf{B} = 0$. The stagnation-point flow is therefore modified by the addition of a simple shear in the y-direction. The corresponding magnetic flux function (A) and stream function (ψ) are given by

$$A = \lambda xy + g(x), \quad \psi = xy + \lambda g(x),$$

where $F(x) = -\lambda\, dg/dx$ and $G(x) = (1 - \lambda^2)\, dg/dx$. $F(x)$ and $G(x)$ are related by

$$F(x) = -\frac{\lambda}{1-\lambda^2} G(x).$$

For this form of solution Equation (1.62) reduces to

$$E - xG = \frac{\eta}{1-\lambda^2}\frac{dG}{dx}, \tag{1.72}$$

which determines $G(x)$ as

$$G(x) = E\left(\frac{2(1-\lambda^2)}{\eta}\right)^{1/2} \mathrm{daw}\left(\left(\frac{1-\lambda^2}{2\eta}\right)^{1/2} x\right). \tag{1.73}$$

λ is a measure of how far this solution is from the stagnation-point flow solution (which is given by $\lambda = 0$). This solution allows one to impose the values of three of the four vector components of $\mathbf{v}$ and $\mathbf{B}$ at some external point. The fourth is determined by the solution in terms of the other three.

This model does not represent genuine reconnection since the current sheet is purely one-dimensional and the magnetic field just diffuses or annihilates across the y-axis (Figure 1.15). It is therefore referred to as reconnective annihilation. The field lines are advected in towards the null and, as in simple annihilation, they diffuse together.

Priest *et al* (2000) generalised this exact solution even further, by adopting flux and stream

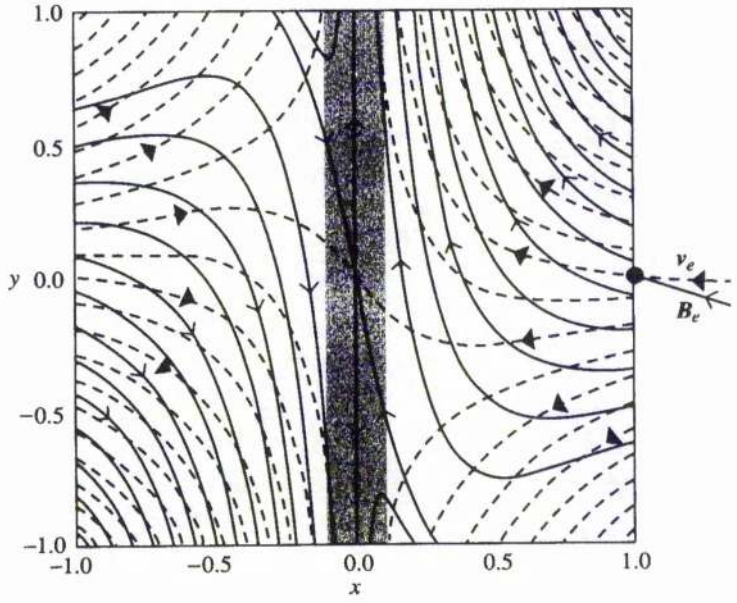

Figure 1.15: The streamlines (dashed) and the field lines (solid) for two-dimensional reconnective annihilation. The diffusion region is shaded grey and the arrows indicate the direction of the field and flow, both inflowing on the boundary. (Priest *et al*, 2000)

functions in the form

$$A = A_0(x) + A_1(x)y, \quad \psi = \psi_0(x) + \psi_1(x)y,$$

to model the magnetic field and plasma flow. Such an approach yields an extra parameter, γ, which allows three different types of solution in the outer advection region. $\gamma < 1$ produces trigonometric solutions, $\gamma = 1$ has solutions like the previous Craig-Henton (1995) solution and $\gamma > 1$ yields hyperbolic solutions.

This form of solution represents physically the same kind of annihilation as the Craig-Henton (1995) solution, but it is a two-fold generalisation in that it allows us to impose all four of the boundary values (v_x, v_y, B_x, B_y) at an external point, as well as the value of γ, whereas the Craig-Henton (1995) solution would only allow three of the four boundary values to be imposed.

1.6 Reconnective Magnetic Annihilation in Three Dimensions

1.6.1 Introduction

Priest and Titov (1996) studied spine reconnection and fan reconnection with the current concentrated along the spine and fan. However, they only presented a kinematic solution. So far

no exact solutions for spine or fan reconnection exist. However, Craig and co-workers have succeeded in discovering exact solutions for three-dimensional reconnective annihilation which are similar in spirit to the reconnective annihilation solutions in two dimensions and which possess one-dimensional current concentrations stretching along either the spine or the fan. The limitation of their model, as of the stagnation-point flow model, is that the current concentrations are not bounded but extend to infinity.

1.6.2 Fan Annihilation

Craig *et al* (1995) extended the idea of reconnective annihilation into three dimensions. They modelled a sheared stagnation-point flow of the form

$$v_x = -x, \quad v_y = Ky - F_y(x), \quad v_z = (1-K)z - F_z(x),$$

with a magnetic field

$$\mathbf{B} = \lambda \mathbf{v} + G_y(x)\hat{\mathbf{y}} + G_z(x)\hat{\mathbf{z}}.$$

This allowed them to consider annihilation in the fan plane of a null point. There was again the relationship

$$F = -\frac{\lambda}{1-\lambda^2}G,$$

and they could solve the differential equations

$$xG_y' + KG_y = -\frac{\eta}{1-\lambda^2}G_y'', \tag{1.74}$$

$$xG_z' + (1-K)G_z = -\frac{\eta}{1-\lambda^2}G_z'', \tag{1.75}$$

to determine the structure of the magnetic field and plasma flow. The fan is given by the plane $x = 0$ and the spine is inclined such that

$$y = -\frac{E_1 x}{\lambda\eta(1+K)}, \quad z = -\frac{E_2 x}{\lambda\eta(2-K)}, \tag{1.76}$$

where E_1 and E_2 are integration constants. Figure 1.16 shows how curved field lines are advected by the flow across the spine into the current sheet ($x = 0$) across which there is no flow.

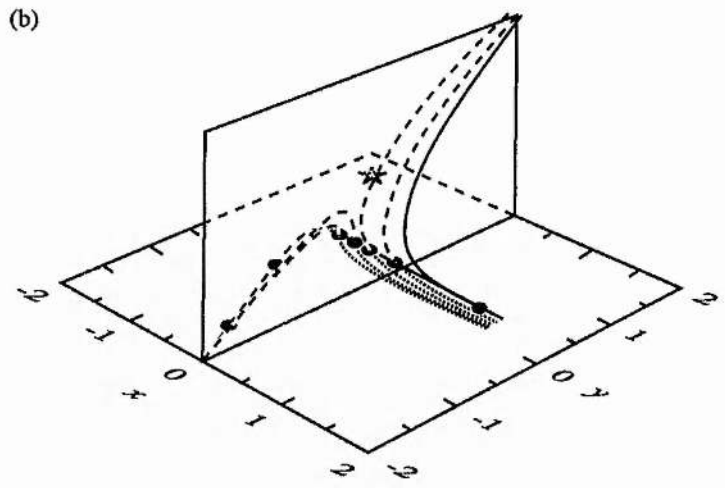

Figure 1.16: The advection of field lines across the spine of a null point in a model of fan reconnective annihilation. The same plasma element is followed and one can see that a field line frozen into the plasma crosses the spine and diffuses in the fan. (Craig *et al*, 1995)

1.6.3 Spine Annihilation

Craig and Fabling (1996) later modelled annihilation occurring along the spine line of a null point. They used cylindrical polar coordinates and considered a plasma velocity and magnetic field of the form

$$v_R = \frac{\alpha R}{2}, \quad v_z = \lambda f(R) \sin\phi - \alpha z, \tag{1.77}$$

$$B_R = \frac{\lambda \alpha R}{2}, \quad B_z = f(R) \sin\phi - \lambda \alpha z, \tag{1.78}$$

where $f(R)$ satisfies

$$\alpha(1-\lambda^2)\left(f + \frac{Rf'}{2}\right) = \eta\left(f'' + \frac{f'}{R} - \frac{f}{R^2}\right) \tag{1.79}$$

and $f' \equiv df/dR$. This yielded a cylindrical diffusion region around the spine of radius $\sim R^{1/2}$. The field close to the spine grows linearly with R and drops off far from the spine and diffusion region as R^{-2}.

1.7 Summary

Studying the collapse of null points is worthwhile, since it is an important means of producing a current sheet. Extensive studies have taken place, each demonstrating that linear X-type nulls are

subject to collapse. The linear and non-linear collapse properties have been determined, and in the absence of dissipative terms the collapse results in a current sheet being formed at the null. Adding the effect of diffusivity or other non-ideal effects allows the collapsing current to dissipate, releasing energy as the magnetic field annihilates or reconnects.

This chapter has been concerned with the exact MHD solutions for collapse, annihilation and reconnective annihilation models in two and three dimensions. The theory of reconnection has been discussed extensively elsewhere (e.g., Priest and Forbes, 2000). Reconnective annihilation has more features in common with the simple annihilation models, and can be thought of as a generalisation of them. The annihilation rate in these models may occur at any rate up to a beta-limited value, depending on the inflow velocity of the plasma and field to the diffusion region. In the annihilation models, the plasma acceleration due to a pressure gradient along the current sheet is passive, due to the stagnation point flow. In genuine reconnection on the other hand, this acceleration is due to a combination of the Lorentz force and an excess plasma pressure in a sheet of finite length.

The MHD equations are highly non-linear and so exact solutions are extremely rare. Until ten years ago only the Imshenik and Syrovatsky (1967) collapse solution and the steady stagnation-point flow annihilation solution were known, but a combination of ingenuity and good fortune has now produced a series of generalisations of these. Such exact solutions are invaluable in highlighting the basic physical processes in a transparent manner and may form the basis for more complex approximate and computational studies of the fundamental processes of null collapse, magnetic annihilation and magnetic reconnection both in two dimensions and in three dimensions.

In chapter 2, we deal with asymmetric nulls due to a stagnation point flow and chapter 3 sees the extension of the Craig-Fabling spine annihilation results. Chapters 4 and 5 are concerned with the collapse of 2D and 3D nulls, respectively, and chapter 6 introduces preliminary numerical simulations of the simple coronal heating model suggested by Priest *et al* (2002). Finally, my conclusions and ideas for further work are presented.

Chapter 2

Stagnation-Point Flow and Asymmetric Boundary Conditions

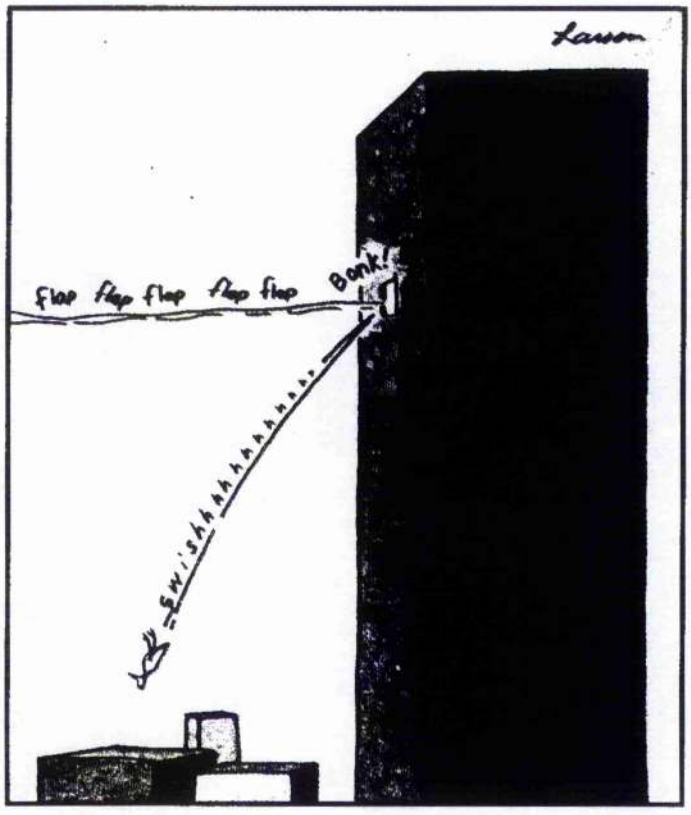

2.1 Introduction

Parker (1973) and Sonnerup and Priest (1975) derived the stagnation-point flow solution (1.63) assuming that the stagnation point of the plasma flow coincided with the null point of the magnetic field. In this chapter, we look briefly at the case where the null and stagnation point do not coincide, which is a more physically realistic assumption.

We will once again assume that the stagnation point is at the origin, without loss of generality, but we will allow the magnetic field there to be non-zero by introducing an asymmetry to the boundary conditions.

2.2 The Model

Starting with Ohm's Law,

$$\mathbf{E} + \mathbf{v} \times \mathbf{B} = \eta \nabla \times \mathbf{B}, \tag{2.1}$$

we take

$$v_x = \frac{-v_e x}{L_e}, \quad v_y = \frac{v_e y}{L_e}, \quad \mathbf{B} = B(x)\hat{\mathbf{y}}, \quad \mathbf{E} = E\hat{\mathbf{z}},$$

where E is constant due to Faraday's law. This reduces to an ordinary differential equation in the z- direction

$$E - \frac{v_e}{L_e} x B = \eta \frac{dB}{dx}. \tag{2.2}$$

Non-dimensionalising, using

$$X = \frac{x}{L_e}, \quad E^* = \frac{E}{v_e B_e}, \quad B^* = \frac{B}{B_e}, \quad R_{me} = \frac{v_{Ae} L_e}{\eta}, \quad M_e = \frac{v_e}{v_{Ae}},$$

where $-B_e$ is the field strength, and M_e and R_{me} are the Alfvén Mach number and magnetic Reynolds number respectively at $x = -L_e$, Equation (2.2) becomes

$$\frac{dB^*}{dX} + R_{me} M_e B^* X = E^* R_{me} M_e. \tag{2.3}$$

The general solution of (2.3) is

$$B^* = E^* R_{me} M_e \mathrm{daw}\left(\left(\frac{R_{me} M_e}{2}\right)^{1/2} X\right) + B_0^* \exp\left(-\frac{R_{me} M_e}{2} X^2\right), \tag{2.4}$$

where daw(t) is the Dawson function described in chapter 1 and B_0^* is an arbitrary constant. Implementing the boundary conditions

$$B^*(X=-1)=-1, \quad B^*(X=1)=1+\lambda, \tag{2.5}$$

say, determines B_0^* and E^* and gives

$$B^*(X)=\left(\frac{\lambda+2}{2}\right)\frac{\mathrm{daw}\left(\left(\frac{R_{me}M_e}{2}\right)^{1/2}X\right)}{\mathrm{daw}\left(\left(\frac{R_{me}M_e}{2}\right)^{1/2}\right)}+\frac{\lambda}{2}\frac{\exp\left(-\frac{R_{me}M_e}{2}X^2\right)}{\exp\left(-\frac{R_{me}M_e}{2}\right)}. \tag{2.6}$$

The dimensionless electric field is given by

$$E^*=\frac{2+\lambda}{2\sqrt{2R_{me}M_e}\mathrm{daw}\left(\sqrt{R_{me}M_e/2}\right)}.$$

The particular case $\lambda = 0$ recovers the stagnation-point flow result (Parker, 1973; Sonnerup & Priest, 1975). However, when $\lambda \neq 0$ there results an asymmetric magnetic field with the null point located at a point X_N determined by

$$\int_0^{(R_{me}M_e/2)^{1/2}X_N}\exp(t^2)\,dt=\frac{-\lambda}{2+\lambda}\int_0^{(R_{me}M_e/2)^{1/2}}\exp(t^2)\,dt. \tag{2.7}$$

2.3 The Permissible Size of r

The dimensionless magnetic field is

$$B^*(X)=\frac{(2+\lambda)\mathrm{daw}(rX)}{2D}+\frac{\lambda E_1}{2\exp(r^2X^2)}, \tag{2.8}$$

where $r^2 = M_eR_{me}/2$, $E_1 = \exp(r^2)$ and $D = \mathrm{daw}(r)$. A necessary but not sufficient condition to keep our external point (1,0) outside the diffusion region is that the diffusion speed must be less than the plasma velocity. This means that $M_e > 1/R_{me}$ and so $r > 1/\sqrt{2}$. This turns out to be too small a limit, as the diffusion region still extends beyond $X = 1$, and so it must be modified numerically to $r > 0.924$.

2.4 The Case With λ Varying

If we let λ vary, keeping $r > 0.924$ as discussed previously, we find that near this limit, the diffusion region moves to the left or right depending on λ. In order to keep the diffusion region

within $|X| = 1$, λ must stay small.

At $r = 0.924$, there can be no asymmetry because the diffusion region will become too large, but as r increases, the asymmetry can become larger before this happens.

2.5 Summary

We have found that due to constraints on the plasma inflow speed and the size of the diffusion region, the value of r has to be strictly limited to $r > 0.924$.

We also found that the asymmetry has to be limited. At $r = 0.924$ there can be no asymmetry due to our physical arguments.

These constraints mean that the Alfvén Mach number and annihilation rate are very small, and can be shown to go as $M_e \propto 1/R_{me}$ which is slower even than the Sweet-Parker reconnection rate. It also means that the field varies little from the original solution of Parker (1973) and Sonnerup and Priest (1975), which remains a very good approximation to the general solution.

Chapter 3

Spine Reconnective Magnetic Annihilation

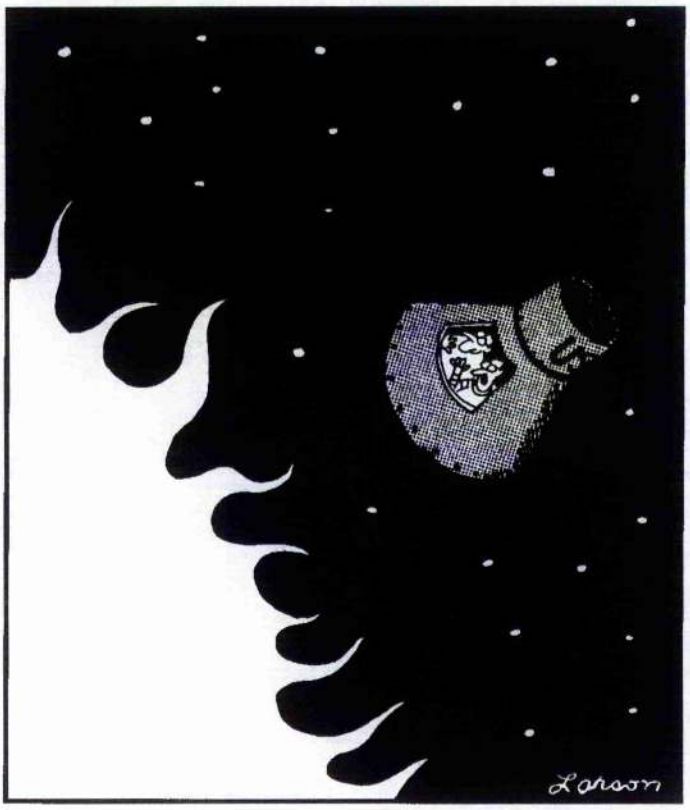

"Blast! The controls are jammed! ...
We're headed straight for Mr. Sun!"

Mellor, C., Priest, E.R. and Titov, V.S., 2002, Geophys. Astrophys. Fluid Dyn., **96** 153.

Solutions for spine reconnective annihilation are presented which satisfy exactly the three-dimensional equations of steady-state resistive incompressible magnetohydrodynamics (MHD). The magnetic flux function (A) and stream function (Ψ) have the form

$$A = A_0(R)\sin\phi + A_1(R)z, \quad \Psi = \Psi_0(R)\sin\phi + \Psi_1(R)z,$$

in terms of cylindrical polar coordinates (R, ϕ, z). First of all, two nonlinear fourth-order equations for A_1 and Ψ_1 are solved by the method of matched asymptotic expansions when the magnetic Reynolds number is much larger than unity. The solution, for which a composite asymptotic expansion is given in closed form, possesses a weak boundary layer near the spine ($R = 0$). These solutions are used to solve the remaining two equations for A_0 and Ψ_0. Physically, the magnetic field is advected across the fan separatrix surface and diffuses across the spine curve. Different members of a family of solutions are determined by values of a free parameter (γ) and the components (B_{Re}, B_{ze}) and (v_{Re}, v_{ze}) of the magnetic field and plasma velocity at a fixed external point $(R, \phi, z) = (1, \pi/2, 0)$, say.

The purpose of this chapter is to present some new exact solutions for spine reconnective annihilation that are much more general than the previous Craig-Fabling (1996) solutions and to find explicit expressions for them to leading order in η. After presenting the basic equations and the form for the new solutions in terms of the variables A_1, Ψ_1, A_0, Ψ_0 as functions of R (Section 3.1.2), we change the variables to $(a_1, \psi_1, a_0, \psi_0, s)$ to simplify the equations. In Section 3.2 we give the boundary-layer solutions of the nonlinear equations for a_1 and ψ_1, while in Section 3.3 we use the solutions found in Section 3.2 to solve the equations for a_0 and ψ_0. The basic properties of the solutions are developed in Sections 3.4 and 3.5.

3.1 Form for new exact solutions

3.1.1 Basic equations

The basic MHD equations for steady incompressible three-dimensional flow are the induction equation,

$$\nabla \times (\mathbf{v} \times \mathbf{B}) + \eta \nabla^2 \mathbf{B} = \mathbf{0} \tag{3.1}$$

and the equation of motion

$$\rho(\mathbf{v} \cdot \nabla)\mathbf{v} = -\nabla\left(p + \frac{B^2}{2\mu}\right) + (\mathbf{B} \cdot \nabla)\frac{\mathbf{B}}{\mu}, \tag{3.2}$$

where

$$\nabla \cdot \mathbf{B} = \nabla \cdot \mathbf{v} = 0, \tag{3.3}$$

in terms of the magnetic field (**B**) and the plasma velocity (**v**). The plasma density (ρ) and magnetic diffusivity (η) are assumed uniform and the electric current is

$$\mathbf{j} = \frac{1}{\mu}\nabla \times \mathbf{B}.$$

The equations (3.3) may be satisfied identically by writing the velocity and magnetic field in terms of the flux function (A) and stream function (Ψ) as

$$\mathbf{B} = -\nabla \times (A\hat{\phi}), \quad \mathbf{v} = -\nabla \times (\Psi\hat{\phi}).$$

In what follows we set $L_e = 1$, $\mu = 1$, $\rho = 1$ without loss of generality, since this is equivalent to rescaling distances with respect to the distance (L_e) from the origin at which $v = v_e$, rescaling the density with respect to ρ and absorbing μ in **B**.

3.1.2 Proposed new solutions

The form for the new solutions that we seek in cylindrical polar coordinates (R, ϕ, z) is

$$A = A_0^*(R,\phi) + A_1(R)z, \quad \Psi = \Psi_0^*(R,\phi) + \Psi_1(R)z,$$

with four free functions. The corresponding magnetic field and velocity are

$$\mathbf{B} = -\nabla \times (A\hat{\phi}), \quad \mathbf{v} = -\nabla \times (\Psi\hat{\phi}),$$

and have components

$$B_R = A_1, \quad B_\phi = 0, \quad B_z = -\dot{A}_0^* - \dot{A}_1 z, \tag{3.4}$$

$$v_R = \Psi_1, \quad v_\phi = 0, \quad v_z = -\dot{\Psi}_0^* - \dot{\Psi}_1 z. \tag{3.5}$$

The induction equation, $\nabla \times (\mathbf{v} \times \mathbf{B}) - \eta\nabla \times (\nabla \times \mathbf{B}) = 0$, becomes

$$\begin{aligned}&\left[\Psi_1\dot{A}_1 - A_1\dot{\Psi}_1, 0, \left(A_1\dot{\Psi}_0^* - \Psi_1\dot{A}_0^*\right)^{\cdot} + z\left(A_1\dot{\Psi}_1 - \Psi_1\dot{A}_1\right)^{\cdot}\right] \\ &\quad -\eta\left[-(\dot{A}_1)', 0, \left(\left[\dot{A}_0^* + \dot{A}_1 z\right]'\right)^{\cdot} + (\partial\dot{A}_0^*/\partial\phi^2)/r^2\right] = 0,\end{aligned} \tag{3.6}$$

and the curl of the momentum equation, $M = \nabla \times ([\mathbf{v}\cdot\nabla]\mathbf{v} - [\mathbf{B}\cdot\nabla]\mathbf{B}) = 0$, becomes

$$\begin{aligned} M_R &= (-1/R)\partial\left(\Psi_1(\dot{\Psi}_0^*)' - \dot{\Psi}_0^*\dot{\Psi}_1 - A_1(\dot{A}_0^*)' + \dot{A}_0^*\dot{A}_1\right)/\partial\phi, \\ M_\phi &= \partial\left(\Psi_1(\dot{\Psi}_0^*)' - \dot{\Psi}_0^*\dot{\Psi}_1 - A_1(\dot{A}_0^*)' + \dot{A}_0^*\dot{A}_1\right)/\partial R \\ &+ z\partial\left(-(\dot{\Psi}_1)^2 + \Psi_1\dot{\Psi}_1{}' + (\dot{A}_1)^2 - A_1\dot{A}_1{}'\right)/\partial R, \\ M_z &= 0, \end{aligned} \tag{3.7}$$

where $\dot{f} \equiv R^{-1}\partial(Rf)/\partial R$ and $g' \equiv \partial g/\partial R$. This represents a special case in which the angular components of field and flow (B_ϕ and v_ϕ) are both zero.

Setting coefficients of z^0 and z^1 to zero, the steady-state induction equation (3.6) and the curl of the momentum equation (3.7) can be used to show that

$$A_1\dot{\Psi}_1 - \Psi_1\dot{A}_1 + \eta\frac{d\dot{A}_1}{dR} = 0, \tag{3.8}$$

$$-(\dot{\Psi}_1)^2 + \Psi_1\frac{d\dot{\Psi}_1}{dR} + (\dot{A}_1)^2 - A_1\frac{d\dot{A}_1}{dR} = -k, \tag{3.9}$$

$$\left(A_1\dot{\Psi}_0^* - \Psi_1\dot{A}_0^* + \eta\frac{\partial\dot{A}_0^*}{\partial R}\right)^{\cdot} = -\frac{\eta}{R^2}\frac{\partial^2\dot{A}_0^*}{\partial\phi^2}, \tag{3.10}$$

$$\Psi_1\frac{\partial\dot{\Psi}_0^*}{\partial R} - \dot{\Psi}_0^*\dot{\Psi}_1 - A_1\frac{\partial\dot{A}_0^*}{\partial R} + \dot{A}_0^*\dot{A}_1 = L, \tag{3.11}$$

where k and L are constants of integration. Possible functions of integration can be reduced to constants because of the assumed form of the solution.

There are eight natural boundary conditions that we impose, namely, $\mathbf{B} = \mathbf{v} = \mathbf{0}$ at the origin and $\mathbf{B} = \mathbf{B_e}$ and $\mathbf{v} = \mathbf{v_e}$ at the external point $(R,\phi,z) = (1,\pi/2,0)$ or, in terms of the flux function and stream function, $A_1(0) = \Psi_1(0) = 0$, $A_1(1) = B_{Re}$, $\Psi_1(1) = v_{Re}$, $\dot{A}_0^*(0) = \dot{\Psi}_0^*(0) = 0$, $\dot{A}_0^*(1) = -B_{ze}$ and $\dot{\Psi}_0^*(1) = -v_{ze}$.

Equations 3.8 and 3.9 are second order in both A_1 and Ψ_1. The four boundary conditions on these are sufficient to solve them. Equations 3.10 and 3.11 are second order in $\dot{A}_0^*$ but only first order in $\dot{\Psi}_0^*$. The four boundary conditions are such as to solve the equations and also to make the constant L disappear.

Equations (3.8) and (3.9) for A_1 and Ψ_1 decouple from the other two equations. Equations (3.10) and (3.11) for A_0^* and Ψ_0^* are linear (if A_1 and Ψ_1 are known) and so their general solution

may be found by expanding A_0^* and Ψ_0^* in Fourier series of the form

$$A_0^*(R,\phi) = \sum_{m=0}^{\infty} A_m(R)\sin([m+1]\phi) + \sum_{m=-1}^{\infty} C_m(R)\cos([m+1]\phi)$$

However, the fundamental ($m = 0$) mode is the most interesting since it is the only one that is reconnective (Craig *et al*, 1995). In this chapter we concentrate only on this mode from now on by replacing A_0^* and Ψ_0^* by $A_0 \sin\phi$ and $\Psi_0 \sin\phi$ and hope to address other possibilities in the future. Even though Lin (1958) suggested such solutions as a form of exact solution of the MHD equations, this has not previously been used for the reconnection problem.

These equations simplify greatly by making the substitutions $a = RA, \psi = R\Psi$ and $s = R^2/2$, for which the equations (3.8)-(3.11) become

$$a_1\frac{d\psi_1}{ds} - \psi_1\frac{da_1}{ds} + 2\eta s\frac{d^2a_1}{ds^2} = 0, \tag{3.12}$$

$$-\left(\frac{d\psi_1}{ds}\right)^2 + \psi_1\frac{d^2\psi_1}{ds^2} + \left(\frac{da_1}{ds}\right)^2 - a_1\frac{d^2a_1}{ds^2} = -k, \tag{3.13}$$

$$\frac{d}{ds}\left(a_1\frac{d\psi_0}{ds} - \psi_1\frac{da_0}{ds} + 2\eta s\frac{d^2a_0}{ds^2}\right) = \frac{\eta}{2s}\frac{da_0}{ds}, \tag{3.14}$$

$$\psi_1\frac{d^2\psi_0}{ds^2} - \frac{d\psi_0}{ds}\frac{d\psi_1}{ds} - a_1\frac{d^2a_0}{ds^2} + \frac{da_0}{ds}\frac{da_1}{ds} = 0. \tag{3.15}$$

The boundary conditions are now $a_1(0) = \psi_1(0) = 0$, $a_1(1/2) = B_{Re}$, $\psi_1(1/2) = v_{Re}$, $(da_0/ds)(0) = (d\psi_0/ds)(0) = 0$, $(da_0/ds)(1/2) = -B_{ze}$ and $(d\psi_0/ds)(1/2) = -v_{ze}$.

3.2 Solution for a_1 and ψ_1

We seek the solution of (3.12) and (3.13) subject to the given boundary conditions by using the method of matched asymptotic expansions, with an outer solution over most of the range ($0 < s \leq 1/2$) and an inner (boundary-layer) solution near $s = 0$. We are able to show that the outer solution is a uniformly valid solution to leading order for all s in the range $0 \leq s \leq 1/2$. A Taylor-series expansion about $s = 0$ gives

$$a_1 = a_{11}s + a_{14}s^4 + a_{15}s^5 + \ldots,$$

$$\psi_1 = \psi_{11}s + \psi_{13}s^3 + \psi_{14}s^4 + \psi_{15}s^5 + \ldots,$$

which is used later to start the numerical integration of the equations from $s = 0$. The inner boundary condition results in the coefficients $a_{12} = a_{13} = \psi_{12} = 0$ for the relevant terms in s^2

and s^3. The absence of these terms in the Taylor expansions implies that $d^3a_1/ds^3(0) \equiv 0$. Also, substitution into the differential equations gives the relation $a_{11}^2 - \psi_{11}^2 = -k$.

3.2.1 Outer solution

The outer solution can be obtained by expanding in powers of η and matching terms of the same order in η. The first of these terms can be found by setting $\eta = 0$ in (3.12), integrating and using the outer boundary conditions to give

$$\psi_1 = \frac{v_{Re}}{B_{Re}} a_1. \tag{3.16}$$

Eliminating ψ_1 from (3.13) gives a second-order equation in a_1 that may be solved to give three different forms for the solution depending on the values of a positive parameter, γ, in terms of which

$$k = \frac{4(v_{Re}^2 - B_{Re}^2)}{\gamma^2} > 0. \tag{3.17}$$

The parameter, k is positive so that the calculation for the thickness of the current tube to be carried out later in (3.47) is valid for the inflowing boundary that we assume. If $\gamma = 1$, we have

$$a_1 = 2B_{Re}s, \quad \psi_1 = 2v_{Re}s. \tag{3.18}$$

If $\gamma < 1$, then by using a new parameter, λ, such that $(\sin\lambda)/\lambda = \gamma$, we obtain

$$a_1 = B_{Re}\frac{\sin(2\lambda s)}{\sin\lambda}, \quad \psi_1 = v_{Re}\frac{\sin(2\lambda s)}{\sin\lambda}. \tag{3.19}$$

If $\gamma > 1$, then

$$a_1 = B_{Re}\frac{\sinh(2\Lambda s)}{\sinh\Lambda}, \quad \psi_1 = v_{Re}\frac{\sinh(2\Lambda s)}{\sinh\Lambda}, \tag{3.20}$$

where the new parameter, Λ, is such that $(\sinh\Lambda)/\Lambda = \gamma$.

The variation of λ and Λ with γ is shown in Figure 3.1.

The solutions (3.18), (3.19) and (3.20) satisfy, for any value of γ, both the outer and the inner boundary conditions. However, if $\gamma \neq 1$, they do not satisfy the full equations (3.12) and (3.13) with $\eta \neq 0$. For example, they have $d^3a_1/ds^3(0) \neq 0$, whereas we saw from the series expansion about $s = 0$ that $d^3a_1/ds^3(0) \equiv 0$. Hence a boundary layer near the origin is needed to bring d^3a_1/ds^3 down to zero as the origin is approached so as to accommodate this implicit boundary

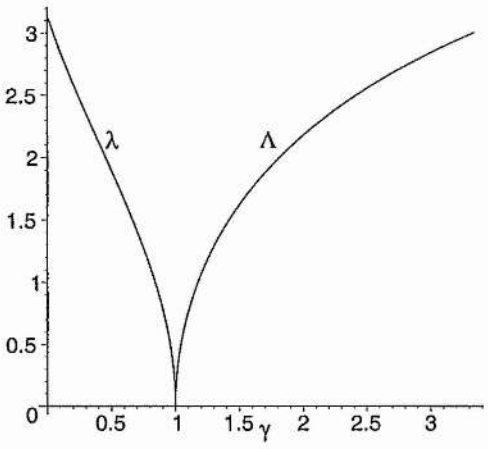

Figure 3.1: The variation of λ and Λ with the parameter γ.

condition.

3.2.2 Inner solution

The boundary-layer equations are obtained by rescaling the dependent and independent variables in (3.12) and (3.13) in the following way

$$a_1 = \eta \bar{a_1}, \quad \psi_1 = \eta \bar{\psi_1}, \quad s = \eta \bar{s}. \tag{3.21}$$

The resulting equations in place of (3.12) and (3.13) are

$$\bar{a_1}\bar{\psi_1}' - \bar{\psi_1}\bar{a_1}' + 2\bar{s}\bar{a_1}'' = 0, \tag{3.22}$$

and

$$-(\bar{\psi_1}')^2 + \bar{\psi_1}\bar{\psi_1}'' + (\bar{a_1}')^2 - \bar{a_1}\bar{a_1}'' = -k, \tag{3.23}$$

where $f' \equiv df/d\bar{s}$. The boundary conditions for the inner solution become $\bar{a_1}(0) = 0$, $\bar{\psi_1}(0) = 0$, $\bar{a_1}'''(0) = 0$ and $\bar{\psi_1}'''(0) = 6\eta^2\psi_{13}$.
Setting

$$\bar{a_1} = a_{11}\bar{s} + \eta^2\tilde{a_1}, \quad \bar{\psi_1} = \psi_{11}\bar{s} + \eta^2\tilde{\psi_1},$$

and substituting into (3.22) and (3.23) reduces them to a pair of linear equations

$$a_{11}(\bar{s}\tilde{\psi_1}' - \tilde{\psi_1}) - \psi_{11}(\bar{s}\tilde{a_1}' - \tilde{a_1}) - 2\bar{s}\tilde{a_1}'' = 0, \tag{3.24}$$

and

$$\psi_{11}(\bar{s}\tilde{\psi_1}'' - 2\tilde{\psi_1}') - a_{11}(\bar{s}\tilde{a_1}'' - 2\tilde{a_1}') = 0, \tag{3.25}$$

for which the boundary conditions are

$$\tilde{a_1}(0) = \tilde{\psi_1}(0) = \tilde{a_1}'(0) = \tilde{\psi_1}'(0) = 0, \qquad \tilde{\psi_1}'''(0) = 6\psi_{13}.$$

Equation (3.25) can be integrated twice to give

$$\psi_{11}\tilde{\psi_1} - a_{11}\tilde{a_1} = \psi_{11}\psi_{13}\bar{s}^3. \tag{3.26}$$

Using this to eliminate $\tilde{\psi_1}$ from (3.24) and with $\sigma^2 = -k/\psi_{11}$, we then find

$$2\bar{s}\tilde{a_1}'' + \sigma^2(\bar{s}\tilde{a_1}' - \tilde{a_1}) + 2a_{11}\psi_{13}\bar{s}^3 = 0. \tag{3.27}$$

This can be manipulated to yield

$$\frac{d}{d\bar{s}}\left(\frac{\tilde{a_1}}{\bar{s}}\right) = -a_{11}\psi_{13}\frac{1}{\bar{s}^2}\exp\left(-\frac{\sigma^2}{2}\bar{s}\right)\int_0^{\bar{s}} t^3\exp\left(\frac{\sigma^2}{2}t\right)dt, \tag{3.28}$$

which may be integrated to give an explicit solution for $\tilde{a_1}$.

Expanding for small $\bar{s}$ gives

$$\tilde{a_1} = -\frac{a_{11}\psi_{13}}{12}\bar{s}^4 + \ldots,$$

$$\tilde{\psi_1} = \psi_{13}\bar{s}^3 - \frac{a_{11}^2\psi_{13}}{12\psi_{11}}\bar{s}^4 + \ldots.$$

Expanding instead for large $\bar{s}$ gives

$$\tilde{a_1} = -\frac{a_{11}\psi_{13}}{\sigma^2}\bar{s}^3 + \frac{12a_{11}\psi_{13}}{\sigma^4}\bar{s}^2 + O\left(\bar{s}\ln(\bar{s})\right),$$

$$\tilde{\psi_1} = \psi_{13}\left(1 - \frac{a_{11}^2}{\sigma^2\psi_{11}}\right)\bar{s}^3 - \frac{12a_{11}^2\psi_{13}}{\sigma^4\psi_{11}}\bar{s}^2 + O\left(\bar{s}\ln(\bar{s})\right).$$

3.2.3 Matching

In order to match the inner solution (3.28) and the outer solutions (3.18), (3.19) and (3.20), we now express the inner solution in terms of the outer variable (s) and expand for small η, so that

$$a_1 = a_{11}s - \frac{a_{11}\psi_{13}}{\sigma^2}s^3 + O(\eta). \tag{3.29}$$

Similarly, we expand the outer solution in terms of the inner variable for small η. When $\gamma < 1$ we obtain

$$a_1 = \frac{2\lambda B_{Re}}{\sin\lambda} s - \frac{4\lambda^3 B_{Re}}{3\sin\lambda} s^3 + \dots . \tag{3.30}$$

Clearly the two solutions (3.29) and (3.30) can be matched provided

$$a_{11} = \frac{2\lambda B_{Re}}{\sin\lambda}, \quad \psi_{13} = -\frac{2\lambda^2 k}{3\psi_{11}}.$$

The outer solution (3.19) represents a composite solution to leading order.

When $\gamma > 1$, the same solution is obtained but with λ and λ^2 replaced by Λ and $(-\Lambda^2)$, respectively. Finally, when $\gamma = 1$ we find that the solution $a_1 = 2B_{Re}s$ is valid everywhere.

The numerical solutions for a_1 and ψ_1 to the full equations (3.12) and (3.13) are shown in Figure 3.2, which gives the $\gamma < 1$ solutions with $\eta = 0.01$, $B_{Re} = 2$, $\lambda = 2$ and $k = 500$. The top part of Figure 3.3 shows the boundary layer for $\eta = 0.01$ with the inner solution (dotted line) and the outer solution (dashed line) imposed over the numerical solution (solid line). The bottom part shows that the boundary layer varies in width for different values of η. The lowest curve is for $\eta = 0.001$, the next two curves are for $\eta = 0.003$ and $\eta = 0.01$ and the uppermost curve is for $\eta = 0.03$. The width of the boundary layer in each case is approximately η.

3.3 Solution for a_0 and ψ_0

Having found the solutions to leading order for a_1 and ψ_1, we now seek the solution of (3.14) and (3.15) for $a_0(s)$ and $\psi_0(s)$ subject to the conditions that $(da_0/ds)(0) = (d\psi_0/ds)(0) = 0$.

Again, solving the equations by the method of matched asymptotic expansions, we start with the Taylor-series expansions for a_0 and ψ_0. These are

$$a_0 = a_{00} + a_{03}s^3 + a_{04}s^4 + \dots ,$$

$$\psi_0 = \psi_{00} + \psi_{02}s^2 + \psi_{03}s^3 + \psi_{04}s^4 + \dots .$$

The coefficients a_{00} and ψ_{00} are arbitrary, but are set to zero to avoid a singularity at $R = 0$ when we change back to the original coordinates. All the other coefficients can be found in terms of ψ_{02} and the coefficients a_{11} and ψ_{13} of the Taylor series for a_1 and ψ_1.

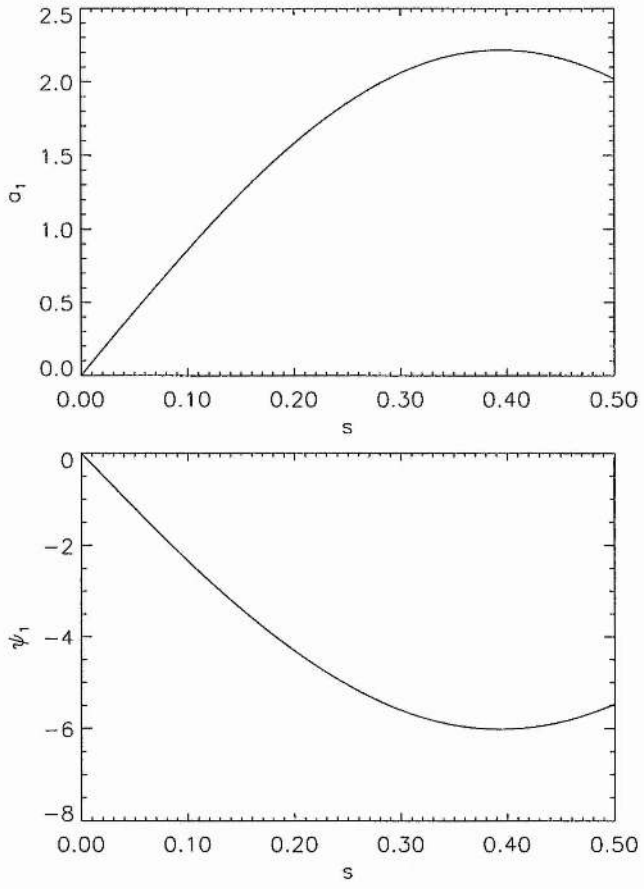

Figure 3.2: *(Top)* a_1 as a function of s for $\eta = 0.01$, $B_{Re} = 2$, $\lambda = 2$ and $k = 500$. *(Bottom)* ψ_1 as a function of s for $\eta = 0.01$, $B_{Re} = 2$, $\lambda = 2$ and $k = 500$.

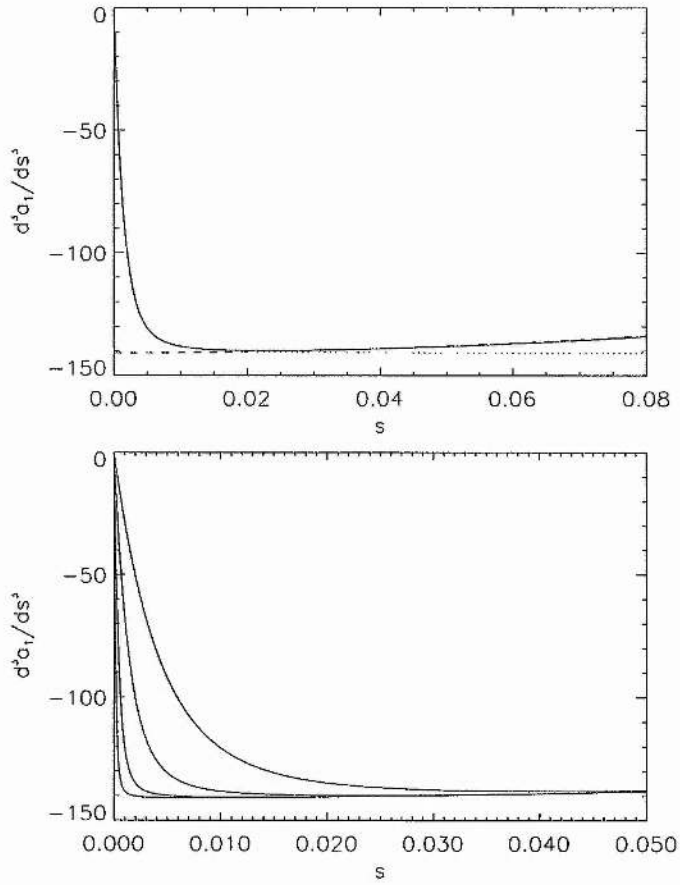

Figure 3.3: *(Top)* d^3a_1/ds^3 as a function of s showing the boundary-layer nature of the solution. The solid curve is the full numerical solution, the dashed curve is the outer solution and the dotted curve the inner solution. *(Bottom)* d^3a_1/ds^3 as a function of s for the values $\eta = 0.001, 0.003, 0.01$ and 0.03 that increase from left to right as the width of the boundary layer increases. All other parameters are as in Figure 3.2.

3.3.1 Outer solution

To find the solution to leading order, again we set $\eta = 0$. After integrating and using the outer boundary conditions, we obtain

$$a_1 \frac{d\psi_0}{ds} - \psi_1 \frac{da_0}{ds} = B_{ze} v_{Re} - B_{Re} v_{ze}.$$

Using the relation (3.16), we find

$$\frac{d\psi_0}{ds} = \frac{v_{Re}}{B_{Re}} \frac{da_0}{ds} + \frac{B_{ze} v_{Re} - B_{Re} v_{ze}}{a_1}.$$

Eliminating ψ_0 from (3.15) yields

$$\frac{da_0}{ds} = \frac{v_{Re} v_{ze} - B_{Re} B_{ze}}{B_{Re}^2 - v_{Re}^2} a_1 + \frac{(B_{ze} v_{Re} - B_{Re} v_{ze}) B_{Re} v_{Re}}{B_{Re}^2 - v_{Re}^2} \frac{1}{a_1}, \tag{3.31}$$

$$\frac{d\psi_0}{ds} = \frac{(v_{Re} v_{ze} - B_{Re} B_{ze}) v_{Re}}{(B_{Re}^2 - v_{Re}^2) B_{Re}} a_1 + \frac{(B_{ze} v_{Re} - B_{Re} v_{ze}) B_{Re}^2}{B_{Re}^2 - v_{Re}^2} \frac{1}{a_1}. \tag{3.32}$$

So the form of a_0 depends on a_1 and therefore the value of γ.
For small s, da_0/ds expands as

$$\frac{da_0}{ds} = \left(\frac{\gamma B_{Re} v_{Re} (B_{ze} v_{Re} - B_{Re} v_{ze})}{2(B_{Re}^2 - v_{Re}^2)} \right) \frac{1}{s} + \left(\frac{2(v_{Re} v_{ze} - B_{Re} B_{ze})}{\gamma (B_{Re}^2 - v_{Re}^2)} + \frac{\lambda^2 \gamma B_{Re} v_{Re} (B_{ze} v_{Re} - B_{Re} v_{ze})}{3(B_{Re}^2 - v_{Re}^2)} \right) s + \ldots, \tag{3.33}$$

for $\gamma < 1$. For the $\gamma > 1$ case, λ^2 is replaced with $-\Lambda^2$ as before. As λ or Λ tend to zero, $\gamma \to 1$, and we can neglect the term in λ or Λ.

3.3.2 Inner solution

Again, setting $a = \eta \bar{a}$, $\psi = \eta \bar{\psi}$ and $s = \eta \bar{s}$, equations (3.14) and (3.15) imply

$$\left(\bar{a}_1 \bar{\psi}_0{}' - \bar{\psi}_1 \bar{a}_0{}' + 2\bar{s} \bar{a}_0{}'' \right)' = \frac{\bar{a}_0{}'}{2\bar{s}}, \tag{3.34}$$

and

$$\bar{\psi}_1 \bar{\psi}_0{}'' - \bar{\psi}_0{}' \bar{\psi}_1{}' - \bar{a}_1 \bar{a}_0{}'' + \bar{a}_0{}' \bar{a}_1{}' = 0, \tag{3.35}$$

with boundary conditions $\bar{a}_0{}'(0) = \bar{\psi}_0{}'(0) = 0$, $\bar{a}_0{}''(0) = 0$ and $\bar{\psi}_0{}''(0) = 2\eta\psi_{02}$.
Again, $x' \equiv dx/d\bar{s}$.

Then putting

$$\tilde{a_0} = \eta\tilde{a_0}, \quad \tilde{\psi_0} = \eta\tilde{\psi_0},$$

$$\tilde{a_1} = a_{11}\bar{s} + \eta^2\tilde{a_1}, \quad \tilde{\psi_1} = \psi_{11}\bar{s} + \eta^2\tilde{\psi_1},$$

we obtain the linear equations

$$\left(a_{11}\bar{s}\tilde{\psi_0}' - \psi_{11}\bar{s}\tilde{a_0}' + 2\bar{s}\tilde{a_0}''\right)' = \frac{\tilde{a_0}'}{2\bar{s}}, \tag{3.36}$$

and

$$\psi_{11}\bar{s}\tilde{\psi_0}'' - \psi_{11}\tilde{\psi_0}' - a_{11}\bar{s}\tilde{a_0}'' + a_{11}\tilde{a_0}' = 0. \tag{3.37}$$

Integrating (3.37) and using the boundary conditions $\tilde{a_0}'' = 0$ and $\tilde{\psi_0}'' = 2\psi_{02}$ gives the relation

$$\psi_{11}\tilde{\psi_0}' - a_{11}\tilde{a_0}' = 2\psi_{11}\psi_{02}\bar{s}. \tag{3.38}$$

Using it to eliminate $\tilde{\psi_0}'$ from equation (3.36) we find

$$4\bar{s}^2\tilde{a_0}''' + (2\sigma^2\bar{s}^2 + 4\bar{s})\tilde{a_0}'' + (2\sigma^2\bar{s} - 1)\tilde{a_0}' = -8a_{11}\psi_{02}\bar{s}^2, \tag{3.39}$$

where $\sigma^2 = -k/\psi_{11}$ as before.

Solving for small $\bar{s}$ gives

$$\tilde{a_0} = -\frac{8a_{11}\psi_{02}}{45}\bar{s}^3 + \ldots,$$

which comes entirely from the particular integral of the solution, so there are no complementary functions associated with the solution, and

$$\tilde{\psi_0} = \psi_{02}\bar{s}^2 - \frac{8a_{11}^2\psi_{02}}{45\psi_{11}}\bar{s}^3 + \ldots.$$

Solving for large $\bar{s}$ gives

$$\tilde{a_0}' = -\frac{2a_{11}\psi_{02}}{\sigma^2}\bar{s} + \frac{3a_{11}\psi_{02}}{\sigma^4} + \frac{C}{\bar{s}} + O\left(\frac{1}{\bar{s}^2}\right)$$

and

$$\tilde{\psi_0}' = \left(2\psi_{02} - \frac{2a_{11}^2\psi_{02}}{\psi_{11}\sigma^2}\right)\bar{s} + \frac{3a_{11}^2\psi_{02}}{\psi_{02}\sigma^4} + \frac{a_{11}C}{\psi_{11}\bar{s}} + O\left(\frac{1}{\bar{s}^2}\right)$$

where C is an arbitrary constant as the $\bar{s}^{-1}$ term is part of a complimentary function solution and

hence must be equal to zero.

3.3.3 Matching

We now express the inner solution in terms of the outer variable s and expand for small η, so that

$$\frac{da_0}{ds} = -\frac{2a_{11}\psi_{02}}{\sigma^2}\, s + \dots \tag{3.40}$$

And from (3.33) we can see that these solutions match if

$$\psi_{02} = \frac{k}{2a_{11}\psi_{11}}\left(\frac{2(v_{Re}v_{ze} - B_{Re}B_{ze})}{\gamma(B_{Re}^2 - v_{Re}^2)} + \frac{\lambda^2\gamma B_{Re}v_{Re}(B_{ze}v_{Re} - B_{Re}v_{ze})}{3(B_{Re}^2 - v_{Re}^2)}\right) \tag{3.41}$$

with γ and λ^2 changing as before for the $\gamma \geq 1$ cases. The s^{-1} term must be matched at a higher order in η.

3.4 Properties of solutions

In this section, figures showing the behaviour of the leading-order outer solutions are presented. In cylindrical polar coordinates, in order to find the streamlines of the flux function or stream function, we can use the fact that RA = constant along a field line or $R\Psi$ = constant along a streamline in a plane of constant ϕ. In other words, $a = RA$ and $\psi = R\Psi$, when expressed in terms of R are the flux and stream functions. The equation for the fieldline surfaces is $RA_1 z + RA_0 \sin\phi = c$ and the equation for the streamline surfaces is $R\Psi_1 z + R\Psi_0 \sin\phi = c$, where c is an arbitrary constant which varies from one surface to another.

3.4.1 Fieldlines and streamlines

Shown in the figures 3.5 - 3.7 are surfaces of fieldlines and streamlines found using the outer solutions for A_1, Ψ_1, A_0 and Ψ_0. The field and stream lines are radial, as indicated by the selection of lines on the figures. The boundary conditions for the figures are $B_{Re} = 3$, $v_{Re} = -10$, $B_{ze} = -11$ and $v_{ze} = 1$.

Figure 3.5 gives flux and stream surfaces for $c = 0$ and 5 and $\gamma < 1$, while Figures 3.6 and 3.7 give them for $\gamma = 1$ and $\gamma > 1$, respectively. It can be seen that, as γ increases, the tube structures parallel to the $z-$axis grow wider for the same boundary conditions. Also, as $|c|$ increases, one of the cylinders increases in size and the other decreases. This creates a kink in the region of $R = 0$

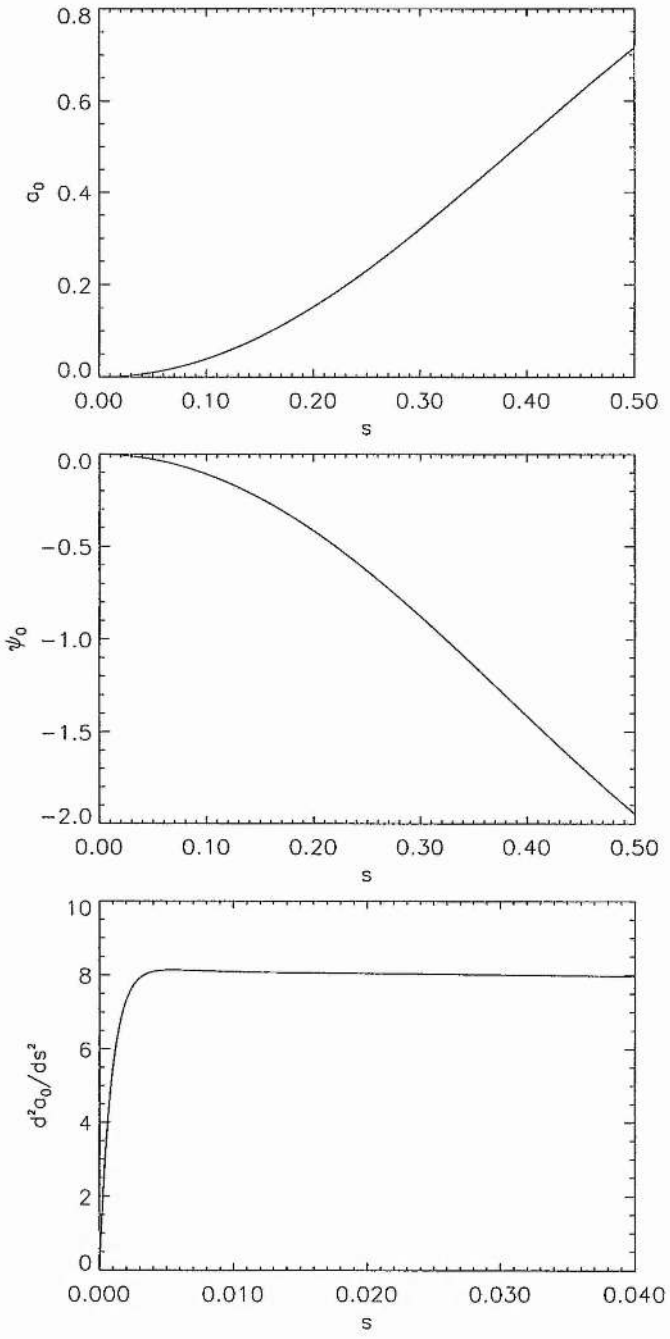

Figure 3.4: *(Top)* a_0 as a function of s. The parameters are the same as previously, with $v_{ze} = 5$ and $B_{ze} = -1.83$ also. *(Middle)* ψ_0 as a function of s. *(Bottom)* d^2a_0/ds^2 as a function of s with $\eta = 0.01$ displaying the boundary-layer nature of the solution.

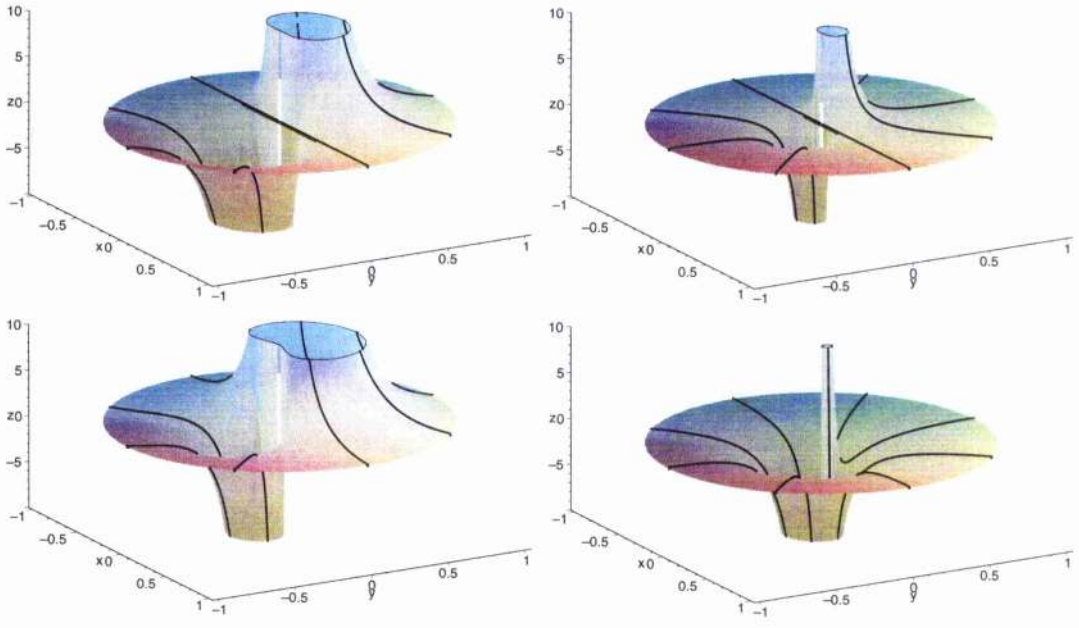

Figure 3.5: *(Top left)* Fieldlines for the case $\gamma = 0.665$ and $c = 0$. *(Top right)* Streamlines for the case $\gamma = 0.665$ and $c = 0$. *(Bottom left)* Fieldlines for the case $\gamma = 0.665$ and $c = 5$. *(Bottom right)* Streamlines for the case $\gamma = 0.665$ and $c = 5$.

as the expanding cylinder wraps around the other, as shown in Figure 3.8. Within a distance $\eta^{1/2}$ of the z-axis, a weak boundary layer occurs as described in Section 3.

3.4.2 The significance of γ

For our solutions, the $z-$derivative of the $z-$component of the magnetic tension force, $(\mathbf{B} \cdot \nabla)\mathbf{B}$, has a constant value of $4B_{Re}^2/\gamma^2$. This indicates that the significance of the value of γ is in determining how rapidly the magnetic tension force parallel to the spine line changes in space. The trigonometric solutions give a steeper gradient than the hyperbolic solutions.

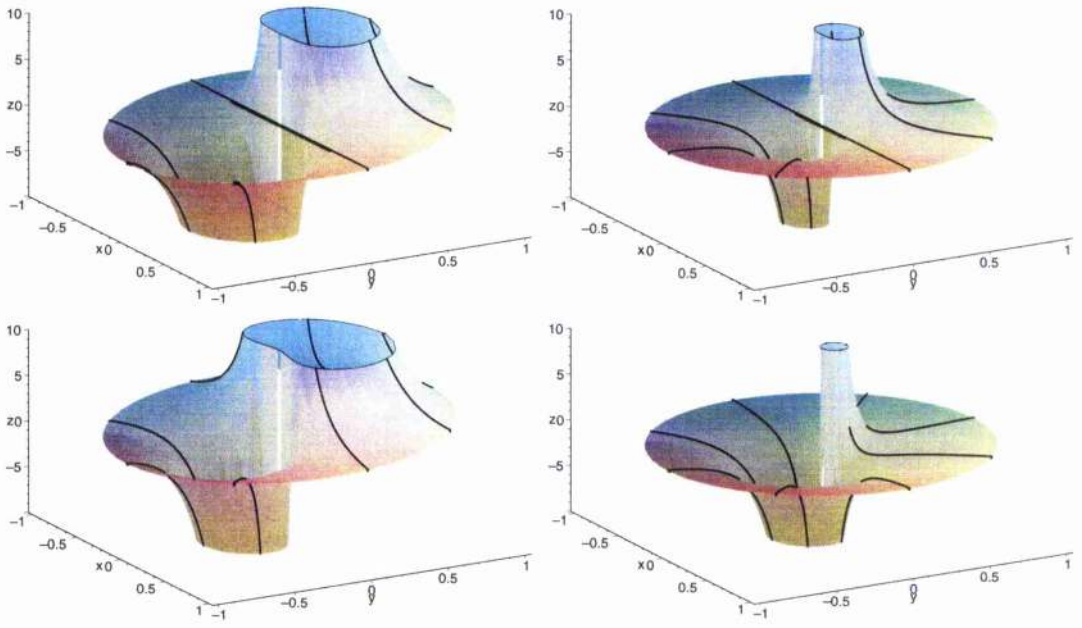

Figure 3.6: *(Top left)* Fieldlines for the case $\gamma = 1$ and $c = 0$. *(Top right)* Streamlines for the case $\gamma = 1$ and $c = 0$. *(Bottom left)* Fieldlines for the case $\gamma = 1$ and $c = 5$. *(Bottom right)* Streamlines for the case $\gamma = 1$ and $c = 5$.

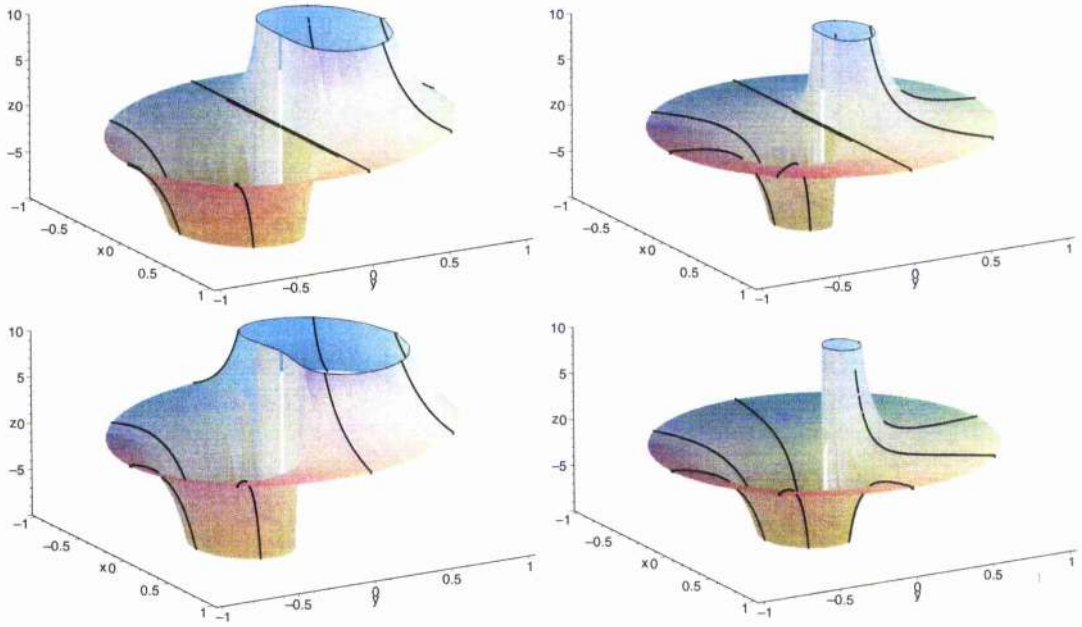

Figure 3.7: *(Top left)* Fieldlines for the case $\gamma = 1.420$ and $c = 0$. *(Right)* Streamlines for the case $\gamma = 1.420$ and $c = 0$. *(Bottom left)* Fieldlines for the case $\gamma = 1.420$ and $c = 5$. *(Bottom right)* Streamlines for the case $\gamma = 1.420$ and $c = 5$

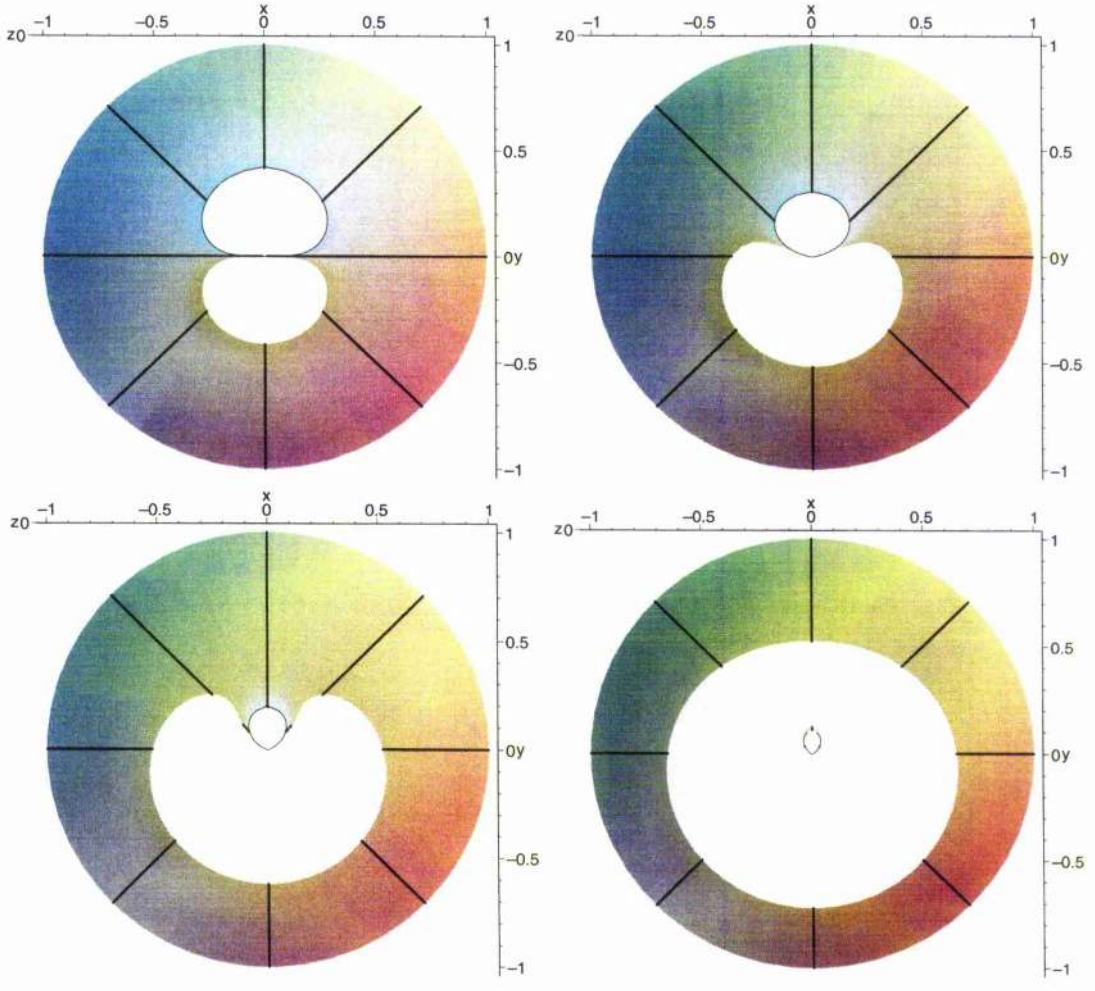

Figure 3.8: Stream surfaces viewed from above, showing that, as $|c|$ increases, one of the cylinders grows in size and wraps around the other one. This example is for $\gamma = 1.420$ and $c = 0$, 6, 12 and 18 from top left to bottom right.

3.5 Comparison of solutions

3.5.1 The solutions of Craig & Fabling

In dimensional units, the solutions of Craig & Fabling (1996) (1.77) and (1.78) can be written for our purposes as

$$v_z = -2v_{Re}z - \frac{B_{Re}}{v_{Re}} f(R)\sin\phi, \quad v_R = v_{Re}R, \tag{3.42}$$

$$B_z = -2B_{Re}z - f(R)\sin\phi, \quad B_R = B_{Re}R, \tag{3.43}$$

where substituting a sine function for a cosine function and setting $m = 1$ loses no generality but allows us to fix an external point at $(x, y, z) = (0, 1, 0)$ where the velocity and magnetic field are $\mathbf{v_e}$ and $\mathbf{B_e}$ to provide a direct comparison with the generalised solutions in this chapter. At the external point, we can see that B_{ze}, v_{ze}, v_{Re} and B_{Re} are not independent but are related by $B_{ze} = v_{Re}v_{ze}/B_{Re} = -f(1)$ in order to satisfy the boundary conditions ($B_R = B_{Re}, v_R = v_{Re}, B_z = B_{ze}, v_z = v_{ze}$) at the external point. In addition, λ and B_{Re} cannot be imposed arbitrarily since the boundary condition on B_R implies that $\lambda = B_{Re}$. This means that we can impose only three of $\lambda, v_{Re}, B_{Re}, v_{ze}$ and B_{ze}. In contrast, the new solutions presented in this chapter are such that all four of the external boundary conditions can be imposed, as well as the extra parameter, γ. This represents a two-fold generalisation of the Craig-Fabling solutions.

Setting $\gamma = 1$ and explicitly inserting it into (3.4) and (3.5), we can see that this reduces to the Craig-Fabling solution as written in (3.42) and (3.43), with $\dot{A}_0(R) = f(R)$ and $\dot{\Psi}_0(R) = (B_{Re}/v_{Re})f(R)$ satisfying both (1.79) and (3.10).

3.5.2 Differences between the 2D and 3D cases

Equation (3.11) has a right-hand side identically equal to zero, whereas the equivalent two-dimensional equation (Priest *et al*, 2000, equation (2.5)) has a non-zero right-hand side. The reason is that the parts of curl of the momentum equation (**M**), relating to equation (3.11), in three dimensions have R and ϕ components of

$$M_R = \frac{\cos\phi}{R}\left(-\Psi_1\frac{d\dot{\Psi}_0}{dR} + \dot{\Psi}_0\dot{\Psi}_1 + A_1\frac{d\dot{A}_0}{dR} - \dot{A}_0\dot{A}_1\right), \tag{3.44}$$

$$M_\phi = (\sin\phi)\frac{d}{dR}\left(\Psi_1\frac{d\dot{\Psi}_0}{dR} - \dot{\Psi}_0\dot{\Psi}_1 - A_1\frac{d\dot{A}_0}{dR} + \dot{A}_0\dot{A}_1\right), \tag{3.45}$$

which are equal to zero, whereas in two dimensions it only has a z-component, namely

$$M_z = \frac{d}{dx}\left(-\psi_1\frac{d^2\psi_0}{dx^2} + \frac{d\psi_0}{dx}\frac{d\psi_1}{dx} + A_1\frac{d^2A_0}{dx^2} - \frac{dA_0}{dx}\frac{dA_1}{dx}\right), \tag{3.46}$$

which is also equal to zero. Thus in three dimensions, the R-component (3.44) gives (3.11) with the right-hand side identically zero, while the ϕ-component (3.45) gives the derivative of (3.11). In two dimensions, however, the z-component (3.46) integrates to give Priest *et al* (2000), equation (2.5).

3.5.3 The width of the current tube

In order to estimate the width of the current tube extending up the z-axis, we consider $B_z(R,0)$ which is governed by $\dot{A}_0$. In terms of the variables (a,ψ,s) we may eliminate ψ_0 and ψ_1 from equation (3.14) using the fact that in the composite solutions for a_1 and ψ_1 there is the relation $\psi_1 = (v_{Re}/B_{Re})a_1$. The result is the following equation for a_0

$$\frac{d^3a_0}{ds^3} + \left\{\frac{1}{s} + \frac{Ka_1}{2\eta s}\right\}\frac{d^2a_0}{ds^2} + \left\{\frac{K}{2\eta s}\frac{da_1}{ds} - \frac{1}{4s^2}\right\}\frac{da_0}{ds} + \frac{Ca_1}{\eta s}\frac{da_1}{ds} = 0,$$

where $K = (B_{Re}^2 - v_{Re}^2)/(B_{Re}v_{Re})$ and $C = (B_{Re}B_{ze} - v_{Re}v_{ze})/(B_{Re}v_{Re})$. In order to estimate a length-scale (l) for the width of the spine current, we compare the highest derivative term (which gives rise to the boundary layer) in an order of magnitude way with the second term. In doing so we can make the approximations $s \sim s_0$, $a_1 \sim (2B_{Re}s_0)/\gamma$ and $(d^3a_0/ds^3) \sim (d^2a_0/ds^2)/s_0$, where $s_0 = l^2/2$. To within a numerical factor, we then find the expression

$$s_0 = \frac{\eta\gamma\, v_{Re}}{B_{Re}^2 - v_{Re}^2},$$

or in terms of the original variables

$$l = \left(\frac{2\eta\gamma\, v_{Re}}{B_{Re}^2 - v_{Re}^2}\right)^{1/2}. \tag{3.47}$$

This has exactly the same form as the two-dimensional case when the x-components are replaced by the R-components (Priest *et al*, 2000, equation (5.7)). As in the original Craig *et al* (1995) solution, the current tube width scales as $\eta^{1/2}$. Also, it can be seen that the thickness of the current tube scales relative to the case $\gamma = 1$ by a factor of $\gamma^{1/2}$. Thus the current tube widens as γ increases or as B_{Re} approaches $|v_{Re}|$. The relationship between l and γ for varying (B_{Re}/v_{Re}) is shown in Figure 3.9. The singularity that occurs when $B_{Re}^2 = v_{Re}^2$ is also present in the earlier solutions of Craig *et al* (1995) at $\lambda = 1$. The assumptions of the model include the condition that at $R = 1$ magnetic diffusion is negligible and close to $R = 0$ there is a narrow boundary layer

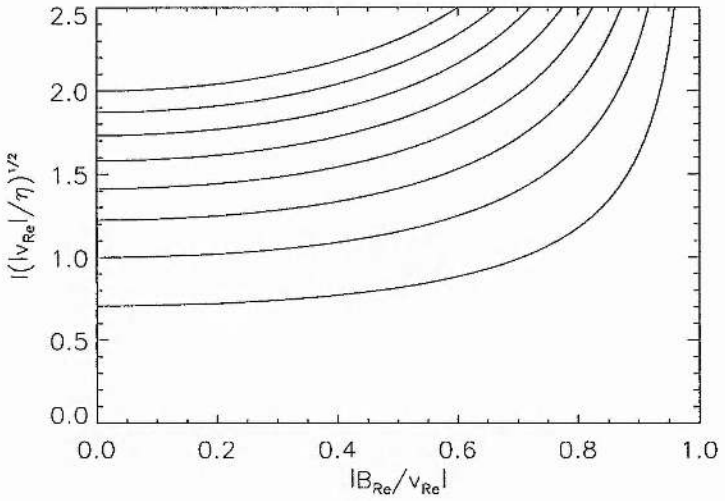

Figure 3.9: The variation of the current tube width (l) with γ and $|B_{Re}/v_{Re}|$. Starting from 0.25 on the bottom curve, γ increases in steps of 0.25 up to a value of 2 on the top curve.

where diffusion is important. However, when λ is close to 1 (so that $\mathbf{v}$ is nearly parallel to $\mathbf{B}$ and the advection of flux decreases) or v_{Re}^2 is close to B_{Re}^2, the width of this boundary layer grows indefinitely and so invalidates the assumptions of the model.

3.6 Summary

Exact solutions to the nonlinear MHD equations are extremely rare, but are of great value since their properties may be examined in a transparent way and they may give insights about the general physical behaviour of a plasma. In the subject of three-dimensional MHD reconnection only two such solutions have been previously discovered, namely, the reconnective fan annihilation regime (Craig *et al*, 1995) and the reconnective spine annihilation regime (Craig & Fabling, 1996). Here we have presented a two-fold generalisation of the basic spine reconnective annihilation solutions to leading order in η, where η ($\ll 1$) is the dimensionless magnetic diffusivity. A much larger family of three-dimensional reconnective annihilation solutions therefore exists than was previously thought.

Chapter 4

Linear Collapse of Spatially Linear, Two-Dimensional Null Points

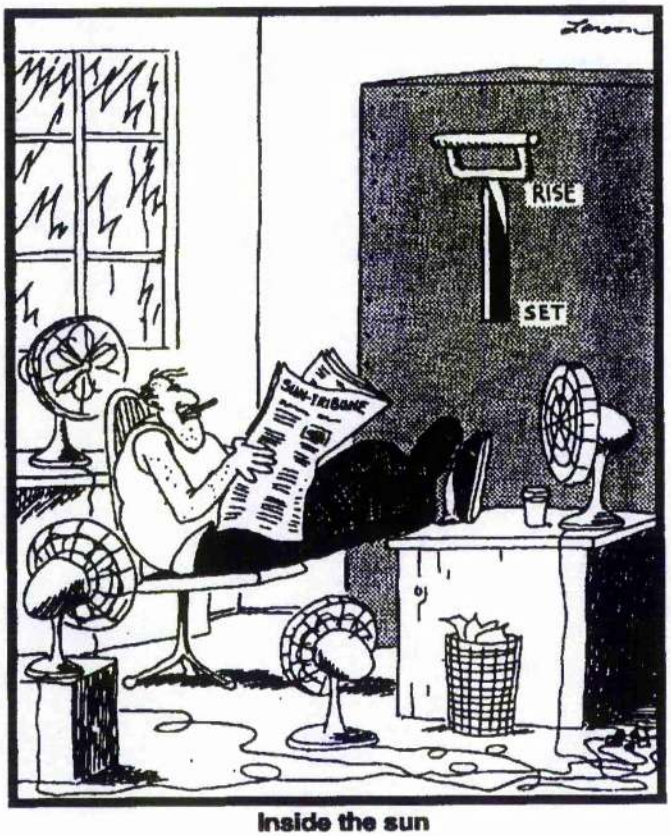

Inside the sun

Mellor, C., Titov, V.S. and Priest, E.R., 2002, Journ. Plasma Phys., **68**, 221.

4.1 Introduction

In this chapter, a technique is developed for analysing the linear collapse properties of spatially linear two-dimensional null points with open boundary conditions. A treatment is given of the collapse of nulls which have current and flow so that they are initially in a steady-state balance between a magnetic force, a pressure force and a centrifugal force. This extends the previous results for initially current-free X-type nulls with no flow. It is found that all X-points, regardless of the current and flow, tend to collapse. Also, O-points collapse in the absence of a plasma flow, but O-points with a large current and possessing a highly super-Alfvénic plasma flow can be stable against linear collapse.

It must again be stressed that in our linear analysis, we talk of collapse when what we are actually seeing is a linear instability. Non-linear effects in principle may act to stop the collapse of the null.

The critical points of a dynamical system are the stationary solutions, and the behaviour of such a system is described by its corresponding phase portrait. The phase portrait near the critical points is described by a linearised system of equations for the dynamical system, and in this chapter we use the linearised MHD equations to find the phase portrait for the collapse equations which then provides useful information about some of the possible types of behaviour of the system. The three-dimensional case is formidable, and so we begin here with the two-dimensional case which has not yet been fully studied.

In Section 2 we introduce and linearise the MHD equations. We then solve the system of linear equations to find a dispersion relation with which we can create a collapse diagram in Section 5. Section 3 deals with X-points and their properties, from potential X-points to general X-points. Section 4 explores O-points and we discover that they too are liable to collapse under this form of perturbation. Section 5 deals with the effect of plasma flow on null points and in Section 6 we offer our conclusions and ideas for further work.

4.2 Linear Analysis

4.2.1 Model Equations

The ideal, time-dependent, incompressible and dimensionless MHD equations are

$$\frac{\partial \mathbf{B}}{\partial t} - \nabla \times (\mathbf{v} \times \mathbf{B}) = \mathbf{0}, \tag{4.1}$$

and

$$\frac{\partial \mathbf{v}}{\partial t} + (\mathbf{v} \cdot \nabla)\mathbf{v} = -\nabla p + (\nabla \times \mathbf{B}) \times \mathbf{B}, \tag{4.2}$$

with the conditions that

$$\nabla \cdot \mathbf{B} = \nabla \cdot \mathbf{v} = 0, \tag{4.3}$$

where the magnetic field ($\mathbf{B}$), pressure (p) and plasma velocity ($\mathbf{v}$) are normalised with respect to a characteristic field (B_*), twice the magnetic pressure (B_*^2/μ_0) and the Alfvén speed ($v_A = B_*/(\mu_0\rho)^{1/2}$), respectively. Time ($t$) is normalised with respect to (l/v_A) in terms of a characteristic length-scale (l).

Equations (4.1)-(4.3) admit a special class of solutions (Klapper *et al*, 1996; Bulanov & Sakai, 1997) of the form

$$\mathbf{B} = \mathcal{B}(t) \cdot \mathbf{r}, \tag{4.4}$$

$$\mathbf{v} = \mathcal{V}(t) \cdot \mathbf{r}, \tag{4.5}$$

$$p = \tfrac{1}{2}\mathbf{r}^T \cdot \mathcal{P}(t) \cdot \mathbf{r} + p_0, \tag{4.6}$$

where $\mathbf{r}$ is the position vector and $\mathcal{B}(t)$, $\mathcal{V}(t)$ and $\mathcal{P}(t)$ are time-dependent matrices with elements $\mathcal{B}_{ij} = \partial B_i/\partial x_j$, $\mathcal{V}_{ij} = \partial v_i/\partial x_j$ and $\mathcal{P}_{ij} = \partial^2 p/\partial x_i \partial x_j$, respectively. The constant p_0 ensures that the pressure is always positive in the region under consideration.

Solutions of this particular form represent flows of plasma in the neighbourhood of a stagnation point located at a null point ($\mathbf{r} = 0$) of the magnetic field. The solutions will also yield the leading terms in a corresponding Taylor expansion of more general MHD solutions. In particular, one can show that it describes an arbitrary ideal MHD flow in the neighbourhood of a magnetic null (Klapper *et al*, 1996; Bulanov & Sakai, 1997).

Substitution of Equations (4.4)-(4.6) into the MHD equations yields the following matrix system of ordinary differential equations:

$$\frac{d\mathcal{B}}{dt} + \mathcal{B}\mathcal{V} - \mathcal{V}\mathcal{B} = 0, \tag{4.7}$$

$$\frac{d\mathcal{V}}{dt} + \mathcal{V}^2 = -\mathcal{P} + \mathcal{B}^2 - \mathcal{B}^T\mathcal{B}, \tag{4.8}$$

$$tr(\mathcal{B}) = tr(\mathcal{V}) = 0. \tag{4.9}$$

The equations of the magnetic field lines and streamlines are given by A = constant and ψ = constant, respectively, where the flux function (A) and stream function (ψ) are related to the

magnetic field and plasma velocity by

$$B_x = \frac{\partial A}{\partial y}, \quad B_y = -\frac{\partial A}{\partial x}, \quad v_x = \frac{\partial \psi}{\partial y}, \quad v_y = -\frac{\partial \psi}{\partial x}.$$

4.2.2 Initial State

The initial state ($\mathcal{B}_0$,$\mathcal{V}_0$,$\mathcal{P}_0$) satisfies the steady-state equations

$$\mathcal{B}_0\mathcal{V}_0 - \mathcal{V}_0\mathcal{B}_0 = 0, \tag{4.10}$$

$$\mathcal{V}_0^2 = -\mathcal{P}_0 + \mathcal{B}_0^2 - \mathcal{B}_0^T\mathcal{B}_0, \tag{4.11}$$

with the conditions

$$tr(\mathcal{B}_0) = tr(\mathcal{V}_0) = 0. \tag{4.12}$$

In particular, we shall start with a magnetic field ($\mathcal{B}_0$) of the form

$$\mathcal{B}_0 = \begin{pmatrix} 0 & (1-J_0)/2 \\ (1+J_0)/2 & 0 \end{pmatrix},$$

where J_0 is the dimensionless current in the z-direction. The corresponding flux function is

$$A_0 = \frac{(1-J_0)y^2 - (1+J_0)x^2}{4}.$$

Thus, if $|J_0| < 1$, then $\mathcal{B}_0$ represents an X-point with hyperbolic field lines, whereas $|J_0| > 1$ gives an O-point with elliptical field lines. The special case $|J_0| = 1$ gives a one-dimensional field with straight field lines.

In order to satisfy the induction equation (4.10), we use the only permissible flow ($\mathcal{V}_0$) which is parallel to the field and so has the form

$$\mathcal{V}_0 = \begin{pmatrix} 0 & M_A(1-J_0)/2 \\ M_A(1+J_0)/2 & 0 \end{pmatrix},$$

where $M_A(= v_0/B_0)$ is the dimensionless Alfvén Mach number.

The pressure matrix that is required to balance the magnetic force is then from Equation (4.11)

$$\mathcal{P}_0 = \frac{1}{4}\begin{pmatrix} (J_0+1)(M_A^2(J_0-1) - 2J_0) & 0 \\ 0 & (J_0-1)(M_A^2(J_0+1) - 2J_0) \end{pmatrix}.$$

4.2.3 Linearised Equations

In this chapter we shall assume that the magnetic field, plasma flow and pressure gradients are made up of the initial, steady component ($\mathcal{B}_0$,$\mathcal{V}_0$,$\mathcal{P}_0$) plus a small, time-dependent perturbation ($\mathcal{B}_1(t)$,$\mathcal{V}_1(t)$,$\mathcal{P}_1(t)$). Linearising Equations (4.7)-(4.9) then reduces them to a matrix system for the perturbed quantities ($\mathcal{B}_1(t)$,$\mathcal{V}_1(t)$,$\mathcal{P}_1(t)$) in terms of the initial state ($\mathcal{B}_0$,$\mathcal{V}_0$,$\mathcal{P}_0$), namely,

$$\frac{d\mathcal{B}_1}{dt} + \mathcal{B}_0\mathcal{V}_1 + \mathcal{B}_1\mathcal{V}_0 - \mathcal{V}_0\mathcal{B}_1 - \mathcal{V}_1\mathcal{B}_0 = 0, \tag{4.13}$$

$$\frac{d\mathcal{V}_1}{dt} + \mathcal{V}_0\mathcal{V}_1 + \mathcal{V}_1\mathcal{V}_0 = -\mathcal{P}_1 + \mathcal{B}_0\mathcal{B}_1 + \mathcal{B}_1\mathcal{B}_0 - \mathcal{B}_0^T\mathcal{B}_1 - \mathcal{B}_1^T\mathcal{B}_0, \tag{4.14}$$

$$tr(\mathcal{B}_1) = tr(\mathcal{V}_1) = 0. \tag{4.15}$$

In order to solve the system of equations, the perturbations ($\mathcal{B}_1$,$\mathcal{V}_1$,$\mathcal{P}_1$) to the initial state are assumed to be of the form

$$\mathcal{B}_1 = \begin{pmatrix} B_{11}(t) & B_{12}(t) \\ B_{21}(t) & -B_{11}(t) \end{pmatrix},$$

$$\mathcal{V}_1 = \begin{pmatrix} V_{11}(t) & V_{12}(t) \\ V_{21}(t) & -V_{11}(t) \end{pmatrix},$$

$$\mathcal{P}_1 = \begin{pmatrix} P_{11}(t) & P_{12}(t) \\ P_{12}(t) & P_{22}(t) \end{pmatrix},$$

for which (4.15) is satisfied and $\mathcal{P}_1$ is symmetric. After substituting these matrices into the linearised equations (4.13)-(4.14), we obtain eight equations for the nine unknowns (B_{11}, B_{12}, B_{21}, V_{11}, V_{12}, V_{21}, P_{11}, P_{12}, P_{22}) of the perturbed system. Only seven of these eight equations are independent, however, since the trace of Equation (4.13) automatically vanishes, which means that the two equations in the leading diagonal of the induction equation (4.13) are automatically equal and opposite in sign. This in turn arises because the divergence of Equation (4.1) is satisfied automatically.

The fact that we have only seven independent equations implies that we are free to choose two of the perturbations ourselves, and the rest can then be written in terms of them. Also, it can be shown from these equations that

$$B_{21}(t) = \frac{J_0 + 1}{J_0 - 1} B_{12}(t),$$

and

$$V_{21}(t) = V_{12}(t),$$

which further reduces the number of unknown variables to seven and the number of independent equations to five. They are

$$\begin{aligned}
(1+J_0)^2 B_{12} + (J_0-1)\frac{dV_{11}}{dt} + M_A(J_0-1)V_{12} + (J_0-1)P_{11} &= 0,\\
-J_0 B_{11} + \frac{dV_{12}}{dt} + P_{12} &= 0,\\
-(J_0-1)B_{12} - \frac{dV_{11}}{dt} + M_A V_{12} + P_{22} &= 0,\\
\frac{dB_{11}}{dt} + M_A(1+J_0)B_{12} - J_0 V_{12} &= 0,\\
-M_A(J_0-1)B_{11} + \frac{dB_{12}}{dt} + (J_0-1)V_{11} &= 0.
\end{aligned} \tag{4.16}$$

The components of the field and flow perturbation matrices can be expressed in terms of the pressure components:

$$B_{11}(t) = -\frac{1}{2J_0M_A}\left(\left[1-\frac{6J_0^2-4J_0}{\xi}\right]\frac{dP_{11}}{dt} + \frac{2}{\xi}\frac{d^3P_{11}}{dt^3}\right) + \frac{1}{J_0}\left(P_{12} + \frac{2}{\xi}\frac{d^2P_{12}}{dt^2}\right)$$

$$-\frac{1}{2J_0M_A}\left(\left[1-\frac{6J_0^2+4J_0}{\xi}\right]\frac{dP_{22}}{dt} + \frac{2}{\xi}\frac{d^3P_{22}}{dt^3}\right),$$

$$B_{12}(t) = \frac{J_0-1}{2J_0}\left(\frac{-3J_0^2+2J_0}{\xi}P_{11} + \frac{1}{\xi}\frac{d^2P_{11}}{dt^2}\right) - \frac{M_A(J_0-1)}{J_0\xi}\frac{dP_{12}}{dt}$$

$$+\frac{J_0-1}{2J_0}\left(\frac{-3J_0^2-2J_0}{\xi}P_{22} + \frac{1}{\xi}\frac{d^2P_{22}}{dt^2}\right),$$

$$V_{11}(t) = -\frac{1}{2J_0}\left(\left[1-\frac{9J_0^2-6J_0}{\xi}\right]\frac{dP_{11}}{dt} + \frac{3}{\xi}\frac{d^3P_{11}}{dt^3}\right) + \frac{M_A}{J_0}\left(P_{12} + \frac{3}{\xi}\frac{d^2P_{12}}{dt^2}\right)$$

$$-\frac{1}{2J_0}\left(\left[1-\frac{9J_0^2+6J_0}{\xi}\right]\frac{dP_{22}}{dt} + \frac{3}{\xi}\frac{d^3P_{22}}{dt^3}\right),$$

$$V_{12}(t) = -\frac{1}{2M_A}\left(\left[1-\frac{6J_0^2-4J_0}{\xi}\right]P_{11} + \frac{2}{\xi}\frac{d^2P_{11}}{dt^2}\right) + \frac{2}{\xi}\frac{dP_{12}}{dt}$$

$$-\frac{1}{2M_A}\left(\left[1-\frac{6J_0^2+4J_0}{\xi}\right]P_{22} + \frac{2}{\xi}\frac{d^2P_{22}}{dt^2}\right),$$

where $\xi \equiv 4J_0^2 + 3M_A^2J_0^2 - 3M_A^2 - 2$.

After eliminating B_{11}, B_{12}, V_{11} and V_{12} from Equations (4.16), we then obtain a single equa-

tion linking the three elements (P_{11}, P_{12}, P_{22}) of the pressure matrix, namely,

$$\begin{aligned}
&\frac{d^4P_{11}}{dt^4} + (2J_0 - 2J_0^2 - 1 - M_A^2 + J_0^2M_A^2)\frac{d^2P_{11}}{dt^2} + \\
&J_0(J_0-1)(J_0^2 - J_0M_A^2 - J_0 - M_A^2)P_{11} \\
&- \quad 2M_A\left(\frac{d^3P_{12}}{dt^3} - (M_A^2+1)(1-J_0^2)\frac{dP_{12}}{dt}\right) \quad + \\
&\frac{d^4P_{22}}{dt^4} + (-2J_0 - 2J_0^2 - 1 - M_A^2 + J_0^2M_A^2)\frac{d^2P_{22}}{dt^2} + \\
&J_0(J_0+1)(J_0^2 - M_A^2 + J_0M_A^2 + J_0)P_{22} = 0. \qquad (4.17)
\end{aligned}$$

Two of the elements of the pressure matrix (say, $P_{12}(t)$ and $P_{22}(t)$) can be considered as being given, so the third ($P_{11}(t)$) is the corresponding solution of this equation. The general solution for $P_{11}(t)$ when $P_{12}(t)$ and $P_{22}(t)$ are given will then be the sum of a particular integral (the driven part) and a complementary function (the normal-mode part), which contains two arbitrary constants and enables two initial conditions to be satisfied. The complementary function may be found by setting $P_{12}(t) = P_{22}(t) = 0$ in Equation (4.17) and so is the solution of

$$\frac{d^4P_{11}}{dt^4} + (2J_0 - 2J_0^2 - 1 - M_A^2 + J_0^2M_A^2)\frac{d^2P_{11}}{dt^2} + J_0(J_0-1)(J_0^2 - J_0M_A^2 - J_0 - M_A^2)P_{11} = 0,$$

A similar reasoning can be developed if $P_{11}(t)$ and $P_{12}(t)$, say, are imposed instead of $P_{12}(t)$ and $P_{22}(t)$. Because the field and flow perturbations can be expressed in terms of the pressure perturbations, then all of the normal-mode responses will be evident in these perturbation components, so if the pressure perturbations grow, then the rest of the perturbations will do so too, and the null will collapse. Equation (4.17) can be re-written to find the normal-mode response when the pressure perturbations have the form, $P_{11}(t) = P_{11}\exp(\lambda t)$, say, such that a non-collapsing solution will have $\Re(\lambda) = 0$. It becomes

$$\begin{aligned}
(\lambda^4 - (2J_0^2 - 2J_0 + 1 + M_A^2 - J_0^2M_A^2)\lambda^2 \quad &+ \quad J_0(J_0-1)(J_0^2 - J_0M_A^2 - J_0 - M_A^2))P_{11} \\
- \quad 2M_A\lambda(\lambda^2 + (M_A^2 \quad &+ \quad 1)(J_0^2 - 1))P_{12} \quad + \\
(\lambda^4 - (2J_0^2 + 2J_0 + 1 + M_A^2 - J_0^2M_A^2)\lambda^2 \quad &+ \quad J_0(J_0+1)(J_0^2 + J_0M_A^2 + J_0 - M_A^2))P_{22} \\
= 0. \qquad (4.18)
\end{aligned}$$

With free boundary conditions, one can in principle choose values of the three free parameters

P_{11}, P_{12} and P_{22} in equation 4.18 such that λ can be of any value. This means that we can choose combinations of the pressure perturbations which will under any initial conditions collapse the null. The addition of boundary conditions will limit our choices of pressure perturbations and give a discrete set of growth rates. We consider next a subsection of the possible combinations by choosing the perturbations to be non-zero only individually for a variety of different initial states, namely, X-points, O-points and nulls with flow.

4.3 X-points

4.3.1 Current-Free X-point

Starting with the simplest situation, namely, a potential X-point with no initial current or plasma flow ($J_0 = M_A = 0$), Equation (4.18) for the normal-mode behaviour of P_{11} reduces to

$$(\lambda^4 - \lambda^2)P_{11} = 0.$$

The solutions in terms of λ are

$$\lambda = -1, 0, 1.$$

$\lambda = 1$ implies that the perturbations grow exponentially, collapsing the null point. Since these normal mode perturbations can occur whatever the form of the driven pressure (P_{12}, P_{22}), the null point is susceptible to this form of collapse. The normal mode values for P_{12} and P_{22} are just the same.

For the driven problem, the element P_{12} decouples from P_{11} in Equation (4.17). In this case (and the case $J_0 \neq 0$) its time-variation does not affect P_{11}.

With $J_0 = M_A = 0$, Equations (4.16) may be solved to give

$$\begin{aligned} B_{11} &= 0, \\ (1-\lambda^2)B_{12} &= P_{11}, \\ (1-\lambda^2)V_{11} &= \lambda P_{11}, \\ \lambda V_{12} &= -P_{12}, \\ P_{22} &= -P_{11}. \end{aligned} \tag{4.19}$$

The pressure perturbation then takes the form

$$p_1 = \frac{P_{11}}{2}(x^2 - y^2) + P_{12}xy,$$

and so on a circle of radius 1, say, where $x = \cos\theta$ and $y = \sin\theta$, it becomes

$$p_1 = \frac{P_{11}\cos(2\theta) + P_{12}\sin(2\theta)}{2}.$$

We can therefore impose odd or even boundary conditions (or a combination of them) on the pressure perturbation along the circle $r = 1$, say. Imposing just the odd condition, by putting $P_{11} = 0$ and $P_{12} \neq 0$, we find from Equations (4.19) that $\lambda^2 = 1$ if $B_{12} \neq 0$, which means that the perturbations can grow exponentially and the X-point collapses with a growth rate $\lambda = 1$. Thus, during the collapse, $B_{11} = P_{22} = P_{11} = 0$, $B_{12} = -B_{21} = V_{11}$, $V_{12} = V_{21} = -P_{12}$ and the direction of the collapse depends on the value of V_{11}: if $V_{11} < 0$ then $B_{12} < 0$ and the inclination of the separatrix $y = x$ in the first quadrant to the x-axis increases in value and vice versa. If we instead impose the even condition, by putting $P_{12} = 0$ and $P_{11} \neq 0$ with $V_{12} \neq 0$, then we find a state of marginal stability ($\lambda = 0$).

Alternatively, we could instead impose boundary conditions on the unit circle, say, on the magnetic field rather than the pressure. The unperturbed flux function is

$$A_0 = (y^2 - x^2)/2 \quad (= \cos(2\theta_0)/2 \quad \text{on the boundary}), \tag{4.20}$$

while the perturbed flux function is

$$A_0 + A_1 = (y^2 - x^2)/2 + B_{12}(x^2 + y^2), \tag{4.21}$$

or, on the boundary ($r = 1$),

$$A_0 + A_1 = \cos(2\theta_1)/2 + B_{12}. \tag{4.22}$$

Now suppose we move a field line (with flux function $A_0 = \cos(2\theta_0)/2$) from an angular position θ_0 on the unit circle to a position $\theta_1 = \theta_0 + \Delta\theta$ (with flux function $A = \cos(2\theta_1)/2 + B_{12}$). In an ideal motion the value of A is conserved and so after linearising we find

$$\Delta\theta = \frac{B_{12}}{\sin(2\theta_0)}. \tag{4.23}$$

In the first quadrant, $\sin(2\theta_0) > 0$ and so, if $B_{12} > 0$, $\Delta\theta$ is positive and the X-point closes up towards the y-axis, whereas if $B_{12} < 0$ it collapses towards the x-axis.

4.3.2 The Symmetric Case

If we constrain $B_{11} = 0$, $V_{12} = 0$, $P_{12} = 0$ and $M_A = 0$, then the perturbations will not rotate the null and will collapse it to either the x or the y- axis. Equations (4.16) then give the relations

$$V_{11} = \frac{1}{4J_0}\left(\frac{dP_{11}}{dt} + \frac{dP_{22}}{dt}\right), \tag{4.24}$$

$$B_{12} = \frac{1 - J_0}{4J_0}\left(P_{11} + P_{22}\right), \tag{4.25}$$

$$\left(\frac{d^2P_{11}}{dt^2} - (J_0 - 1)^2 P_{11}\right) + \left(\frac{d^2P_{22}}{dt^2} - (J_0 + 1)^2 P_{22}\right) = 0. \tag{4.26}$$

This will give pressure growth rates of $\pm(J_0 + 1)$ or $\pm(J_0 - 1)$. This will collapse the null point, as there is always a positive, real value for the growth rate.

4.3.3 X-points with Current but No Flow

Physical Cause of Collapse of an X-point with Current

Next, consider a magnetic field with current of the form

$$B_{0x} = \frac{y}{\alpha_0}, \quad B_{0y} = \alpha_0 x, \tag{4.27}$$

whose field lines are described by

$$\frac{y^2}{\alpha_0} - \alpha_0 x^2 = k, \tag{4.28}$$

and k is a constant. The resulting current is along the z-direction, is uniform and has a value

$$j_0 = \frac{\alpha_0^2 - 1}{\mu_0 \alpha_0}.$$

The Lorentz force due to this field is

$$\mathbf{j_0} \times \mathbf{B_0} = j_0 \begin{pmatrix} -\alpha_0 x \\ y/\alpha_0 \end{pmatrix},$$

which balances the pressure gradient in the equilibrium state. The Ohmic heating due to this current is

$$\frac{(\alpha_0^2 - 1)^2}{\sigma \mu_0^2 \alpha_0^2}. \tag{4.29}$$

Now suppose we perturb the field so its components become

$$B_x = \frac{y}{\alpha}, \quad B_y = \alpha x\,,$$

in place of (4.27) and the same field lines are described by

$$\frac{y^2}{\alpha} - \alpha x^2 = k,$$

in place of (4.28). The resulting current is

$$j = \frac{\alpha^2 - 1}{\mu_0 \alpha},$$

again in the z-direction, so that the Lorentz force due to the new field is

$$\mathbf{j} \times \mathbf{B} = j \begin{pmatrix} -\alpha\, x \\ y/\alpha \end{pmatrix}.$$

The Ohmic heating is now

$$\frac{(\alpha^2 - 1)^2}{\sigma \mu_0^2 \alpha^2}. \tag{4.30}$$

The additional Lorentz force acting on the plasma is

$$\mathbf{F} = \frac{\alpha^2 - \alpha_0^2}{\mu_0} \begin{pmatrix} -x \\ y/\alpha_0^2 \alpha^2 \end{pmatrix}.$$

Figure 4.1 shows an initial X-point (dotted), a perturbed X-point and the additional magnetic force that is acting on the plasma in the perturbed state. This force is in such a direction as to continue the collapse of the X-point. For example, along the x-axis it is directed inwards, towards the null point due to the enhanced magnetic pressure force and along the y-axis it is directed outwards, away from the null point due to the enhanced magnetic tension force. Of course, there are other forces (such as a pressure gradient) that could in principal act against the magnetic force.

From (4.29) and (4.30), we can also see that if α is further away in value from 1 than α_0, so that the X-point collapses, then the heating will increase. If, on the other hand, α is closer in value to 1 than α_0, so that the angle between the separatrices approaches $\pi/2$, the heating will decrease.

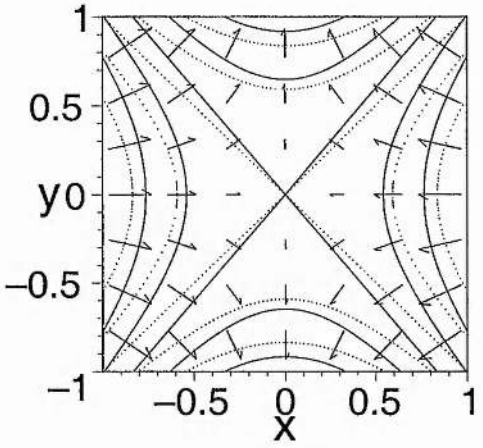

Figure 4.1: A plot of the magnetic field lines of an X-point with the initial state $\alpha_0 = 1$ (dotted curves) and the perturbed state having $\alpha = 1.2$ (solid curves). The arrows show the direction and relative magnitude of the additional force acting on the plasma.

Linear Analysis

Keeping $M_A = 0$, but now allowing J_0 to be non-zero so there can be some initial current in the null point, Equation (4.18) becomes

$$(\lambda^4 - (2J_0^2 - 2J_0 + 1)\lambda^2 + J_0^2(J_0+1)^2)P_{11} \quad + \\ (\lambda^4 - (2J_0^2 \quad + \quad 2J_0 + 1)\lambda^2 + J_0^2(J_0-1)^2)P_{22} = 0.$$

If we set $P_{22} = 0$ and solve for the normal modes (λ) of P_{11}, then we find that the growth rates for P_{11} are $\lambda = \pm J_0, \pm(J_0 - 1)$. Instead, setting $P_{11} = 0$ allows us to calculate the growth rates for the normal modes of P_{22}, which are $\lambda = \pm J_0, \pm(J_0+1)$. All of these represent an exponential growth of the perturbation, and therefore a collapse of the null point but with different growth rates from before. These are shown in Figure 4.2 which implies that for $-1 < J_0 < 1$ there is always a positive, non-zero value of λ, giving exponential growth of the perturbation, regardless of the value of J_0. The effect of increasing the current from zero is to decrease the growth-rate of the stable mode and increase that of the neutral mode.

This analysis applies to all types of null point with no flow, namely, X-points ($|J_0| < 1$), O-points ($|J_0| > 1$) and one-dimensional current sheets ($|J_0| = 1$).

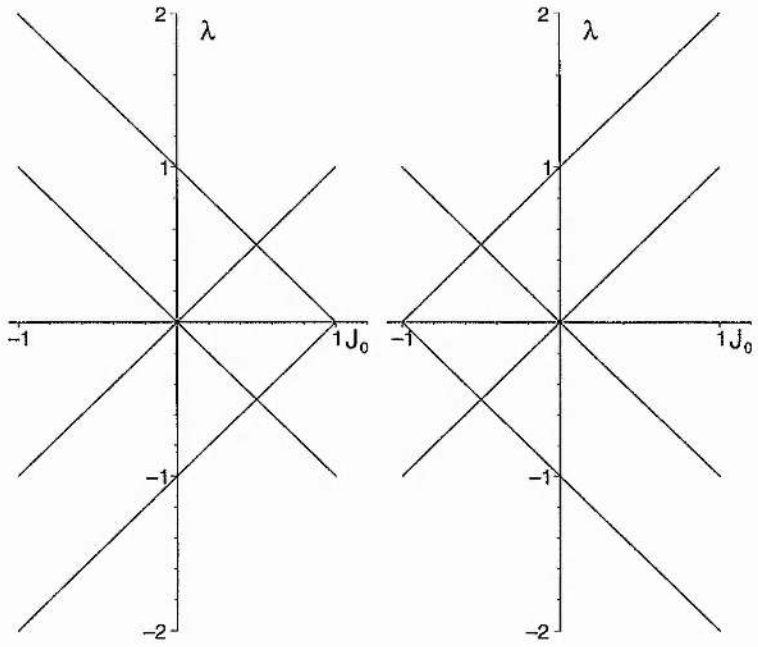

Figure 4.2: The growth rates (λ) of the pressure perturbations P_{11} (*left*) and P_{22} (*right*) as functions of the dimensionless current (J_0).

4.4 O-points

4.4.1 Physical Cause of Collapse

The linear analysis of the previous section suggests that an O-point will tend to collapse (when there is no plasma flow present), which, as far as we are aware, is a new result, so what is the physical cause for this collapse?

Consider a magnetic field (**B**) such that

$$B_{0x} = -\frac{1}{\alpha_0}\, y, \quad B_{0y} = \alpha_0\, x,$$

whose field lines are elliptical and are described by

$$\frac{1}{\alpha_0}\, y^2 + \alpha_0\, x^2 = k,$$

where k is a constant and the area of the ellipse is πk and so is independent of α_0.

The current (j_0) is given by

$$j_0 = \frac{\alpha_0^2 + 1}{\mu_0 \alpha_0},$$

in the z-direction. The Lorentz force is

$$\mathbf{j_0} \times \mathbf{B_0} = j_0 \begin{pmatrix} -\alpha_0 x \\ -y/\alpha_0 \end{pmatrix},$$

which can be balanced by the pressure gradient so that the null point is in equilibrium. The Ohmic heating (j^2/σ) is given by

$$\frac{(\alpha_0^2 + 1)^2}{\sigma \mu_0^2 \alpha_0^2}$$

Now perturb the field such that

$$B_x = -\frac{1}{\alpha} y, \quad B_y = \alpha x,$$

and the same field lines are described by

$$\frac{1}{\alpha} y^2 + \alpha x^2 = k,$$

and have a constant area as α changes. The current (j) is given by

$$j = \frac{\alpha^2 + 1}{\mu_0 \alpha},$$

and the Lorentz force is

$$\mathbf{j} \times \mathbf{B} = j \begin{pmatrix} -\alpha x \\ -y/\alpha \end{pmatrix}.$$

The additional magnetic force acting on the plasma is therefore

$$\mathbf{F} = \frac{\alpha^2 - \alpha_0^2}{\mu_0} \begin{pmatrix} -x \\ y/(\alpha^2 \alpha_0^2) \end{pmatrix},$$

which will tend to carry on flattening the ellipse as can be seen in Figure 4.3. The magnetic tension force ($[\mathbf{B} \cdot \nabla]\mathbf{B}/\mu_0$) is stabilizing and the magnetic pressure force ($\nabla(B^2)/[2\mu_0]$) is destabilizing and dominant, causing the collapse due to magnetic forces. The Ohmic heating (j^2/σ) is now

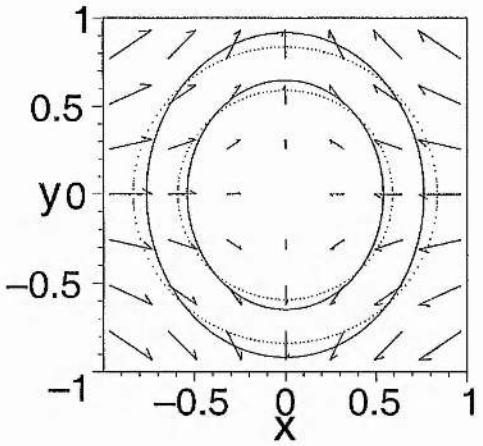

Figure 4.3: A plot of the magnetic field lines of an O-point with $\alpha_0 = 1$ (dotted ellipses) and the perturbed field with $\alpha = 1.2$ (solid ellipses). The arrows indicate the direction and relative strength of the additional force acting on the plasma.

given by

$$\frac{(\alpha^2+1)^2}{\sigma\mu_0^2\alpha^2},$$

from which it can be seen that, if α is further away from 1 in value than α_0, the ellipse is flattened and the heating rises. If, on the other hand, α is closer in value to 1 than α_0, the ellipse becomes more circular and the Ohmic heating reduces. This simple analysis shows that a magnetic null in the form of an O-point tends to collapse into a current sheet under the present approximations due to the magnetic forces. Other forces (again, such as a pressure gradient) could, in principal, stop the collapse.

4.5 Effect of flow

Equation (4.18) can be used to find the normal-mode frequencies of the system by setting two of the elements to zero and requiring that the coefficient of the third be zero. This produces three equations, the solutions of which give us the normal-mode frequencies for P_{11}, P_{12} and P_{22}, respectively,

$$\lambda^4+(-2J_0^2+2J_0-1-M_A^2+J_0^2M_A^2)\lambda^2+J_0(J_0-1)(J_0^2-J_0M_A^2-J_0-M_A^2)=0, \quad (4.31)$$

$$\lambda^2+(M_A^2+1)(J_0^2-1)=0, \quad (4.32)$$

$$\lambda^4+(-2J_0^2-2J_0-1-M_A^2+J_0^2M_A^2)\lambda^2+J_0(J_0+1)(J_0^2+J_0M_A^2+J_0-M_A^2)=0. \quad (4.33)$$

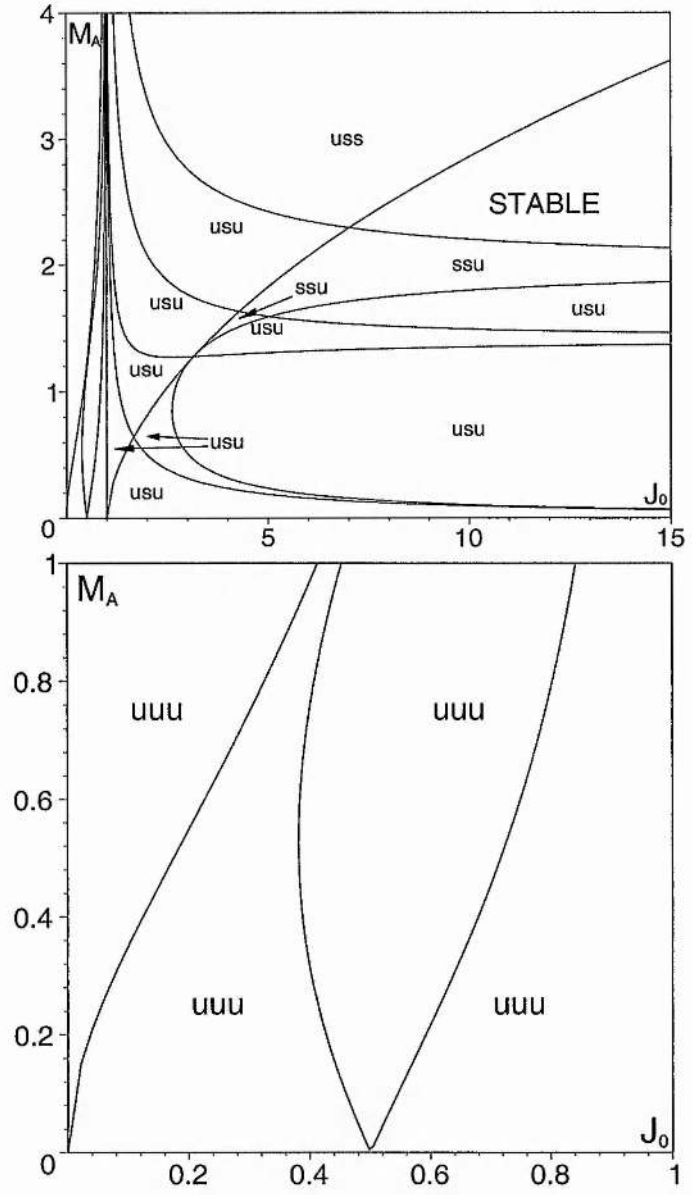

Figure 4.4: Plots of the regions in J_0-M_A parameter space where different perturbations have growing solutions. The sets of three letters indicate the stability to collapse of the pressure elements in that particular region. Thus, for instance, "uss" would indicate that P_{11} in unstable to collapse, whereas P_{12} and P_{22} are both stable to collapse. The top figure shows one completely stable region. The bottom figure shows the region for $0 < J_0 < 1$ and $0 < M_A < 1$, i.e., an X-point.

Figure 4.4 shows the curves in M_A-J_0 parameter space where $\Re(\lambda)$ vanishes for each of the normal modes. The figure also indicates where P_{11}, P_{12} and P_{22} are each unstable (i.e., at least one value of $\Re(\lambda)$ is positive) or stable (i.e., all values of $\Re(\lambda)$ are zero) to collapse. It is constructed in the following way. The polynomials (4.31) and (4.33) both have the form

$$\lambda^4 + A\lambda^2 + B = 0,$$

where A and B are real, and so

$$\lambda^2 = \frac{-A \pm (A^2 - 4B)^{1/2}}{2}$$

If $B < 0$, the discriminant in this solution is positive, giving one positive and one negative solution for λ^2, which means that at least one value of $\Re(\lambda)$ is positive and the corresponding pressure parameter grows exponentially in time. If $A < 0$, the solution for λ^2 will have a positive real part, which means that again at least one of the values of $\Re(\lambda)$ will be positive and the pressure grows. If $A^2 - 4B < 0$, the solution for λ^2 is complex, which implies that at least one of the values of $\Re(\lambda)$ is positive, and again we have a collapsing solution. The condition for perturbations that will not cause the collapse of the null point is that $\Re(\lambda) = 0$, so there is a pure oscillation (i.e., $\lambda^2 < 0$) which therefore occurs when all of A, B and $A^2 - 4B$ are positive. In Figure 4.4, therefore, we have drawn the curves $A = 0$, $B = 0$ and $A^2 - 4B = 0$ for Equations (4.31) and (4.33), which provide the corresponding crossover locations between regions of collapsing and non-collapsing solutions for P_{11} and P_{22}. Furthermore, Equation (4.32) for P_{12} has the form

$$\lambda^2 + C = 0,$$

where C is real. In Figure 4.4 we have therefore also plotted the curve $C = 0$ which gives the crossover points between collapsing and non-collapsing solutions for P_{12}.

There is only one completely stable region, where all of $A, B, C, A^2 - 4B$ are positive and all the values of λ are purely imaginary so that P_{11}, P_{12} and P_{22} are all purely oscillatory. It is located in the upper right part of the top diagram in Figure 4.4. The other regions have at least one of the pressure perturbations growing exponentially and so collapsing the null point provided that the boundary conditions are free. Since the stable region is in the area where $J_0 > 7$ and $M_A > 2$, we can see that all X-points ($|J_0| < 1$) and O-points with weak current ($1 < J_0 < 7$) are unstable to collapse. For most physically realistic flows (i.e., $M_A < 1$ with sub-Alfvénic plasma velocities) the null point will tend to collapse as a result of these perturbations. It is only O-points with strongly super-Alfvénic flows that can be stable against collapse.

Choosing a value from the stability region, namely $[J_0 = 15, M_A = 3]$, substituting these values into the equations for the normal mode solution of P_{11} (4.31) and setting $P_{11} = P_{22} = 0$, we

can show that the extra forces due to the pressure ($-\mathcal{P}_1$), the magnetic pressure ($-\mathcal{B}_0^T\mathcal{B}_1 - \mathcal{B}_1^T\mathcal{B}_0$), the magnetic tension ($\mathcal{B}_0\mathcal{B}_1 + \mathcal{B}_1\mathcal{B}_0$) and the plasma velocity ($-\mathcal{V}_0\mathcal{V}_1 - \mathcal{V}_1\mathcal{V}_0$) are stabilizing when taken together.

Using the above values for J_0 and M_A, we can obtain as a particular example the following expressions for the pressure perturbations.

$$P_{11} = 2\sin(39.8\,t) + 2\sin(2.96\,t),$$

$$P_{12} = P_{22} = 0.$$

Focussing on the x-component of the forces at the point (1,0), and looking at a small time $t = 10^{-8}$, such that we catch the very initial effect of the perturbations, we find that the pressure force is -8.56×10^{-7}, the magnetic pressure force is $+2.23 \times 10^{-6}$, the magnetic tension force is negligible at $+2 \times 10^{-16}$ and the centrifugal force is $+1.66 \times 10^{-7}$. The magnetic pressure dominates, and the total is $+1.54 \times 10^{-6}$. This is acting outwards, away from the centre of the elliptical field line. The x-component of the velocity perturbation at this point is -0.238 - in towards the centre of the field line. The force is acting against the perturbed velocity which indicates that it tends to stabilize the plasma flow.

The only force acting to destabilize the plasma flow is the pressure force. The other forces at this point are all acting so as to support the flow of plasma and keep the O-point from collapse.

4.6 Summary

In this chapter, we have developed an elegant method to analyse the linear collapse of a linear null point to spatially linear perturbations. We have discovered that all X-type null points including those with steady initial flows and current have a tendancy to collapse. An O-point without flow will also collapse, but an O-point with strong enough flow can be stable.

In the next chapter we aim to develop the ideas further by considering the much more complex structure of MHD collapse near three-dimensional null points.

Chapter 5

Collapse of Spatially Linear, Three-Dimensional Null Points

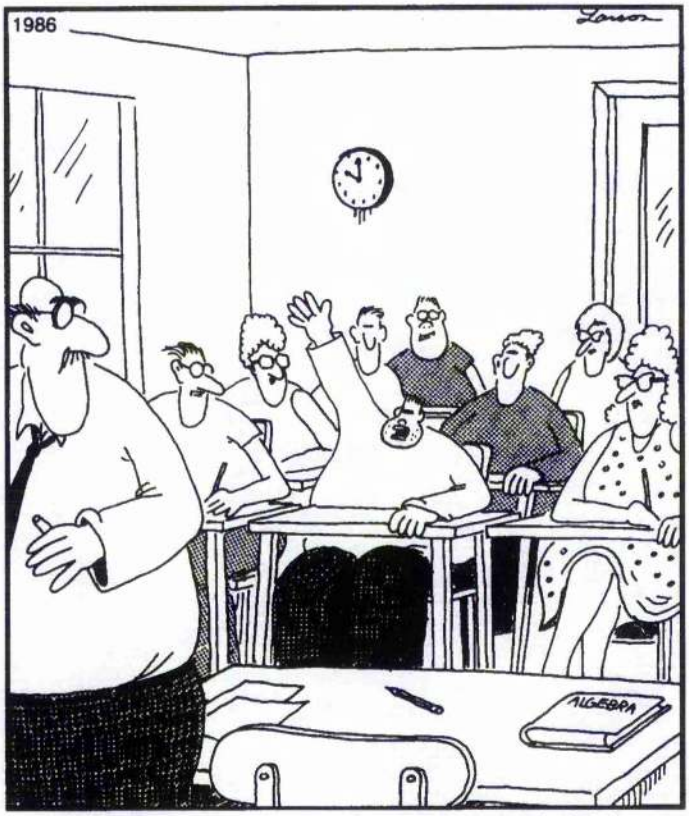

"Mr. Osborne, may I be excused? My brain is full."

Mellor, C., Titov, V.S. and Priest, E.R., 2003, Geophys. Astrophys. Fluid Dyn., in press.

5.1 Introduction

The collapse of the magnetic field in the vicinity of a null point creates a large electrical current. Non-ideal effects in the surrounding plasma can then allow the onset of magnetic reconnection, which is important in many astrophysical phenomena. An elegant technique is used to show that spatially linear, initially potential, three-dimensional null points have a tendency to collapse with a growth of either the spine current or the fan current or a combination of both. The rate of collapse is determined for an incompressible plasma flow with open boundary conditions. An initial plasma flow affects the rate of collapse by speeding it up.

In Section 2, the ideal MHD equations are introduced and linearised and the model for determining collapse properties is explained. In Section 3 we give a simple physical argument as to how magnetic forces can collapse a potential null point. Section 4 applies the model to potential nulls with all possible initial plasma flows. In Section 5 we offer our conclusions and ideas for future work.

Once again we stress that in our linear analysis we talk of collapse when what we are actually seeing is a linear instability. Non-linear effects in principle may act to stop the collapse of the null.

5.2 MHD and Model Equations

The MHD equations and the model that we use are outlined in the previous chapter (section 4.1.1)

5.2.1 Initial State

The initial state $(\mathcal{B}_0,\mathcal{V}_0,\mathcal{P}_0)$ satisfies the steady-state equations

$$\mathcal{B}_0\mathcal{V}_0 - \mathcal{V}_0\mathcal{B}_0 = 0, \tag{5.1}$$

$$\mathcal{V}_0^2 = -\mathcal{P}_0 + \mathcal{B}_0^2 - \mathcal{B}_0^T\mathcal{B}_0, \tag{5.2}$$

with the conditions

$$tr(\mathcal{B}_0) = tr(\mathcal{V}_0) = 0. \tag{5.3}$$

In particular, we shall start with a magnetic field ($\mathcal{B}_0$) of the form

$$\mathcal{B}_0 = \begin{pmatrix} 1 & (Q - J_\parallel)/2 & 0 \\ (Q + J_\parallel)/2 & R & 0 \\ 0 & J_\perp & -(1+R) \end{pmatrix},$$

where R and Q are symmetric, potential parameters, $J_\parallel$ is the current parallel to the spine of the null (the z-axis) and $J_\perp$ is the current perpendicular to the spine, chosen to lie in the x-direction. Parnell *et al* (1996) and Parnell *et al* (1997) showed that an arbitrary linear null can be reduced to this form and gave a preliminary treatment of its collapse. The form of the initial plasma flow ($\mathcal{V}_0$) is explained in Section 4. For a fuller treatment of initial plasma flows supporting a general null point, see Titov and Hornig (2000).

5.2.2 Linearised Equations

In this chapter we shall assume that the magnetic field, plasma flow and pressure gradients are made up of the initial, steady component ($\mathcal{B}_0$,$\mathcal{V}_0$,$\mathcal{P}_0$) of a potential null plus a small, time-dependent perturbation ($\mathcal{B}_1(t)$,$\mathcal{V}_1(t)$,$\mathcal{P}_1(t)$). Linearising Equations (5.1)-(5.3) then reduces them to a matrix system for the perturbed quantities ($\mathcal{B}_1(t)$,$\mathcal{V}_1(t)$,$\mathcal{P}_1(t)$) in terms of the initial state ($\mathcal{B}_0$,$\mathcal{V}_0$,$\mathcal{P}_0$), namely,

$$\frac{d\mathcal{B}_1}{dt} + \mathcal{B}_0\mathcal{V}_1 + \mathcal{B}_1\mathcal{V}_0 - \mathcal{V}_0\mathcal{B}_1 - \mathcal{V}_1\mathcal{B}_0 = 0, \tag{5.4}$$

$$\frac{d\mathcal{V}_1}{dt} + \mathcal{V}_0\mathcal{V}_1 + \mathcal{V}_1\mathcal{V}_0 = -\mathcal{P}_1 + \mathcal{B}_0\mathcal{B}_1 + \mathcal{B}_1\mathcal{B}_0 - \mathcal{B}_0^T\mathcal{B}_1 - \mathcal{B}_1^T\mathcal{B}_0, \tag{5.5}$$

$$tr(\mathcal{B}_1) = tr(\mathcal{V}_1) = 0. \tag{5.6}$$

In order to solve the system of equations, the perturbations ($\mathcal{B}_1$,$\mathcal{V}_1$,$\mathcal{P}_1$) to the initial state are assumed to be of the form

$$\mathcal{B}_1 = \begin{pmatrix} B_{11}(t) & B_{12}(t) & B_{13}(t) \\ B_{21}(t) & B_{22}(t) & B_{23}(t) \\ B_{31}(t) & B_{32}(t) & -B_{11}(t) - B_{22}(t) \end{pmatrix},$$

$$\mathcal{V}_1 = \begin{pmatrix} V_{11}(t) & V_{12}(t) & V_{13}(t) \\ V_{21}(t) & V_{22}(t) & V_{23}(t) \\ V_{31}(t) & V_{32}(t) & -V_{11}(t) - V_{22}(t) \end{pmatrix},$$

$$\mathcal{P}_1 = \begin{pmatrix} P_{11}(t) & P_{12}(t) & P_{13}(t) \\ P_{12}(t) & P_{22}(t) & P_{23}(t) \\ P_{13}(t) & P_{23}(t) & P_{33}(t) \end{pmatrix},$$

for which (5.6) is satisfied identically and $\mathcal{P}_1$ is symmetric.

In this chapter we shall derive the collapse behaviour of the initially potential case. In the case of the potential null, Equations (5.4)-(5.5) yield seventeen independent equations for twenty-two variables. We choose to find the field and flow components and one pressure component in terms of the other five pressure components.

The solutions are made up of two parts, namely, a driven part (when the five imposed pressure functions are non-zero and can be chosen in principle to model given perturbations to five functions of the field, flow or pressure) and a normal-mode part. These are equivalent, respectively, to the particular integral and complementary function solutions of a differential equation. As we want to find the collapse properties of the null in the general case, we will concentrate on the normal-mode solutions to these equations. Such normal mode solutions will be present whatever the imposed pressure perturbations. In turn, the imposed pressures contain the reaction of the surrounding fluid to the collapsing null point as well as the effects of whatever at large distances has driven or initiated the collapse. Depending on the nature of those pressures, their effect may or may not dominate at large times. In order to study the normal-mode solutions, we substitute

$$\begin{aligned} B_{ij}(t) &= B_{ij}\exp(\lambda t), \\ V_{ij}(t) &= V_{ij}\exp(\lambda t), \\ P_{ij}(t) &= P_{ij}\exp(\lambda t), \end{aligned}$$

for each of the perturbation components, which yields seventeen equations involving λ instead of time derivatives.

5.3 A Simple Physical Argument

The following simple arguments are intended to demonstrate why a perturbed potential magnetic null can collapse solely due to magnetic forces. We do not include other forces such as a pressure gradient or centrifugal force, which may in principle prevent such a collapse.

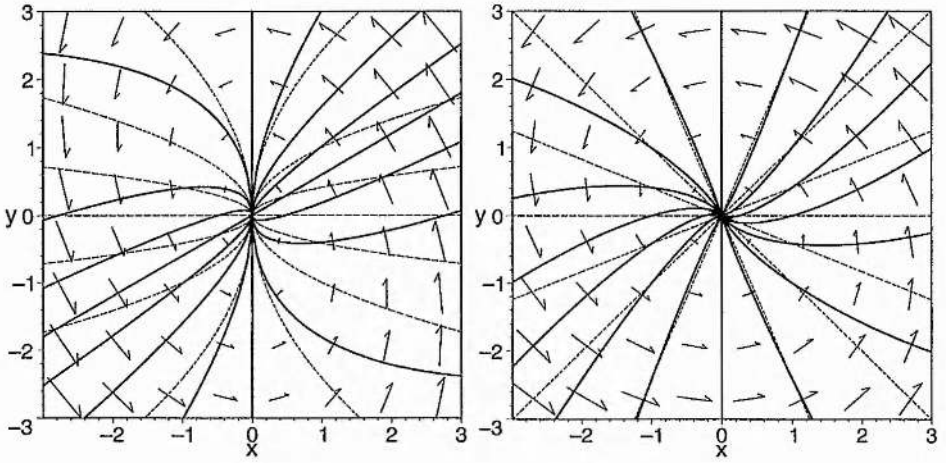

Figure 5.1: Introducing a Spine Current. (*Left*) The collapse of the null in the xy plane in the case $R = 0.5$. (*Right*) The collapse of the null in the xy plane in the case $R = 1$. The thin, dotted lines are the unperturbed fieldlines, whereas the thick, solid lines are the perturbed fieldlines ($\epsilon = 0.3$) and the arrows show the relative strength and direction of the induced Lorentz force which is seen to increase the perturbation and so collapse the null.

5.3.1 Collapse with a Spine Current

Taking the simple potential field (**B**) described by

$$B_x = x, \quad B_y = y, \quad B_z = -2z, \tag{5.7}$$

which has field lines described in the xy-plane by $y = mx$, and perturbing it such that

$$B_x = x, \quad B_y = \epsilon x + y, \quad B_z = -2z, \tag{5.8}$$

so that a current of strength ϵ is introduced in the z-direction, the Lorentz force (**F**) introduced by the perturbation is,

$$F_x = -\epsilon^2 x - \epsilon y, \quad F_y = \epsilon x, \quad F_z = 0. \tag{5.9}$$

The field lines in the xy-plane are now given by $y = \epsilon x \ln(x) + mx$. Plotting the original field lines and the perturbed field lines demonstrates how the perturbation has affected the structure of the field. Figure 5.1 shows this and also the relative direction and magnitude of the Lorentz force caused by the perturbation. It can be seen that the force is such as to reinforce the perturbation and therefore continue the collapse of the structure of the field lines.

For a more general potential null, where the initial magnetic field (**B***) is given by

$$B_x^* = x, \quad B_y^* = Ry, \quad B_z^* = -(1+R)z, \tag{5.10}$$

and fieldlines in the xy-plane by $y = Cx^R$, perturbing the field as above such that the components are

$$B_x^* = x, \quad B_y^* = \epsilon x + Ry, \quad B_z^* = -(1+R)z, \tag{5.11}$$

means that the fieldlines are now described by the equation $y = Cx^R + \epsilon x/(1-R)$ and the Lorentz force ($\mathbf{F}^*$) is

$$F_x^* = -\epsilon^2 x - \epsilon R y, \quad F_y^* = \epsilon x, \quad F_z^* = 0. \tag{5.12}$$

When $R < 1$, this force acts to continue the perturbation, collapsing the null point but when $R > 1$, the force acts against the perturbation, preventing the null from collapse. If the z-current is introduced by perturbing the x-component of the field instead, the opposite occurs. $R > 1$ will collapse this time and $R < 1$ will not. This suggests that the null will collapse in the xy-plane when the magnetic field perturbation is parallel to the direction of the unperturbed fieldlines at the origin.

When introducing current by perturbing the y-component of the field, the magnetic tension force ($[\mathbf{B}^* \cdot \nabla]\mathbf{B}^*$) acts to increase the perturbation in the second and fourth quadrants, and acts against the perturbation in the first and third. The magnetic pressure force ($-\nabla(\mathbf{B}^{*2})/2$) acts to decrease the perturbation in quadrants two and four, and to increase the perturbation in one and three. The forces leading to collapse are dominant when their sum is taken to give the Lorentz force ($\mathbf{F}^*$).

5.3.2 Collapse with a Fan Current

Perturbing $\mathbf{B}$ (with fieldlines in the yz-plane described by $z = C/y^2$) so that now

$$B_x = x, \quad B_y = y, \quad B_z = \epsilon y - 2z, \tag{5.13}$$

and current is instead introduced in the x-direction, the Lorentz force is this time

$$F_x = 0, \quad F_y = -\epsilon^2 y + 2\epsilon z, \quad F_z = \epsilon y. \tag{5.14}$$

The field lines are described by $z = \epsilon y/3 + C/y^2$. Figure 5.2 shows this situation. The lines are as described in Fig 5.1 and one can see that the Lorentz force is again such as to continue the collapse of the field line structure.

Now, taking the general potential field ($\mathbf{B}^*$) described by

$$B_x^* = x, \quad B_y^* = Ry, \quad B_z^* = -(1+R)z, \tag{5.15}$$

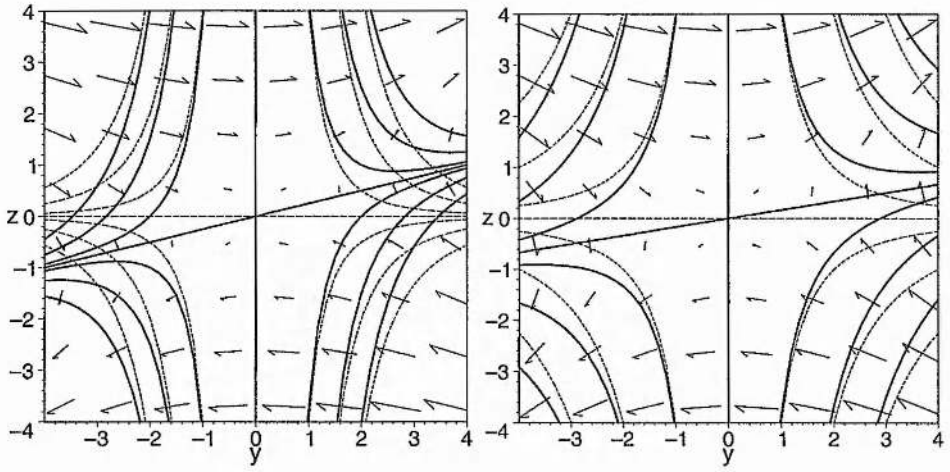

Figure 5.2: Introducing a Fan Current. (*Left*) The collapse of the null in the yz-plane in the case $R = 0.5$. (*Right*) The collapse of the null in the yz-plane in the case $R = 1$. The lines and arrows are as in Fig 1 and $\epsilon = 0.5$. For all values of R, the Lorentz force is in a direction such as to increase the perturbation and collapse the null.

which has field lines described in the yz-plane by $z = C/y^{(1+R)/R}$, and perturbing it such that

$$B_x^* = x, \quad B_y^* = Ry, \quad B_z^* = \epsilon y - (1+R)z, \tag{5.16}$$

so that a current of strength ϵ is introduced in the x-direction, the Lorentz force ($\mathbf{F}^*$) introduced by the perturbation is found to be

$$F_x^* = 0, \quad F_y^* = -\epsilon^2 y + \epsilon(1+R)z, \quad F_z^* = \epsilon R y. \tag{5.17}$$

The field lines in the xz-plane are now given by $z = \epsilon y/(1+2R) + C/y^{(1+R)/R}$. Plotting the original field lines and the perturbed field lines shows how the perturbation has affected the structure of the field. Figure 5.2 illustrates this and also the relative direction and magnitude of the Lorentz force caused by the perturbation. It can be seen that this time for all values of R, the force is such as to reinforce the perturbation and continue the collapse of the structure of the field lines.

5.4 Linear Analysis

5.4.1 $R \neq 1$: the General Case

Setting $Q = J_{\parallel} = J_{\perp} = 0$ in the magnetic field matrix ($\mathcal{B}_0$), the initial plasma flow can be represented by the diagonal matrix,

$$\mathcal{V}_0 = u \begin{pmatrix} 1 & 0 & 0 \\ 0 & U & 0 \\ 0 & 0 & -(1+U) \end{pmatrix},$$

where U determines the shape of the plasma flow and u gives its strength. This is different from (and less restrictive than) substituting $Q = J_{\parallel} = J_{\perp} = 0$ in the results of Titov and Hornig (2000), whose expressions assume current in the null and miss this form of flow. The initial plasma flow is now only field-aligned when $R = U$ which is a new result, additional to those of Titov and Hornig (2000). The perturbed field ($\mathcal{B}_1$), flow ($\mathcal{V}_1$) and current (**J**) components, in terms of the perturbed pressure components are then

$$\begin{aligned}
B_{11} &= 0, \\
\alpha(\lambda + u(1+U))B_{12} &= -(R-1)(\lambda^2 + 2u\lambda - u^2(U^2-1) + R^2 - 1)P_{12}, \\
\beta(\lambda - uU)B_{13} &= (R+2)(\lambda^2 + 2u\lambda - u^2U(U+2) + R(R+2))P_{13}, \\
\alpha(\lambda + u(1+U))B_{21} &= (R-1)(\lambda^2 + 2uU\lambda + u^2(U^2-1) - R^2 + 1)P_{12}, \\
B_{22} &= 0, \\
\gamma(\lambda - u)B_{23} &= (2R+1)(\lambda^2 + 2uU\lambda - u^2(2U+1) + 2R + 1)P_{23}, \\
-\beta(\lambda - uU)B_{31} &= (R+2)(\lambda^2 - 2u(U+1)\lambda + u^2U(U+2) - R(R+2))P_{13}, \\
-\gamma(\lambda - u)B_{32} &= (2R+1)(\lambda^2 - 2u(U+1)\lambda + u^2(2U+1) - 2R - 1)P_{23}, \\
(\lambda + 2u)V_{11} &= -P_{11}, \\
\alpha(\lambda + u(1+U))V_{12} &= -(\lambda + u(U-1))(\lambda^2 + 2u\lambda - u^2(U^2-1) + R^2 - 1)P_{12}, \\
-\beta(\lambda - uU)V_{13} &= (\lambda - u(U+2))(\lambda^2 + 2u\lambda - u^2U(U+2) + R(R+2))P_{13}, \\
\alpha(\lambda + u(1+U))V_{21} &= -(\lambda + u(1-U))(\lambda^2 + 2uU\lambda + u^2(U^2-1) - R^2 + 1)P_{12}, \\
(\lambda + 2uU)V_{22} &= -P_{22}, \\
-\gamma(\lambda - u)V_{23} &= (\lambda - u(2U+1))(\lambda^2 + 2uU\lambda - u^2(2U+1) + 2R + 1)P_{23}, \\
-\beta(\lambda - uU)V_{31} &= (\lambda + u(U+2))(\lambda^2 - 2u(U+1)\lambda + u^2U(U+2) - R(R+2))P_{13}, \\
-\gamma(\lambda - u)V_{32} &= (\lambda + u(2U+1))(\lambda^2 - 2u(U+1)\lambda + u^2(2U+1) - 2R - 1)P_{23}, \\
\alpha J_z &= 2(R-1)\lambda P_{12},
\end{aligned}$$

$$\begin{aligned}\beta J_y &= 2(R+2)\lambda P_{13},\\ \gamma J_x &= -2(2R+1)\lambda P_{23},\end{aligned} \tag{5.18}$$

where

$$\begin{aligned}\alpha &= \lambda^3 + u(U+1)\lambda^2 - (u^2(U-1)^2 + (R-1)^2)\lambda - u(U-1)(u^2(U^2-1) - R^2 + 1),\\ \beta &= \lambda^3 - uU\lambda^2 - (u^2(U+2)^2 + (R+2)^2)\lambda + u(U+2)(u^2U(U+2) - R(R+2)),\\ \gamma &= \lambda^3 - u\lambda^2 - (u^2(2U+1)^2 + (2R+1)^2)\lambda + u(2U+1)(u^2(2U+1) - 2R - 1),\end{aligned}$$

and the components P_{11}, P_{22} and P_{33} are related by

$$\begin{aligned}(\lambda - 2u(U+1))(\lambda + 2uU)P_{11} + (\lambda - 2u(U+1))(\lambda + 2u)P_{22}\\ +(\lambda + 2uU)(\lambda + 2u)P_{33} = 0.\end{aligned} \tag{5.19}$$

In order to find the normal-mode response, we set five of the six pressure components (P_{12}, P_{13}, P_{23} and two of P_{11}, P_{22}, P_{33}) to zero. Avoiding the trivial solutions where the field and flow components are also zero, we conclude from the components dependent on P_{12}, P_{13} and P_{23} that the growth rates, λ, are found by setting $\alpha = 0$, $\beta = 0$ and $\gamma = 0$. We ignore the solutions $\lambda = u$, $\lambda = U$ and $\lambda = -u(1+U)$ in Equation (5.18) because they do not cause the current (**J**) to grow as the null becomes perturbed, which is the purpose of studying the collapse of the null in the first place.

If we let α, β, γ have roots $\lambda_{1,j}$, $\lambda_{2,j}$, $\lambda_{3,j}$ ($j = 1, 2, 3$), respectively, then the sums of these roots are

$$\begin{aligned}\sum_{j=1}^{3}\lambda_{1,j} &= -u(U+1),\\ \sum_{j=1}^{3}\lambda_{2,j} &= uU,\\ \sum_{j=1}^{3}\lambda_{3,j} &= u,\end{aligned}$$

implying that if we add all of the nine roots, we have

$$\sum_{i=1}^{i=3}\sum_{j=1}^{j=3}\lambda_{i,j} = 0.$$

This is an important result, as it tells us that there must be both positive and negative values of λ for all values of u, U and R. This implies that there are always at least two perturbations of both

magnetic field and plasma flow that grow exponentially and collapse the null point.

If we expand the nine roots of α, β and γ, in terms of large values of u, representing a strong flow, we find that all nine have the form

$$\lambda = f(U)u + g(R,U)\frac{1}{u} + \mathrm{O}(1/u^3).$$

Thus, the growth rates increase approximately linearly with the strength of the initial plasma flow.

From the remaining pressure components (P_{11}, P_{22} and P_{33}) we conclude from Equation (5.19) that $\lambda = 2u(U+1)$, $\lambda = -2uU$, or $\lambda = -2u$, the three of which sum to zero, so we can conclude once again that there is at least one value of λ that is positive, unless $u = 0$ which is the trivial case of no initial flow. In the particular case of $u = 0$, we can plainly see from α, β and γ that $\lambda = |R-1|$, $\lambda = R+2$ and $\lambda = 2R+1$, respectively, and the zero growth rates from P_{11}, P_{22} and P_{33} are unimportant to the collapse of the null. The growth rates above for the case $u = 0$ agree with those found by Parnell *et al* (1997).

5.4.2 $R = 1$: the Axisymmetric Case

In the axisymmetric case $R = 1$, the initial plasma flow differs from the previous case by including non-diagonal terms which leaves two more cases to study, namely

$$\mathcal{V}_0 = w \begin{pmatrix} 1 & W & 0 \\ W & \Omega & 0 \\ 0 & 0 & -(1+\Omega) \end{pmatrix}, \tag{5.20}$$

and

$$\mathcal{V}_0 = \begin{pmatrix} v & \omega_0 & 0 \\ \nu_0 & -v & 0 \\ 0 & 0 & 0 \end{pmatrix}. \tag{5.21}$$

Because we are dealing with the axisymmetric case, we can rotate the x and y axes as we see fit and as such, we can simplify the initial plasma flow matrices. In particular, it is possible to transform Equation (5.20) to

$$\mathcal{V}_0 = w_1 \begin{pmatrix} 1 & 0 & 0 \\ 0 & \Omega_1 & 0 \\ 0 & 0 & -(1+\Omega_1) \end{pmatrix}, \tag{5.22}$$

and Equation (5.21) becomes

$$\mathcal{V}_0 = \begin{pmatrix} 0 & \omega & 0 \\ \nu & 0 & 0 \\ 0 & 0 & 0 \end{pmatrix}. \tag{5.23}$$

As can be plainly seen, Equation (5.22) is of the same form as was used in the previous section, with w_1 and Ω_1 in place of u and U, respectively, and so for this case we can use the previous analysis substituting $R = 1$.

Finally, we can use Equation (5.23) as an initial condition in the same way as for the general-R case, and the resulting growth rates are as follows. For the components dependent on the pressure components P_{11}, P_{12}, P_{22} and P_{33}, namely B_{11}, B_{12}, B_{21}, B_{22}, V_{11}, V_{12}, V_{21}, V_{22} and J_z, the components are related by

$$\lambda^2 P_{11} - 2(\nu + \omega)\lambda P_{12} + \lambda^2 P_{22} + (\lambda^2 - 4\omega\nu)P_{33} = 0.$$

These components grow with a rate $\lambda = 2(\omega\nu)^{1/2}$, which is positive and real when ω and ν have the same sign, representing a two-dimensional hyperbolic stagnation point flow. When they have opposite signs, representing an elliptical flow, this growth rate is imaginary, so these components do not grow, but oscillate around their initial values. The components dependent on the pressure components P_{13} and P_{23}, namely B_{13}, B_{23}, B_{31}, B_{32}, V_{13}, V_{23}, V_{31}, V_{32}, J_x and J_y, grow with rates λ which satisfy

$$\lambda^6 - 3(\nu\omega + 6)\lambda^4 + 3(\nu^2\omega^2 + 8\nu\omega + 27)\lambda^2 - \nu\omega(\nu\omega + 3)^2 = 0. \tag{5.24}$$

Setting $\xi = \lambda^2 - (\nu\omega + 6)$, the equation becomes

$$\xi^3 - 3(4\nu\omega + 9)\xi + 54 = 0. \tag{5.25}$$

The discriminant (D) of the equation $\xi^3 + \phi\xi + \chi = 0$ is $D \equiv -(4\phi^3 + 27\chi^2)$, which in this case becomes

$$D = 432\nu\omega\left(\left[4\nu\omega + \frac{27}{2}\right]^2 + \frac{243}{4}\right).$$

(i) The case $\nu\omega > 0$

As can be seen, if ν and ω are of the same sign, the discriminant is positive, meaning that the three roots, ξ (and therefore λ^2) are real. If we let $0 < \nu\omega \ll 1$, then expanding the three roots of

Equation (5.24), we find

$$\begin{aligned}\lambda^2 &= 9 + 2\sqrt{\nu\omega} + \frac{13\nu\omega}{9} + \mathrm{O}((\nu\omega)^{3/2}),\\ \lambda^2 &= 9 - 2\sqrt{\nu\omega} + \frac{13\nu\omega}{9} + \mathrm{O}((\nu\omega)^{3/2}),\\ \lambda^2 &= \frac{\nu\omega}{9} + 0.0439(\nu\omega)^2 + \mathrm{O}((\nu\omega)^{5/2}),\end{aligned}$$

all of which are positive, implying that for $0 < \nu\omega \ll 1$, λ is real and positive and the null is susceptible to collapse.

If instead, $\nu\omega \gg 1$, then expanding the three roots of Equation (5.24) gives

$$\begin{aligned}\lambda^2 &= \nu\omega + \sqrt{12\nu\omega} + 6 + \sqrt{\frac{243}{16\nu\omega}} + \mathrm{O}((\nu\omega)^{-1}),\\ \lambda^2 &= \nu\omega - \sqrt{12\nu\omega} + 6 - \sqrt{\frac{243}{16\nu\omega}} + \mathrm{O}((\nu\omega)^{-1}),\\ \lambda^2 &= \nu\omega + 6 + \frac{9}{2\nu\omega} + \mathrm{O}((\nu\omega)^{-2}),\end{aligned}$$

which, again, are all positive, so λ is real and positive, leaving the null again liable to collapse.

Finally, when $\nu\omega = 1$, Equation (5.24) becomes $\lambda^6 - 21\lambda^4 + 108\lambda^2 - 16 = 0$, whose roots are $\lambda = 0.1526$, 8.4653 and 12.3821 to four decimal places. These are once again positive, giving real and positive values for λ.

Figure 5.3 shows a plot of λ^2 as a function of $\nu\omega$ for values of $0 \leq \nu\omega < 5$, bridging the gap between the very small and the large limits discussed above. This shows that for positive values of $\nu\omega$, the three roots of Equation (5.24) are positive, so that the null is unstable against collapse.

From this analysis, we can see that $\lambda^2 > 0$ as well as being real when $\nu\omega > 0$. This means that if the initial flow is hyperbolic and parallel to the xy-plane, the null can collapse.

(ii) The case $\nu\omega < 0$

In this case, we can see that the discriminant of Equation (5.25) is negative. This implies that there is a complex conjugate pair of roots to Equation (5.25) and hence to Equation (5.24). If there is a conjugate pair of roots for λ^2, then there must be two conjugate pairs of roots for λ, of the form $\lambda = a \pm ib$, $\lambda = -a \pm ib$, which guarantees a positive real part for the growth rate for any value of $a \neq 0$. This means that when there is an elliptical initial flow, the null will still tend to collapse, but may oscillate whilst doing so.

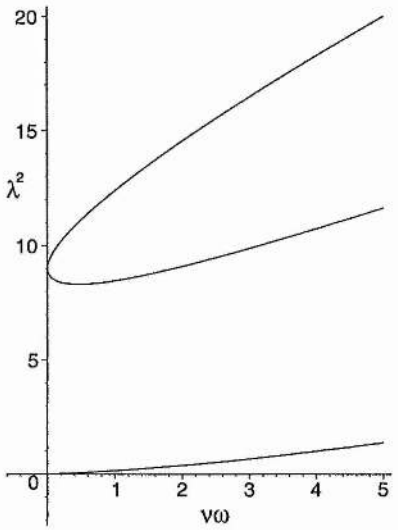

Figure 5.3: λ^2 as a function of $\nu\omega$. For all positive values of $\nu\omega$, λ^2 is also positive and so there is a positive growth rate which causes the null point to collapse.

5.5 Summary

In this chapter we have studied the linear collapse properties of three-dimensional potential null points from initial steady states that may include a plasma flow. The case with no initial plasma flow produces a null that collapses at the same rate as had been found previously in Parnell *et al* (1997) and the effect of adding an initial plasma flow is to speed up the collapse. This suggests that an initial plasma flow and associated pressure gradient make the null less stable against collapse.

As in our analysis of the collapse of 2D nulls, it should be noted that we have focussed on the local behaviour near a null and have asked whether a null has a tendancy to collapse when the boundary conditions are free. This means that the null is not isolated and energy may flow in from outside (e.g. Imshennik and Syrovatsky, 1967). Of course, if we had considered a potential null with fixed boundary conditions, there could be no collapse since the initial state has the minimum energy.

The presence of free functions in our analysis is symptomatic of the possible influence of external conditions on the null. Thus, in future it will be of great interest to consider the more complex problem of how general perturbations at large distances propagate into the null and cause it to collapse and reconnect.

Chapter 6

Coronal Tectonics

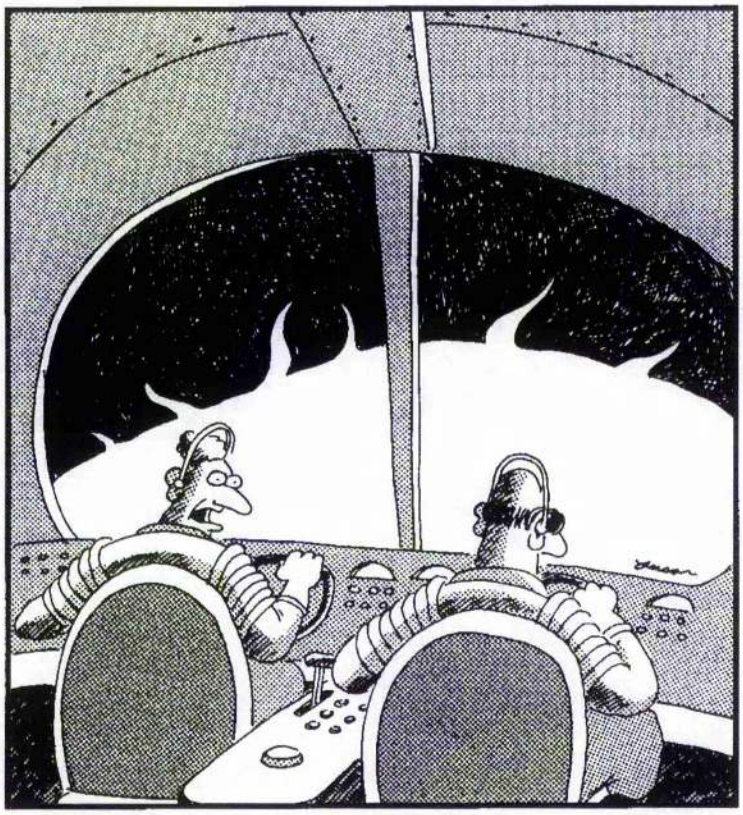

"It's no good, Dawson! We're being sucked in by the sun's gravitational field and there's nothing we can do! ... And let me add those are my sunglasses you're wearing!"

6.1 Introduction

There are many models for the heating of the solar corona through magnetic reconnection (for example, nanoflares and flux braiding). For a more comprehensive treatment of reconnection, see Priest and Forbes, 2000. Most involve complex plasma motions such as braiding of the magnetic field lines (Galsgaard and Nordlund, 1996).

Priest *et al* (2002) proposed a much simpler model. This model assumes that a typical TRACE coronal loop is made up of many smaller loops, too thin to be resolved, which embed separately in the photosphere, as shown in figure 6.1. Photospheric plasma motions move these small, elementary loops and current sheets build up and dissipate on the separatrix surfaces. Figure 6.2 shows a small part of an infinite array of magnetic sources which were moved on the photosphere to build up current sheets at the separatrices. Basic 2.5D and 3D analytical treatments were presented, showing the generation of concentrated current layers.

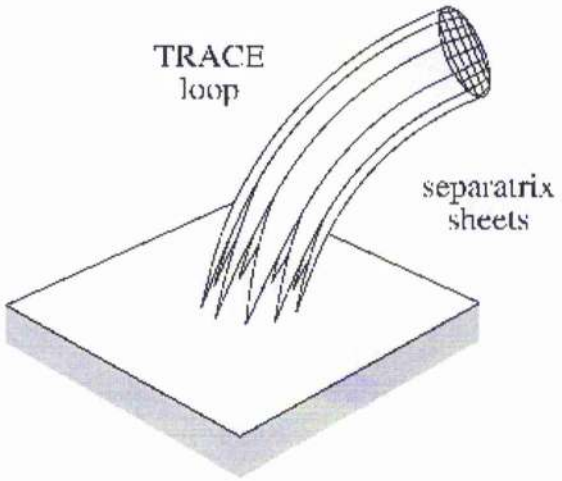

Figure 6.1: Priest *et al* (2002) suggest that a TRACE loop is made up from many smaller loops which separately embed themselves into the photosphere.

In this chapter we present the preliminary results from numerical simulations based on this coronal tectonics model.

6.2 Numerical Details

The simulations described in this chapter were carried out using the 3D MHD code described by Nordlund and Galsgaard (1995). The code solves the MHD equations in the form:

$$\frac{\partial \rho}{\partial t} = -\nabla . \rho \mathbf{u}, \tag{6.1}$$

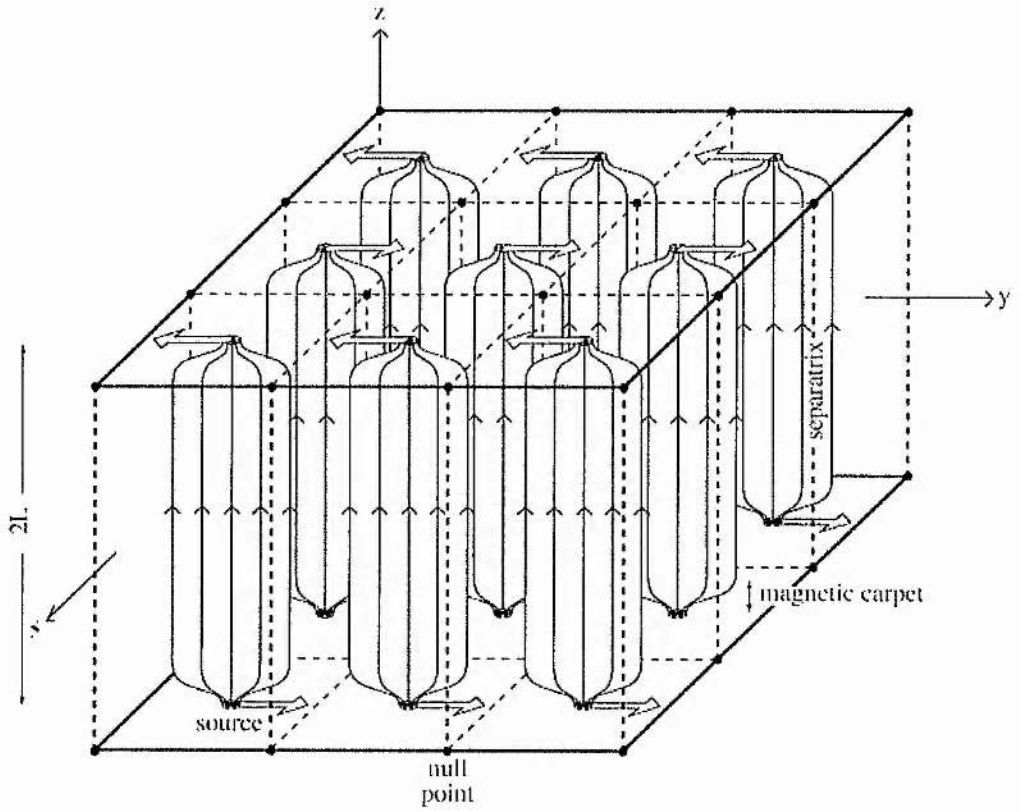

Figure 6.2: Model coronal loops produced by discrete magnetic sources (starred) located in the planes $z = \pm L$. Null points (dots) and separatrix surfaces (dashed) are also indicated.

$$\frac{\partial \mathbf{B}}{\partial t} = -\nabla \times \mathbf{E}, \tag{6.2}$$

$$\mathbf{E} = -(\mathbf{u} \times \mathbf{B}) + \eta \mathbf{J}, \tag{6.3}$$

$$\mathbf{J} = \nabla \times \mathbf{B}, \tag{6.4}$$

$$\frac{\partial \rho \mathbf{u}}{\partial t} = -\nabla.(\rho \mathbf{u}\mathbf{u} + \underline{\tau}) - \nabla P + \mathbf{J} \times \mathbf{B} - g\rho, \tag{6.5}$$

$$\frac{\partial e}{\partial t} = -\nabla.(e\mathbf{u}) - P\nabla.\mathbf{u} + Q_{cool} + Q_{visc} + Q_{joule}, \tag{6.6}$$

where ρ is the density, $\mathbf{u}$ is the velocity, $\mathbf{B}$ is the magnetic field, $\mathbf{E}$ is the electric field, η is the electric resistivity which is made up of two parts, η_1 and η_2. η_1 is a weak magnetic diffusivity,

$$\eta_1 = \frac{\Delta x}{Pr_M}(v_1 c_f + v_2 |u|),$$

and η_2 is a magnetic shock diffusivity which is proportional to the divergence of the velocity field perpendicular to the magnetic field,

$$\eta_2 = \frac{v_3 \Delta x^2}{Pr_M} |\nabla_\perp \cdot \mathbf{u}| .$$

Pr_M is a magnetic Prandtl number that scales the ratio of viscous and magnetic dissipation, v_n is the coefficient of the n^{th} order viscous diffusion term and c_f is the fast-mode speed. The magnetic diffusivity is thus allowed to vary in space and time to act on large magnetic currents and shocks. **J** is the electric current, $\underline{\underline{\tau}}$ is the viscous stress tensor, e is the internal energy, g is the constant of gravity, $P = (\gamma - 1)e$ is the gas pressure, $T = P/\rho$ is the temperature, Q_{cool} is the cooling term, Q_{visc} is the viscous dissipation and Q_{joule} is the joule dissipation. For the simulations described in this chapter we have neglected gravity and the cooling term. There remains the numerical resistivity and viscosity inherent in the code also, but these are on a very small scale due to the high order of the code.

These equations have been non-dimensionalised by setting $\mu_0 = 1$ and the gas constant $R_0 = \mu$ (the mean molecular weight). The dimensional quantities can be regained by multiplying the dimensionless quantities **v**, e, **B**, T, **E** and **J**, respectively, by

$$u_0 = l_0/t_0,$$

$$e_0 = \rho_0 u_0^2,$$

$$B_0 = u_0\sqrt{\mu_0 \rho_0},$$

$$T_0 = \mu u_0^2/R_0,$$

$$E_0 = u_0 B_0,$$

$$j_0 = B_0/(\mu_0 l_0),$$

where $\mu_0 = 4\pi \times 10^{-7} VsA^{-1}m^{-1}$ and $R_0 = 8.3143 Jmol^{-1}K^{-1}$ in SI units and l_0, t_0, ρ_0 and u_0 are typical length-scales, time-scales, density and plasma velocity.

The code makes use of a staggered mesh: the density and internal energy are volume centred, the magnetic field and momentum (ρ**u**) are face centred and the electric field and current are edge centred, as shown in Figure 6.3. In the centre of the numerical domain, the code is 6th order accurate in space and 3rd order in time using a 3rd order explicit predictor-corrector scheme. This spatial order reduces as the boundary approaches so that only one ghost cell is required at the boundary.

The boundary conditions are implemented using ghost cells and in the simulations described in this chapter we used periodic boundary conditions in y and z and driven boundary conditions

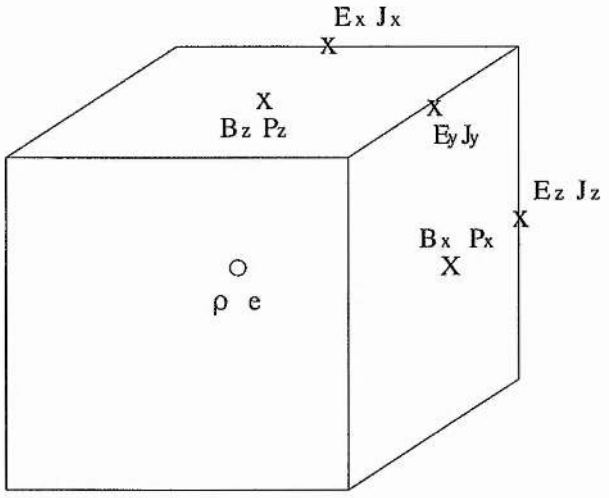

Figure 6.3: A typical cell demonstrating the staggering of the variables.

in x (the exact form of the driving will be described in Section 6.3.2). The periodic boundary conditions on the sides of the box mean that the ghost cells on one side are defined to be the same as the last cells on the other side. This implies that anything leaving one side of the domain will reenter on the opposite side. The boundary conditions in the x direction are as follows. There are no conditions imposed directly on ρ and e which are full point centred and as such are defined on the boundary and updated through the continuity and energy equations respectively. The velocity parallel to the boundary is imposed by us in Section 6.3.2), and the velocity normal to the boundary is set to be zero by having the ghost cell antisymmetric across the boundary. The magnetic field parallel to the boundary is full centred so we need impose no boundary conditions as it is updated directly by the induction equation. The perpendicular field is half centred and the condition $\nabla \cdot \mathbf{B} = 0$ is used to derive this component half a gridpoint outside the boundary.

Finally, the code has been written in both high performance Fortran (HPF) and Message-Passing Interface (MPI) so that it can be run on parallel computers. This has allowed us to carry out high grid resolution, 257^3 simulations.

6.3 The Model

6.3.1 The Initial Magnetic Field

The initial configuration consists of four equal flux patches and a small background axial field on the top ($x = 1$) and bottom ($x = 0$) boundaries of the numerical box. The x-component of the

field on the top and bottom boundaries is described by

$$\begin{aligned} B_x(x=0,1) = 0.1 \quad &+ \quad \exp(-350((y-0.5)^2+(z-0.2)^2)) \\ &+ \quad \exp(-350((y-0.5)^2+(z-0.8)^2)) \\ &+ \quad \exp(-350((y-0.2)^2+(z-0.5)^2)) \\ &+ \quad \exp(-350((y-0.8)^2+(z-0.5)^2)). \end{aligned}$$

We have a small background field for numerical reasons, in order to reduce the steep magnetic gradients near the top and bottom boundaries that would occur if the footpoints alone contributed to the flux. As such there are no null points or separatrices, but there are quasi-separatrix layers (QSLs) which separate the regions of different connectivity. A potential magnetic field was then created in the rest of the domain. The top and bottom boundaries were given driven boundary conditions and the remaining sides periodic boundary conditions in order to simulate a much larger array of sources. Figure 6.4 shows the axial field on the top and bottom boundaries. The internal energy is such that the plasma beta is initially 0.11 and the values of the mean resistivity ($\eta \approx 1.5 \times 10^{-4}$), mean Alfvén speed ($v_A \approx 0.15$), with a typical length (l) of 1 means that we have a Lundquist number ($L_u = v_A l/\eta$), of $L_u \approx 1000$ in the 129^3 runs of the code.

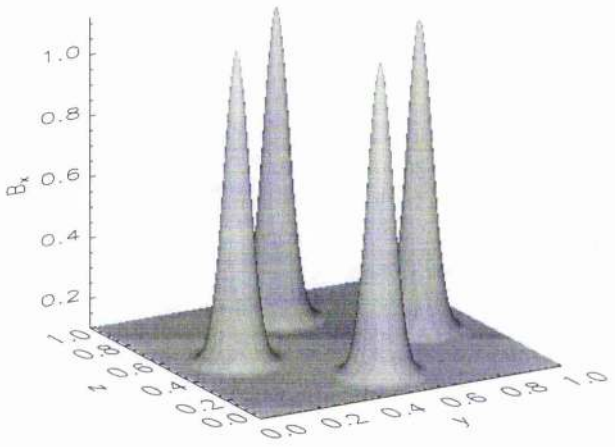

Figure 6.4: The initial axial magnetic field strength on the top and bottom boundaries

6.3.2 Driving on the Bottom Boundary

In order to model simple photospheric motions, we drive two of the flux patches on the bottom boundary in a straight line between the other two. The driving speed is -0.03 units which is approximately one fifth of the mean Alfvén speed in the numerical box. Explicitly, the driving function is given by

$$v_x = 0, \quad v_z = 0, \quad v_y = 0 \quad (0 < z < 0.375,\ 0.625 < z < 1),$$

$$v_y = -0.03 \quad (0.375 < z < 0.625).$$

The code automatically smooths this driving function for numerical stability and the resulting function for 129^3 is shown in figure 6.5, with the imposed driving velocity overlaid in red.

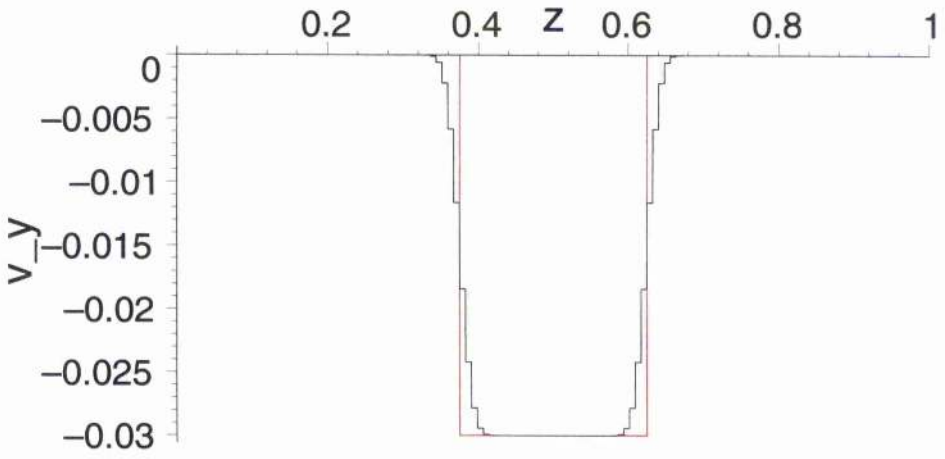

Figure 6.5: The driving velocity on the bottom boundary. Red is the inputted function and black is the smoothed function in the case of 129^3.

6.4 Results

The code was run for grid resolutions of 65^3, 129^3 and 257^3. Each resolution was run for 15.7 Alfvén times (t_A), meaning that the flux patches were driven a total distance of 0.47, the periodic boundary conditions ensuring that when a footpoint left one side of the box, another entered through the opposite side. During this time, the Alfvén waves travelling along the field lines had gone from the bottom of the box to the top, and reflected back to the bottom, and were approximately halfway up to the top again, allowing free and rapid propagation of information in the box. A further simulation was run on a 129^3 grid, but with the driving speed down to -0.01. This allows us to compare what happens when the footpoints are driven more slowly, allowing information to have propagated further for the same footpoint displacement.

6.4.1 Current Scaling

During the simulation, two sheets of current are seen to build up in the centre of the numerical box, as shown in Figure 6.8. They start off above the boundary at which the driving stops, and then follow the QSLs which is why they are not parallel. The sheets of current were checked for scaling to see whether they represented a current sheet (theoretically an infinitessimally thin

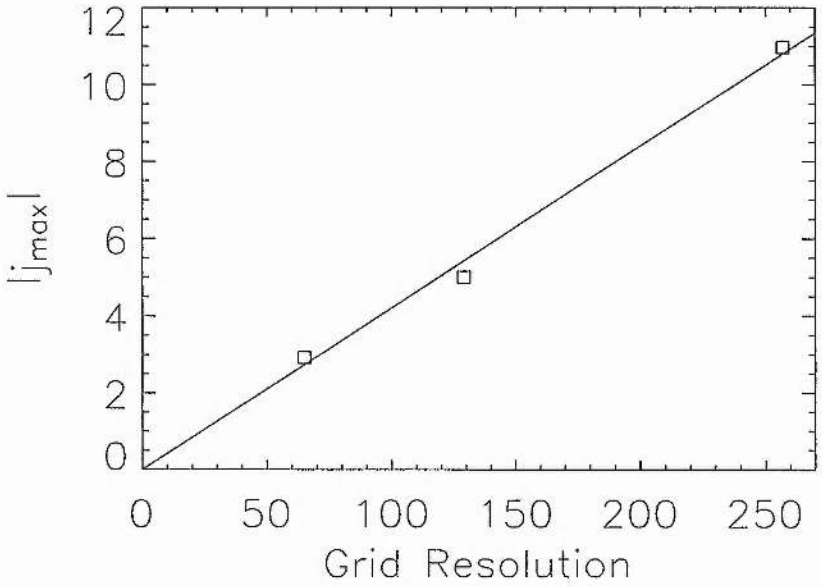

Figure 6.6: A plot of $|j_{max}|$ against grid resolution. The squares are the experimental results and the line is the line of best fit.

region of infinite current, which is significant because even the small coronal values of resistivity will trigger reconnection under this condition) or a current concentration which saturates at a finite value and only triggers reconnection for a finite value of the resistivity. If they are current sheets, the maximum value of the current will scale linearly with resolution, and so will double with each higher grid size in this experiment. Table 6.1 shows the maximum values of $|j|$ within the sheets of current throughout the simulation and compares them with the values we expect if we scale the observed 257^3 value with the grid resolution.

Grid Resolution	65^3	129^3	257^3
Expected Value of $\|j_{max}\|$	2.775	5.506	10.970
Observed Value of $\|j_{max}\|$	2.919	4.996	10.970

Table 6.1: Comparing the scaling of $|j_{max}|$ for the different grid resolutions.

Figure 6.6 shows $|j_{max}|$ against grid resolution for the different runs, with the line of best fit superimposed. The three data points have a correlation coefficient of 0.9966 and so fit extremely well to the regression line.

Table 6.1 and Figure 6.6 both imply that the maximum currents scale with grid resolution, and that there is evidence of current sheet formation, although higher resolution experiments may show that the current saturates at a finite value.

6.4.2 Slower driving

A 129^3 run was carried out where the footpoints were driven at one third of the speed of the previous runs. This allows information to propagate up and down the numerical box three times as much before the footpoints are driven to the same locations, allowing the magnetic field more chance to relax.

Figure 6.7 shows a plot of $|j_{max}|$ in the plane $x = 0.5$ for the 129^3 runs with a driving speed of -0.03 (solid line) and -0.01 (dashed line). The current jumps in value initially as the information propagates through this middle plane. As the footpoint displacement increases, the middle plane is being affected from above and below, so the current grows more smoothly.

Figure 6.8 shows isosurfaces of $|\mathbf{j}| = 2$ for the same two driving speeds and a footpoint displacement of 0.47, the quicker driving speed being on the left. In the case of the faster driving, there is slightly more current build-up near the boundaries, but the two main sheets of current are the same.

The current in both cases is growing at approximately the same rate for a given displacement and the isosurfaces of current look very similar so it would appear that for footpoint displacements up to the values we have investigated here, the speed at which the footpoints are driven does not affect the evolution of the field.

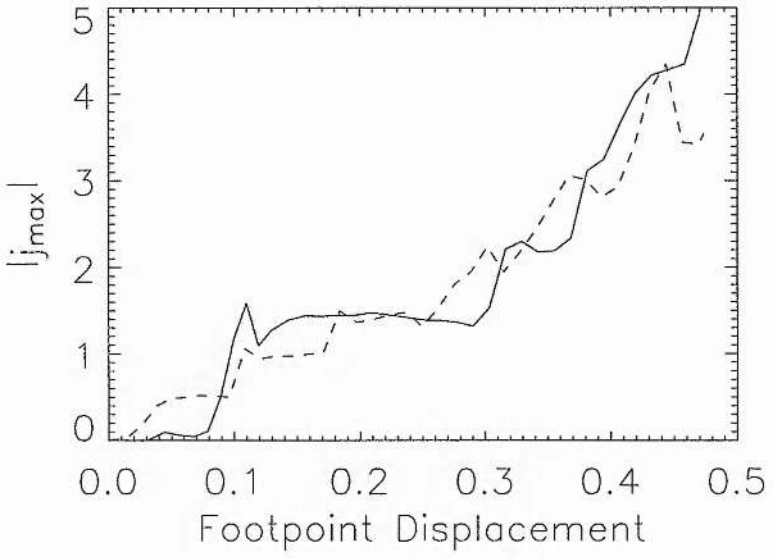

Figure 6.7: A plot of j_{max} in the plane $x = 0.5$ for the 129^3 runs with a driven speed of -0.03 (solid line) and -0.01 (dashed line). The current jumps in value initially as the information propagates through this plane. As the footpoint displacement increases, the middle plane is being affected from above and below, so the current grows more smoothly. The current in both cases is growing at approximately the same rate for a given displacement.

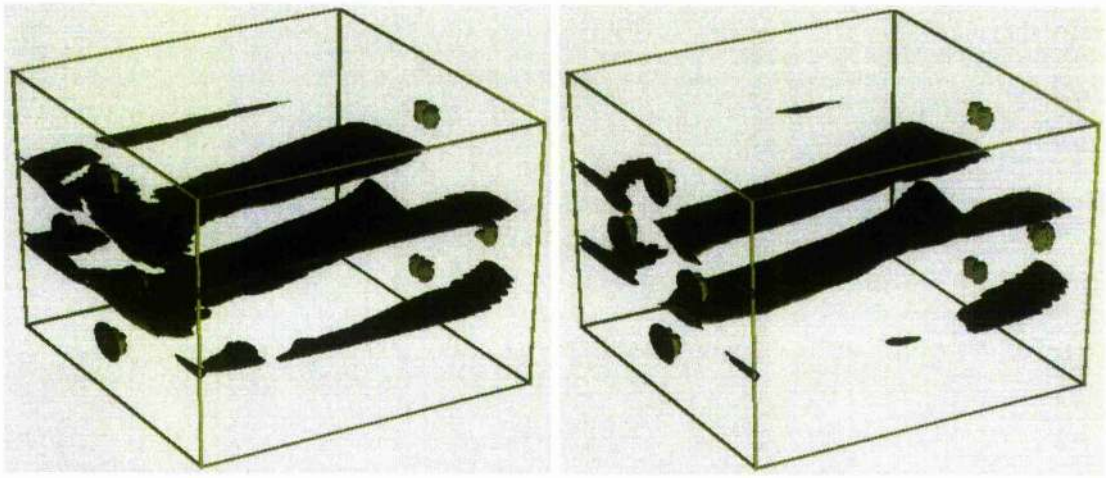

Figure 6.8: Plots of the current isosurface $|\mathbf{j}| = 2$ for the two different driving speeds at a footpoint displacement of 0.47. The quicker speed -0.03 is shown on the left and the slower speed -0.01 on the right.

6.4.3 Reconnection

The simulations give indications that reconnection is occurring. The 129^3 simulation with a driving speed of -0.03 was run for longer, up to a time of $43.02t_A$ (equivalent to a footpoint displacement of 1.29) in order to see if there was any evidence for reconnection in this time. All the figures in this section use the data from the 129^3 run.

Figure 6.9 shows contours of $|\mathbf{j}| = 3.6$ in the middle ($x = 0.5$) plane at $t = 37.2t_A$. This is half of the maximum current in the plane and gives a good idea as to how thick the sheets of current are. The second plot is a close-up of the top contour in the first plot, showing the sheet to be fewer than three grid points thick. A thin, localised current sheet is a strong feature of magnetic reconnection.

Figure 6.10 shows a representation of Petschek reconnection, for comparison with figures 6.11 and 6.12 which are taken in the $x = 0.5$ plane. The diffusion region can be compared with the plots of contours of $|\mathbf{j}|$ on the left hand side of figures 6.11 and 6.12 and the slow shocks show best in the vorticity, and so can be compared with the right hand plots of figures 6.11 and 6.12. Figure 6.11 shows contours of current (left) and the modulus of the vorticity (right) with plasma streaklines overplotted, in the middle plane at $t = 15.7t_A$. The lower plots are close-ups of the bottom sections of the upper plots to show the features more clearly. Figure 6.12 is the same as figure 6.11, but at a time $t = 32.1t_A$.

Each of these figures shows some similarity with figure 6.10. There is plasma outflow, shown in the velocity streaklines, from the diffusion region between the shocks, which are at a small

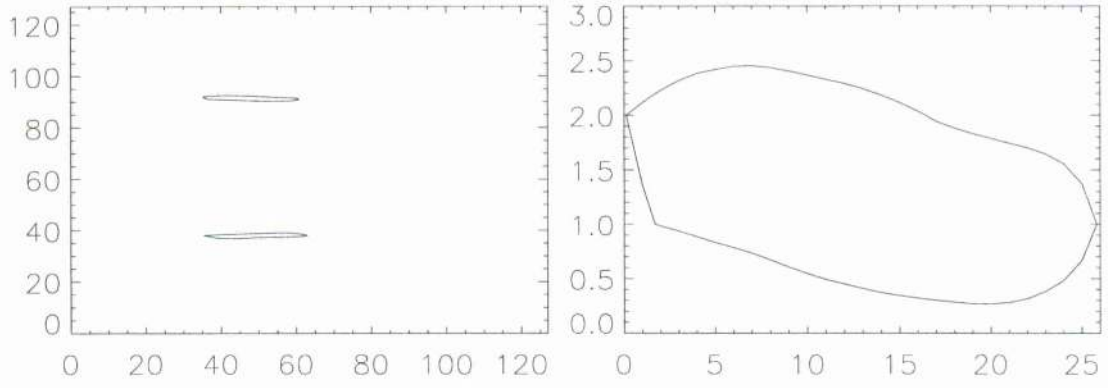

Figure 6.9: Contours of $|\mathbf{j}| = 3.6$ showing that the current sheet is thin. (*Left*) The whole of the $x = 0.5$ plane (*Right*) A close-up of the upper contour, showing it to be fewer than three grid points wide.

angle to each other. At $t = 15.7t_A$, the shocks are not very well defined by the vorticity, but are just perceptible. By the time we reach $t = 32.1t_A$, the shocks are much clearer in the vorticity contours, which can be seen to have a distinctive quadrupolar structure due to the rapid change in direction of the velocity through the shocks.

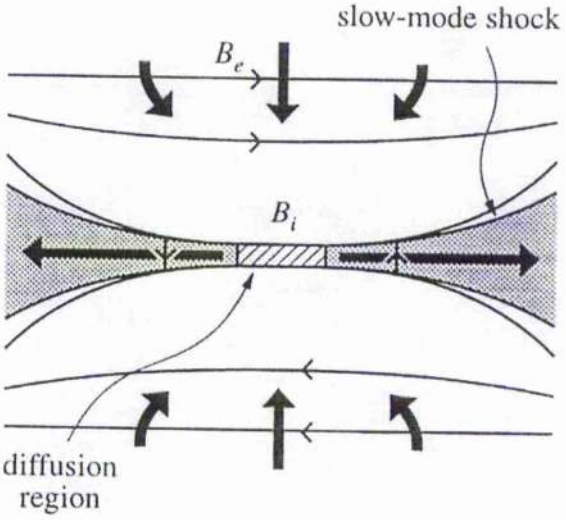

Figure 6.10: A representation of the Petschek reconnection model for comparison with figures 6.11 and 6.12

Figure 6.13 shows plots of isosurfaces of $|\mathbf{j}| = 3$ (green), $|\mathbf{j} \cdot \mathbf{B}|/(|\mathbf{j}||\mathbf{B}|) = 1$ (red) and a selection of magnetic field lines (blue). The four plots are for times $t = 13.8$, 30.7, 35.4 and $42.1t_A$. The red isosurfaces show possible reconnection sites, where the electric field is parallel to the magnetic field. The field lines are integrated from the same locations on the top ($x = 1$) boundary, which is held fixed, so they are the same field lines at each time.

Between 35.4 and $42.1t_A$ we can see that the current sheet has grown and expanded out toward the fieldlines, having passed through one central line. This fieldline has changed its connectivity, from remaining above the current sheet on the $x = 0$ plane at $t = 35.4t_A$, to having gone through the current sheet and been swept along with the driven plasma by $t = 42.1t_A$. Such changes of connectivity are another sign of reconnection.

Figure 6.14 shows the same as figure 6.13, but at $t = 37.2t_A$, and seen from above the $z = 1$ plane. The fieldlines are started from the $x = 1$ boundary at points going through the current sheet, and we can see that as they go through, they get swept along with the driven plasma. The fieldline that starts immediately above the current sheet can be seen to pass through it, and once again become swept away. This represents a change in connectivity also, as this fieldline would have started out being connected to the undriven point immediately opposite its starting point on the $x = 0$ plane. This plot also demonstrates that the current sheets follow the QSLs, because with the exception of the reconnected fieldline, it quite clearly defines the boundary between two regions of differing connectivity.

Finally, figure 6.15 shows plots of the Joule dissipation (left) in the numerical box throughout the experiment, and the Poynting flux (solid line) and kinetic energy (dashed line) on the right. The Joule dissipation increases from early in the experiment, showing that energy is being converted into heat almost straight away. The Poynting flux through the bottom ($x = 0$) boundary increases in steps, as the Alfvén waves carrying the information leave or reflect from this boundary at $t =$ 0, 12 and $25t_A$. The kinetic energy also follows a pattern to do with the Alfvén wave reflections from the top and bottom boundaries. It peaks when the Alfvén wave hits the top boundary, and falls as this wave is reflected.

All of these features are indications that magnetic reconnection is occurring, agreeing with one of the main features of the coronal tectonics model.

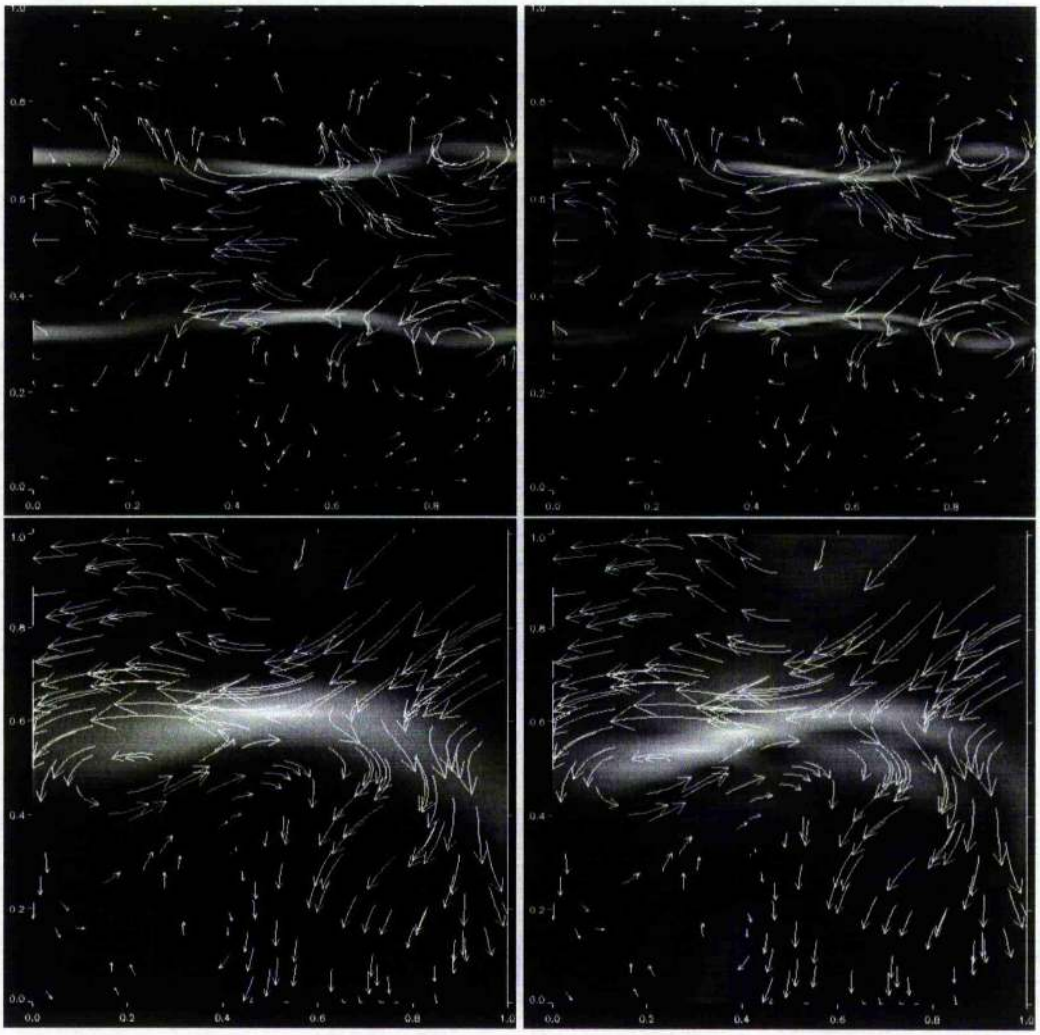

Figure 6.11: (*Top Left*) Current contours with velocity streaklines in the $x = 0.5$ plane at $t = 15.7t_A$. (*Top Right*) Vorticity contours with velocity streaklines in the $x = 0.5$ plane at $t = 15.7t_A$. (*Bottom Left*) A close-up of the bottom portion of top left to show better detail. (*Bottom Right*) A close-up of the bottom portion of top right to show better detail. The shocks are not very well defined at this time, but can just about be seen.

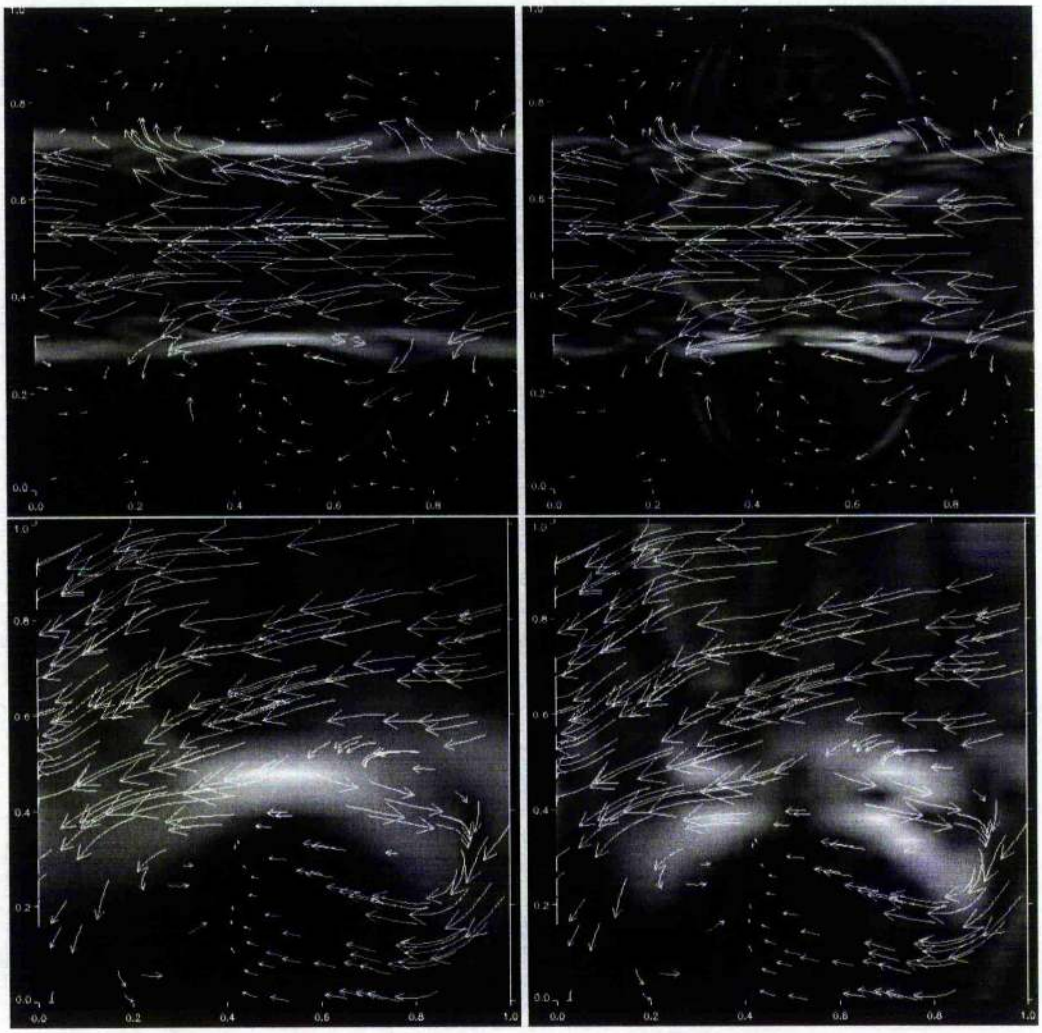

Figure 6.12: (*Top Left*) Current contours with velocity streaklines in the $x = 0.5$ plane at $t = 32.1t_A$. (*Top Right*) Vorticity contours with velocity streaklines in the $x = 0.5$ plane at $t = 32.1t_A$. (*Bottom Left*) A close-up of the bottom portion of top left to show better detail. (*Bottom Right*) A close-up of the bottom portion of top right to show better detail. The shocks are much better defined at this time.

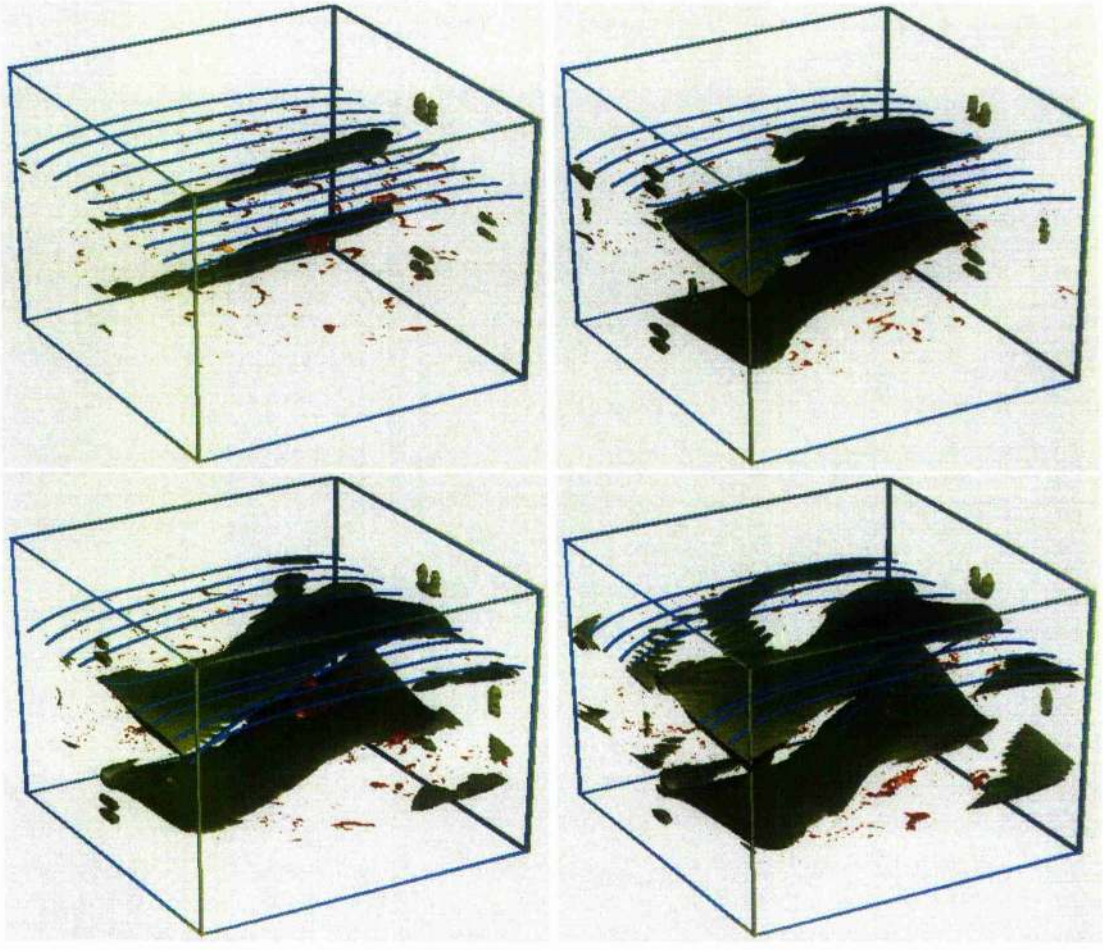

Figure 6.13: Plots of $|\mathbf{j}| = 3$ (green), $|\mathbf{j} \cdot \mathbf{B}|/(|\mathbf{j}||\mathbf{B}|) = 1$ (red) and a selection of magnetic field lines (blue) for $t = 13.8$, 30.7, 35.4 and $42.1 t_A$ from top left to bottom right. During the time between the last two plots, one of the fieldlines appears to have reconnected through the current sheet.

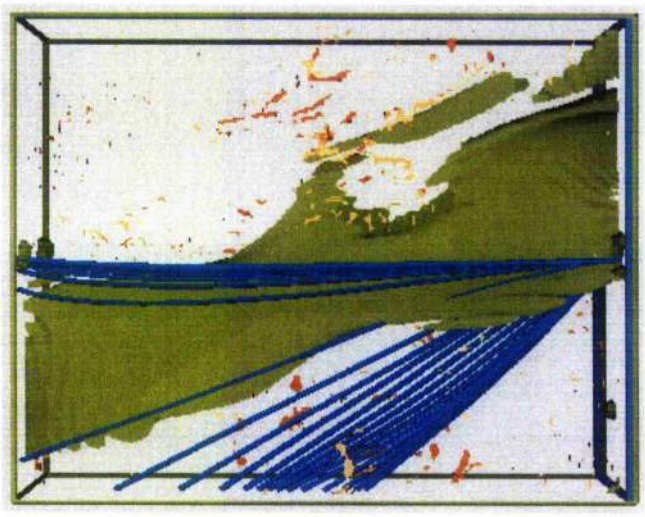

Figure 6.14: A plot showing the same as figure 6.13, but viewed from above the $z = 1$ plane and at $t = 37.2t_A$. The fieldlines' starting points are in a line through the current sheet and the one that starts immediately above this sheet appears to have reconnected through it.

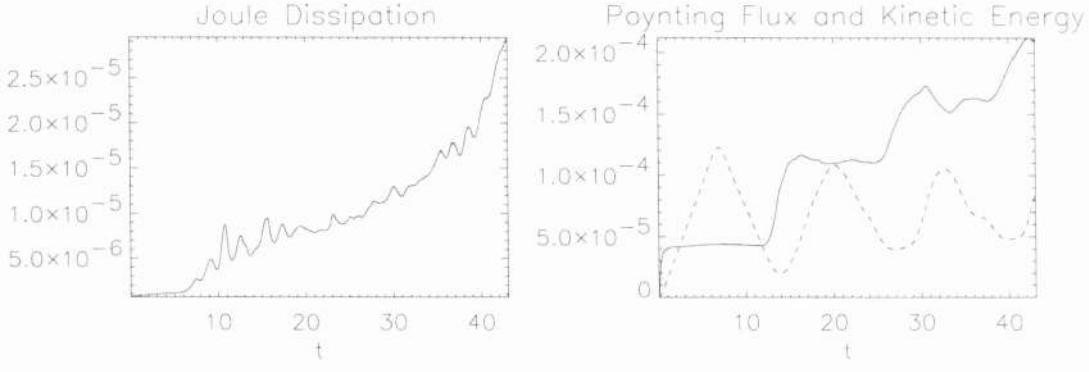

Figure 6.15: (*Left*) The Joule dissipation throughout the numerical box during the course of the experiment. Energy is being converted into heat from an early time. (*Right*) The Poynting flux through the bottom boundary (solid line) and the kinetic energy (dashed line). These increase and decrease in a pattern that follows the reflection of Alfvén waves from the top and bottom boundaries.

6.5 Summary

We ran a fully 3D, resistive MHD experiment with a low plasma beta and high Lundquist number in an attempt to model the coronal tectonics model (Priest *et al*, 2002). This was a preliminary experiment that started with a symmetrical magnetic field, which was moved at one end in a very simple straight line. It was run on three different grid resolutions, namely 65^3, 129^3 and 257^3.

Current sheets build up above the boundary at which the driving stops. These sheets are thin and orient themselves to follow the QSLs. The peak values of these currents scale very well with grid resolution, and so we can say that the sheets of current behave like infinitessimally thin mathematical current sheets with an infinite current density at the grid resolutions considered here.

Driving the footpoints more slowly appears to have a minimal effect on the evolution up to the times we have considered, but running for longer may well yield significant differences.

Finally, we appear to have evidence that magnetic reconnection is occurring. We can see structures in the current, vorticity and plasma velocity that mirror some aspects of Petschek reconnection. Magnetic fieldlines appear to be reconnecting through the current sheets, and there is Joule heating which could be caused by reconnection.

Future extensions to this numerical experiment will be detailed in chapter 7.

Chapter 7

Conclusions and Further Work

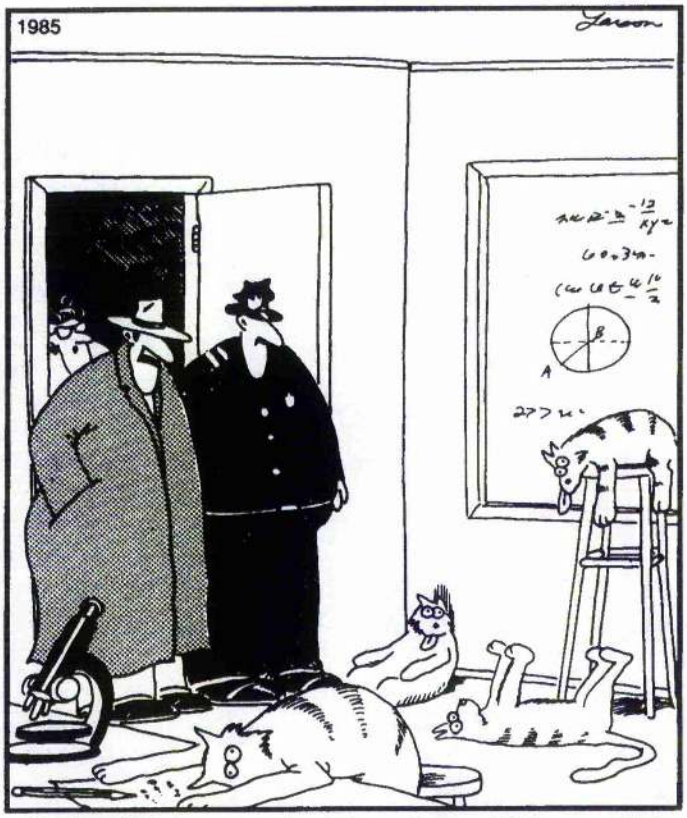

"Notice all the computations, theoretical scribblings, and lab equipment, Norm.... Yes, curiosity killed these cats."

7.1 Magnetic Annihilation

7.1.1 Stagnation-Point Flow and Asymmetric Boundary Conditions

Chapter 2 dealt with the steady, annihilation solution of Parker (1973) and Sonnerup and Priest (1975) which we extended by adding an asymmetry in the boundary conditions. We found that due to constraining the size of the diffusion region, the Alfvén Mach number of the plasma flow (M_e) was $M_e \propto 1/R_{me}$, where R_{me} is the magnetic Reynolds number. M_e is also a measure of the annihilation rate of the magnetic field, and is slower than the slow Sweet-Parker reconnection rate.

We also found that when an asymmetry is allowed by the physical constraints, it can never become large without breaking these constraints.

In the future, this type of analysis could be used to find more physical models of the 2D and 3D reconnective annihilation solutions (Anderson and Priest, 1993; Craig and Henton, 1995; Priest *et al*, 2000; Craig *et al*, 1995; Craig and Fabling, 1996)

7.1.2 Spine Reconnective Annihilation

The solutions presented in chapter 3 have some features that are just the same as the original magnetic annihilation solutions (Sonnerup & Priest, 1975) and so they may be regarded as a generalisation of such solutions. The first feature is that, apart from a beta-limitation and within the constraints of MHD, the reconnective annihilation may occur at any rate (v_e). All that happens as v_e increases is that the boundary-layer width (l) decreases. The beta-limitation arises because the plasma pressure inside the current concentration must remain positive (Priest, 1996; Litvinenko *et al*, 1996). It leads to an upper limit of roughly R_{me}^{-1} in the value of the inflow Alfvén Mach number ($M_e = v_e/v_{Ae}$) at large distances. The second feature is that the present solutions are very different qualitatively from the usual models for reconnection, such as the Sweet-Parker, Petschek and Almost-Uniform (Priest & Forbes, 2000) models, and this is the reason why we refer to them as reconnective annihilation models rather than reconnection models. In reconnective annihilation, the acceleration of the plasma along the infinite current sheet or tube is essentially passive due to a pressure gradient associated with a stagnation-point flow. In reconnection, on the other hand, the acceleration is by a combination of the $\mathbf{j} \times \mathbf{B}$ force and the pressure gradient associated with an excess pressure in a sheet of finite length. A third feature is that the exact solutions we have presented are particular solutions of the MHD equations with particular boundary conditions (as is usual for exact solutions of complex nonlinear equations). They also can represent local solutions near the stagnation point of more general global problems.

Exact solutions to the nonlinear MHD equations are extremely rare, but are of great value since their properties may be examined in a transparent way and they may give insights about the general physical behaviour of a plasma. In the subject of three-dimensional MHD reconnection only two such solutions have been previously discovered, namely, the reconnective fan annihilation regime (Craig *et al*, 1995) and the reconnective spine annihilation regime (Craig & Fabling, 1996). Here we have presented a two-fold generalisation of the basic spine reconnective annihilation solutions to leading order in η, where η ($\ll 1$) is the dimensionless magnetic diffusivity. A much larger family of three-dimensional reconnective annihilation solutions therefore exists than was previously thought.

Future work in this area will include a similar extension of Craig *et al* (1995) for the case of fan reconnective annihilation, and also a further generalisation of the solutions in this chapter to include an angular component of magnetic field and plasma flow.

7.2 Null Collapse

7.2.1 Collapse in 2D

In chapter 4, we developed an elegant method to consider the linear collapse of a linear null point to spatially linear perturbations. We have discovered that all X-type null points including steady flows and current have a tendency to collapse. An O-point without flow will also collapse, but an O-point with strong enough flow can be stable.

If the spatially linear system extends to infinity then its energy is infinité. If it is truncated by a boundary at some radius then the boundary is not in general closed, so that a collapse is associated with an inflow of energy into the region. However, if the linear system under study here is regarded as the local behaviour near a null point in a more global configuration, then the solutions indicate a tendency for collapse and therefore magnetic dissipation and heating near the null in response to distant motions.

7.2.2 Collapse in 3D

In chapter 5 we studied the linear collapse properties of three-dimensional potential null points from initial steady states that may include a plasma flow. The case with no initial plasma flow produces a null that collapses at the same rate as had been found previously in Parnell *et al* (1997) and the effect of adding an initial plasma flow is to speed up the collapse. This suggests that an initial plasma flow and associated pressure gradient make the null less stable against collapse. Parnell *et al* (1997) is, as far as we are aware, the only other analytical study of three-dimensional

null point collapse which has used the linearised MHD equations. However, they assumed a compressible plasma and only studied a few special cases.

All other studies of the collapse of three-dimensional null points have focussed on particular non-linear numerical solutions or asymptotic behaviour. Bulanov and Olshanetsky (1984), for example, found analytical solutions to the non-linear, ideal, compressible MHD equations which show that collapsing solutions close to a singularity display the asymptotic behaviour $\rho \propto (t-t_0)^{-2/3}$, $B \propto (t-t_0)^{-4/3}$, $v \propto (t-t_0)^{-1}$. Klapper *et al* (1996) numerically integrated the non-linear, compressible MHD equations governing collapse for a variety of initial conditions. They found that the asymptotic behaviour of the traces of matrices associated with magnetic field, plasma flow and pressure close to a singularity agrees with their own analytical predictions. Bulanov and Sakai (1997) numerically solved the compressible MHD equations for an initially potential field with no plasma flow. They found that a small velocity perturbation leads to a finite-time blow up of the current and vorticity. They started with the field $\mathbf{B} = [1.1x, 0.9y, -2.0z]$ and added a velocity perturbation that produces current in the z-direction (along the spine line of the initial null), $\mathbf{v}_1 = [0.1y, 0, 0]$. The current and vorticity become singular at a dimensionless time $t = 16.28$ and the field close to the spine line becomes stretched and rotates. Starting instead with the field $\mathbf{B} = [-1.25x, 0.75y, 0.5z]$ and adding the same velocity perturbation (this time producing current in the fan plane of the initial null), the current and vorticity become singular at a time $t = 2.084$, with the spine and fan collapsing together.

This chapter has developed the techniques for finding the collapse behaviour of a null in three dimensions. By necessity we have started with the simplest, potential case, albeit with or without a plasma flow. In future we also intend to extend the analysis to include null points which initially contain both current and plasma flow. We also plan to build on the work detailed above and study in detail the non-linear, compressible MHD equations governing null collapse with a view to discovering how and why the solutions develop from the linear predictions.

7.3 Coronal Tectonics

In chapter 6, we presented the results of preliminary simulations of the coronal tectonics model of Priest *et al* (2002). A simple, symmetrical, potential field was created and two footpoints on the lower boundary were driven between the other two. The top boundary was held fixed and we followed the 3D, resistive MHD evolution using a code detailed in Nordlund and Galsgaard (1995).

Two sheets of current built up in the centre of the numerical box, their locations corresponding with the boundaries on the base of the driven plasma, and the quasi-separatrix layers (QSLs) in the middle of the domain. These sheets of current scale with grid resolution, indicating that they

act as mathematical current sheets up to the highest resolution we considered (257^3). Higher grid resolutions may show that the current saturates at a finite value but to investigate this would require massive computational power at present unavailable.

The current sheets are thin (fewer than three grid points at a resolution of 129^3), and look similar if the footpoints are driven more slowly to the same position.

There were also indications of magnetic reconnection present in the simulation results.

- Structures in the current and vorticity mirrored the diffusion region and slow shocks present in Petschek reconnection. These structures appeared to be present at $t = 15.7t_A$ but were much clearer by $t = 32.1t_A$.
- Magnetic fieldlines appear to reconnect through the current sheets between $t = 35.4t_A$ and $42.1t_A$.
- There is Joule dissipation from an early time, but this could be heating from magnetic diffusion rather than reconnection.

There is still much to do to simulate the coronal tectonics model in future, as follows.

- Using the present simulations there are still many more ways we can analyse what is happening. Where is the Joule heating located - is it on the QSLs as predicted? Are all results similar and properly scaled in runs of different resolutions?
- The present simulations can be run for longer times. Will the current sheets start to tear? How does the tearing time compare to the expected value, $\sqrt{\tau_D \tau_A}$, the square root of the product of the diffusion time and the Alfvén time.
- Further into the future, we will change the driving velocity on the base to see how more complex motions affect the evolution.
- A different initial field will also be considered. This field will not be symmetrical, and the driving velocity will drive footpoints through QSLs. This should produce more heating as flux is forced through the QSLs.

Chapter 8

Bibliography

Anderson, C. and Priest, E.R. 1993, J. Geophys. Res., 98, 19395.

Biskamp, P.K. 1993, *Nonlinear Magnetohydrodynamics*, Cambridge Univ. Press. Cambridge, UK

Bulanov, S.V. and Olshanetsky, M.A. 1984, Phys. Letters, 100A, 35.

Bulanov, S.V. and Sakai, J. 1997, J. Phys. Soc. Jpn., 66, 3477.

Bulanov, S.V. and Sakai, J. 1998, Astrophys. J. S., 117, 599.

Bulanov, S.V., Shasharaina, S.G. and Pegoraro, F. 1990, Plasma Phys. Control Fusion, 32, 377.

Chapman, S. and Kendall, P.C. 1963, Proc. Roy. Soc. Lond., 271, 435.

Clark, A. 1964, Phys. Fluids, 7, 1299.

Craig, I.J.D. and Fabling, R.B. 1996, Astrophys. J., 462, 969.

Craig, I.J.D., Fabling, R.B., Henton, S.M. and Rickard, G.J. 1995, Astrophys. J., 455, L197.

Craig, I.J.D. and Henton, S.M. 1995, Astrophys. J., 450, 280.

Craig, I.J.D and McClymont, A.N. 1991 Astrophys. J., 371, L41.

Dungey, J.W. 1953, Phil. Mag., 44, 725.

Fontenla, J.M. 1993, Astrophys. J., 419, 837.

Forbes, T.G. and Speiser, T.W. 1979, J. Plasma Phys., 21, 107.

Galsgaard, K. and Nordlund, A. 1996, Astrophys. Lett. and Comm., 34, 175.

Galsgaard, K. and Nordlund, A. 1997b, J. Geophys. Res., 102, 231.

Goedbloed, J.P. 1983, *Lecture Notes on Ideal Magnetohydrodynamics*, Rijnhuizen reort, 83.

Hassam, A.B. 1992, Astrophys. J., 399, 159.

Heyn, M.F. and Pudovkin, M.L. 1993, J. Plasma Phys., 49, 17.

Hornig, G. and Rastätter, L. 1998, Physica Scripta, T74, 34.

Imshennik, V.S. and Syrovatsky, S.I. 1967, Sov. Phys. JETP, 141, 656.

Jardine, M., Allen, H.R. and Grundy, R.E. 1993, J. Geophys. Res., 98, 19409.

Klapper, I. 1998, Phys. Plasmas, 5, 910.

Klapper, I., Rado, A. and Tabor, M. 1996, Phys. Plasmas, 3, 4281.

Lin, C.C. 1958, Arch. Ration. Mech. Analysis, 1, 391.

Litvinenko, Y.E., Forbes, T.G. and Priest, E.R. 1996, Solar Phys., 167, 445.

Neukirch, T. 1995, Phys. Plasmas, 2, 4389.

Neukirch, T. and Cheung, D.L.G. 2001, Proc. R. Soc. Lond., 457, 2547.

Neukirch, T. and Priest, E.R. 2000, Phys. Plasmas, 7, 3105.

Nordlund, A. and Galsgaard, K. 1995, A 3D MHD Code for Parallel Computers. Technical Report, Astronomical Observatory, Copenhagen University.

Parker, E.N. 1973, J. Plasma Phys., 9, 49.

Parnell, C.E., Neukirch, T., Smith, J.M. and Priest, E.R. 1997, Geophys. Astrophys. Fluid Dynamics, 84, 245.

Parnell, C.E., Smith, J.M., Neukirch, T. and Priest, E.R. 1996, Phys. Plasmas, 3, 759.

Priest, E.R. 1982, *Solar Magnetohydrodynamics*, D.Reidel Publishing

Priest, E.R. 1996, in *Solar and Astrophysical MHD Flows*, ed. K. Tsinganos (Kluwer, Dordrecht), 151.

Priest, E.R. and Demoulin, P. 1995, J. Geophys. Res., 100, 23443

Priest, E.R. and Forbes, T.G. 1989, Solar Phys., 119, 211.

Priest, E.R. and Forbes, T.G. 2000, *Magnetic Reconnection*, Cambridge Univ. Press. Cambridge, UK

Priest, E.R., Heyvaerts, J.F. and Title, A.M. 2002, Astrophys. Journal, 576, 533.

Priest, E.R. and Titov, V.S. 1996, Phil. Trans. R. Soc. Lond., 354, 2951.

Priest, E.R., Titov, V.S., Grundy, R.E. and Hood, A.W. 2000, Proc. R. Soc. Lond. 456, 1821.

Schindler, K., Hesse, M. and Birn, J. 1988, J. Geophys. Res., 93, 5547.

Sonnerup, B.U.Ö. and Priest, E.R. 1975, J. Plasma Phys., 14, 283.

Titov, V.S. and Hornig, G. 2000, Phys. Plasmas, 7, 3542.

Titov, V.S. and Priest, E.R. 1993, Geophys. Astrophys. Fluid Dynamics, 72, 249.

The End!